

**Clarification of saline groundwater system in  
sedimentary rock area by geostatistical analyses of  
drilling investigation data**

**Lei Lu**

**2015**



**Kyoto University**

**Dissertation**

**Clarification of saline groundwater system in sedimentary rock area by  
geostatistical analyses of drilling investigation data**

Author  
Lei Lu

Supervisor  
Prof. Katsuaki Koike

Environmental Geosphere Engineering  
Department of Urban Management Engineering  
2015



**Clarification of saline groundwater system in  
sedimentary rock area by geostatistical analyses of  
drilling investigation data**

A thesis presented

by

Lei Lu

to

The Department of Urban Management Engineering

in partial fulfillment of the requirements  
for the degree of  
Doctor of Philosophy  
in the subject of  
Urban Management Engineering

Examination Committee:      Prof. Katsuaki Koike (Chairperson)  
   Prof. Tsuyoshi Ishida  
   Associate Prof. Yoshitada Mito

Kyoto University  
Kyoto, Japan

2015

© 2015

by Lei Lu

# **Clarification of saline groundwater system in sedimentary rock area by geostatistical analyses of drilling investigation data**

## **Abstract**

Radioactive wastes of all types need to be responsibly managed in facilities under institutional control to provide public safety, protection of the environment and security from accidental or deliberate intrusion. However, in the long run, long lived radioactive wastes need to be disposed of in a way that does not require continued institutional control. The concept of isolating long lived radioactive wastes from the human environment by placing them deep underground in repositories located in host rocks characterized by high stability and low or no groundwater flow was proposed in many countries.

Suitable environment for such disposal assessment requires: extremely low permeability rocks in which advective groundwater flow is essentially precluded; deep groundwater systems which have displayed stable extremely low natural advective fluxes for periods of hundreds of thousands of years or longer; groundwater systems which have low fluxes combined with long transport paths away from the disposal zone to potentially accessible groundwater systems or to the biosphere.

Sedimentary rocks have been chosen to be host rock for high level nuclear waste (HLW) disposal in research field; this is due to favorable characteristics of sedimentary rock for long-term HLW disposal repositories, which have low

permeability, a small diffusion coefficient, and low adsorption capacity for radionuclides. One of main and important topic in researches based on sedimentary rocks is groundwater modeling, especially saline water. This kind of research would demand following perspective, moreover, those requirements usually are inevitably difficult and become challenges deserved to be resolved.

They includes mapping spatial distribution of saline water (seawater or brine), which can be indexed by chloride ion, in three-dimension; integrating geological structure like formations and fault (zone) into the spatial mapping to depict relationship between deep groundwater and geological structure; developing model paradigm honoring various types of information (qualitative and quantitative), multi-source of data (hard data and soft data); being capable in methods to solve sparse dataset modeling. However, current researches have scarcely provided insights on these points.

Sedimentary rocks extensively exist in Japan, like Hokkaido, northern Tohoku, and Kyushu. Most of these sedimentary rocks are in coastal area whose geological environment investigation is relative few compared with inland; influence of saline water towards the deep subsurface needs to be clearly described; hydrogeological structure (fault zone hydrology) in three-dimension is dispensable in the HLW disposal. Furthermore, deep subsurface information and data are barely enough, especially boreholes data. Therefore, Horonobe Underground Research Laboratory in northern Hokkaido is chosen to solve aforementioned problems.

Water samples, geological columns, and well log data to 1-km depth were taken at 10 sites in the area, showing a dominance of Na-HCO<sub>3</sub> type freshwater in shallow areas and Na-Cl type saline water in deep parts. As for the sparse data, a co-conditional simulation integrating hard data like borehole sampling data and

soft data like resistivity logging data is developed, moreover, the fault dip shows strongly act in the modeling that become a parameter in geostatistical estimation and simulation.

More results could be summarized as follow. For detecting the detailed distribution and variation of saline water, a 3D model of chloride ion ( $\text{Cl}^-$ ) concentration is produced in conjunction with resistivity logging data through kriging estimation and sequential Gaussian co-simulation. Variography shows that the dip of the main Omagari Fault is a control on the spatial correlation structure of  $\text{Cl}^-$  concentration. The 3D model shows that this fault and its auxiliary constitute a clear boundary between high and low saline waters, and that  $\text{Cl}^-$  concentrations tend to change in accord with sedimentary layer structures. Integration of a data analysis of stable isotopes suggests that the deep saline water with heavy  $\delta\text{D}$  and  $\delta^{18}\text{O}$  originated from fossilized seawater trapped in the sedimentation and diagenetic processes during the Miocene, whereas the shallow fresh water with light values is of meteoric water origin. Dilute saline water in the deep part is partially attributable to dehydration of minerals from opal-A to opal-CT. Well tests suggest that vertical groundwater flow prevails near the Omagari Fault, while lateral flow is general in other zones. Difference in the depth of transition zones may be caused by the dominant flow among downward, ascending, and lateral. Consequently, the geostatistical techniques and data integration in this study are useful to depict the regional groundwater system from a dataset of water investigation limited by quantity and location.

## **Acknowledgement**

First and foremost I want to deeply thank my supervisor Professor Katsuaki Koike for his guidance, encouragement, critical feedback. During my four years in Kyoto, I learned tremendously from him, not only in research, but also in many others aspects that will be beneficial to all my life, such as how to write in an efficient way, how to face technical difficulties or how to communicate with people. All his inputs and advices are, and will remain, invaluable to me.

I am really appreciating my sub supervisor, Associate Professor Yoshitada Mito who inspired, supported me in a scientific or non-scientific sense, and has helped me increase my understanding of a variety of scientific disciplines. I also want thank assistant professor Kouki Kashiwaya for his help during all the seminars and courses. It has been a great pleasure to have him in my group and take advantage of his ideas and suggestions.

Furthermore, I would like to thank my committee members. Especially I would like to thank Professor Tsuyoshi Ishida for being the readers of this dissertation. Even though it turned out to be a long work, but he did not hesitate to provide me with his inputs on how to make it better.

Thanks are also due to three advisors from my internships at JAEA (Japan Atomic Energy Agency) also deserving special recognition for their support. Without their precious inputs, applying my PhD ideas to real-world problem would be impossible. It was a delight to work with such a smart and knowledgeable team. Finally, I also would like to thank my lab mates.

They gave me their help and support through every stage of my education and my research. I am forever grateful to them.

## List of Tables

TABLE 1.1 PROPOSALS FOR THE NUCLEAR WASTE DISPOSAL AND STATUS .....	2
TABLE 1.2 HOST ROCK TYPES FOR THE GEOLOGICAL DISPOSAL OF SOLID RADIOACTIVE WASTE .....	6
TABLE 1.3 PRINCIPAL GROUPS OF SEDIMENTARY ROCK .....	9
TABLE 3.1 GEOLOGICAL STRATIGRAPHY IN RESEARCH AREA .....	49
TABLE 3.2 ORIENTATIONS (DIP DIRECTION/DIP) OF BEDDING PLANES AND FAULTS IN BOREHOLES..	53
TABLE 5.1 PERMEABILITY SETTING.....	90
TABLE 5.2 FLOW DIRECTION AND VALUES .....	90

## List of Figures

FIG. 1.1	BRIEF ROCK TYPE IN JAPAN.....	8
FIG. 2.1	SEMIVARIOGRAM MODELS .....	32
FIG. 2.2	COMPARISON OF SIMULATION AND ESTIMATION .....	41
FIG. 3.1	RESEARCH AREA AND BOREHOLES LOCATION WITH MAIN FAULT.....	46
FIG. 3.2	GEOLOGIC MAP OF STUDY AREA AND CROSS-SECTION ALONG A–B, SHOWING GENERAL GEOLOGICAL STRUCTURE, AFTER THE GEOLOGICAL SURVEY OF JAPAN, AIST (2012).....	49
FIG. 3.3	SKETCHES AT THE FAULT OUTCROP OF THE OMAGARI FAULT IN THE BOREHOLES HDB-4 AND HDB-5, THERE WERE NUMEROUS FRACTURES AND CIRCULATION LOSS SECTIONS DURING DRILLING, SUGGESTING THAT THESE FRACTURES MAY BE IMPORTANT AS SOLUTE TRANSPORT PATHWAYS. ....	54
FIG. 3.4	PLOT OF TOPOGRAPHY AND BOREHOLES IN HORONOBE URL.....	55
FIG. 3.5	CONCEPTUAL MODEL OF GEOLOGICAL STRUCTURE AND FORMATIONS IN HORONOBE. ...	56
FIG. 3.6	CONCEPTUAL MODEL OF FAULTS IN AND AROUND THE URL AREA MODIFIED FROM ISHII AND FUKUSHIMA .....	57
FIG. 3.7	DISCRETE POINTS EXTRACTED FROM 3D GEOLOGICAL MODELS. ....	58
FIG. 3.8	3D GEOLOGIC MODEL SHOWING FORMATION BOUNDARIES (TOP AND BOTTOM PLANES) AND PLANE SHAPES OF OMAGARI FAULT AND SUBFAULT, ALONG WITH DISTRIBUTION OF BOREHOLES (RED LINES). LETTER DESIGNATORS ARE AS FOLLOWS. A: OMAGARI FAULT, B: SUBFAULT, C: WESTERN PART OF BOUNDARY BETWEEN WAKKANAI AND MASUPORO FORMATIONS, D: WESTERN PART OF BOUNDARY BETWEEN KOETOI AND WAKKANAI FORMATIONS, E: BOUNDARY BETWEEN YUCHI AND KOETOI FORMATIONS, AND F: BOUNDARY BETWEEN SARABETSU AND YUCHI FORMATIONS.....	59
FIG. 3.9	DISTRIBUTION OF LOG-TRANSFORMED VALUES .....	62
FIG. 4.1	PLOTS OF HYDRAULIC CONDUCTIVITY FROM WELL TESTS IN YUCHI, KOETOI, AND WAKKANAI FORMATIONS AND DAMAGE ZONES. BARS DEPICT TEST INTERVALS.....	65
FIG. 4.2	STIFF DIAGRAMS OF GROUNDWATER SAMPLES IN EACH BOREHOLE AND GEOLOGICAL COLUMNS, WHICH ARE PROJECTED ON THE A–B CROSS-SECTION IN FIG. 3.2. ....	66
FIG. 4.3	COMPARISON OF OMNIDIRECTIONAL EXPERIMENTAL SEMIVARIOGRAMS OF $Cl^-$ CONCENTRATION ALONG DIP DIRECTION OF OMAGARI FAULT, THE MAIN FAULT IN THE STUDY AREA (A), AND ALONG THE HORIZONTAL DIRECTION (B).....	67
FIG. 4.4	SCATTERGRAM BETWEEN MEASURED AND PREDICTED $Cl^-$ CONCENTRATIONS FOR CROSS-VALIDATION OF THE ACCURACY OF OK RESULT IN FIG. 4.5. ....	69
FIG. 4.5	ESTIMATION OF $Cl^-$ CONCENTRATION BY ORDINARY KRIGING (OK) INTEGRATED WITH SHAPES OF OMAGARI FAULTS AND BOUNDARIES OF KOETOI AND WAKKANAI FORMATIONS. A: DISTRIBUTION OF RELATIVELY HIGH CONCENTRATIONS > 8000 MG/L SUPERIMPOSED ON SAMPLE DATA ALONG EACH BOREHOLE; B: PANEL DIAGRAM OF $Cl^-$ CONCENTRATION BY OK	

WITH SHAPES OF OMAGARI FAULTS AND BOUNDARIES OF KOETOI AND WAKKANAI FORMATIONS FROM GEOLOGICAL MODEL SHOWN IN FIG. 3.6. ....	70
FIG. 4.6 PANEL DIAGRAM OF RESISTIVITY DISTRIBUTION BY SEQUENTIAL GAUSSIAN SIMULATION (SGS) AT SAME LOCATION AS FIG. 4.5, SUPERIMPOSED ON SHAPES OF OMAGARI FAULT AND SUBFAULT. ELLIPSE INDICATES HIGH RESISTIVITY ZONE IN SHALLOW PART ALONG OMAGARI FAULT, WHICH SUGGESTS DOWNWARD FLOW OF METEORIC WATERS. ....	71
FIG. 4.7 PLOT OF RESISTIVITY AND CONCENTRATION OF CHLORIDE IONS.....	72
FIG. 4.8 CORRELATION PLOT AND CROSS-VARIOGRAM OF RESISTIVITY AND $Cl^-$ .....	73
FIG. 4.9 TEN CSGS OF $Cl^-$ CONCENTRATION WITH RESISTIVITY (A) AND PANEL DIAGRAM OF IT (B).....	73
FIG. 5.1 CHANGES OF $\Delta D$ AND $\Delta^{18}O$ IN PORE-WATER SAMPLES WITH DEPTH FOR EACH BOREHOLE. ....	77
FIG. 5.2 $\Delta D$ AND $\Delta^{18}O$ DIAGRAM SHOWS A GENERAL TWO TYPE OF SALINE WATER .....	78
FIG. 5.3 PLOT OF ROCK DENSITY, POROSITY AND RESISTIVITY IN TEN BOREHOLES .....	80
FIG. 5.4 DENSITY, POROSITY, AND RESISTIVITY LOG DATA OF HDB-1 SHOWING THREE ZONES OF SIMILAR ROCK PROPERTIES. WATER SAMPLE DATA FROM THE THREE ZONES ARE IDENTIFIED AS GROUPS I, II, AND III. ....	81
FIG. 5.5 STABLE ISOTOPE, $\Delta D$ AND $\Delta^{18}O$ DIAGRAM WITH LOCAL METEORIC WATER LINE (LMWL). DATA ARE CLASSIFIED INTO THREE GROUPS. ....	81
FIG. 5.6 TWO SCATTERGRAMS BETWEEN $\Delta D$ AND $\Delta^{18}O$ AND $Cl^-$ CONCENTRATION AND $\Delta D$ DATA OF THREE GROUPS IN INTERNAL AND EXTERNAL REGIONS. THE REGIONS ARE DEFINED BY A CRITERION OF DISTANCE FROM OMAGARI FAULT AND ITS SUBFAULT: INTERNAL ( $\leq 700$ M) AND EXTERNAL ( $> 700$ M). ....	84
FIG. 5.7 HIGH-RESOLUTION SEM IMAGES. ....	84
FIG. 5.8 SCHEMATIC MODEL OF GROUNDWATER FLOW PATTERNS AND ZONATION OF FRESH, SALINE, AND MIXING WATERS WITH GEOLOGICAL STRUCTURE ALONG CROSS-SECTION A–B (FIG. 4.1). ARROWS INDICATE FLOW DIRECTIONS AND MAGNITUDES BY THEIR LENGTHS. Y.F.: YUCHI FORMATION, K.F.: KOETOI FORMATION, W.F.: WAKKANAI FORMATION, M.F.: MASUPORO FORMATION, AND O.F.: ONISHIBETSU FORMATION .....	85
FIG. 5.8 THE ANALYTIC MODELING AREA .....	88
FIG. 5.9 50 M MESH DEM AND ANALYTIC AREA (BLACK LINE IN LEFT). ....	89
FIG. 5.10 THE ANALYTIC MODEL OF GROUNDWATER FLOW SIMULATION.....	89
FIG. 5.11 FLOW DIRECTIONS IN CROSS-SECTION .....	91

## Contents

<b>Abstract</b> .....	i
<b>Acknowledgement</b> .....	iv
<b>List of Tables</b> .....	vi
<b>List of Figures</b> .....	vii
<b>Chapter 1</b> .....	1
<b>Introduction</b> .....	1
<b>1.1 The geological underground disposal</b> .....	3
<b>1.2 Review of related researches</b> .....	6
<b>1.3 Problem statement</b> .....	14
<b>1.3 Main objective</b> .....	15
<b>1.4 Originality and contributions</b> .....	16
<b>1.5 Thesis structure</b> .....	17
<b>1.6 Summary</b> .....	18
<b>Chapter 2</b> .....	19
<b>Spatial Multivariate Modeling</b> .....	19
<b>2.1 The beginning of spatial variant</b> .....	19
<b>2.2 Modeling continuous spatial variation</b> .....	20
<b>2.3 Spatial Random Processes</b> .....	23
<b>2.3.1. Spatial Random field</b> .....	23
<b>2.3.2. Stationary and Intrinsically Stationary Processes</b> .....	24
<b>2.4 Geostatistical process estimation</b> .....	25
<b>2.4.1. Geostatistical Model</b> .....	26
<b>2.4.2. Estimation of the Semivariogram</b> .....	28
<b>2.4.3. Modeling the Semivariogram</b> .....	30
<b>2.4.4. Cross-validating the fitted variogram</b> .....	33
<b>2.4.5. Kriging</b> .....	34
<b>2.5 Geostatistical process simulation</b> .....	40
<b>2.6 Summary</b> .....	42
<b>Chapter 3</b> .....	44
<b>Case Site and Fundamental Data Properties</b> .....	44
<b>3.1 The HLW disposal situation</b> .....	44
<b>3.2 Investigation and background setting</b> .....	45
<b>3.2.1 Surface-based investigations in Horonobe area</b> .....	46
<b>3.2.2 Borehole investigations</b> .....	53
<b>3.3 Geological modeling</b> .....	56
<b>3.4 Data sampling and analyses</b> .....	58
<b>3.5 Summary</b> .....	62

<b>Chapter 4</b> .....	64
<b>Spatial Characterization of Groundwater Chemistry</b> .....	64
<b>4.1 General characteristics of groundwater chemistry</b> .....	64
<b>4.2 3D distribution of chloride ion concentration</b> .....	67
<b>4.3 Summary</b> .....	74
<b>Chapter 5</b> .....	75
<b>Origin of Groundwater and Temporal Change in Salinity</b> .....	75
<b>5.1 Origin of groundwater</b> .....	75
<b>5.2 Chemical evolution of saline water</b> .....	82
<b>5.3 Groundwater flow modeling in Horonobe area</b> .....	86
<b>5.4 Summary</b> .....	91
<b>Chapter 6</b> .....	93
<b>Conclusions and Future Work</b> .....	93
<b>6.1 Conclusions</b> .....	93
<b>6.2 Future work</b> .....	95
<b>References</b> .....	96
<b>List of Main Associated Publications</b> .....	<b>Error! Bookmark not defined.</b>

# **Chapter 1**

## **Introduction**

All kinds of radioactive wastes need to be managed responsibly in facilities under governmental control to provide public safety, protection of the environment and security from accidental or deliberate intrusion (IAEA, 1995). However, in the long run, long lived radioactive wastes need to be disposed of in a way that does not require continued institutional control. The concept of isolating long lived radioactive wastes from the human environment by placing them deep underground in repositories located in host rocks characterized by high stability and low or no groundwater flow, i.e. geological disposal, was proposed over 40 years ago.

Alternative disposal options, such as disposal in subduction zones along the boundaries of the Earth's tectonic plates, in polar ice caps or even in space, have been rejected on the basis of generic assessments (Table 1.1). Geological disposal of waste packages in the clay-rich sediments underlying the ocean floor, despite the extremely promising results of international studies carried out in the 1980s (OECD, 1988), is presently not considered a realistic disposal option owing to

being prohibited by the London Convention (IAEA, 1999).

Table 1.1 Proposals for the nuclear waste disposal and status

Proposal	Examples
Long-term above ground storage	<ul style="list-style-type: none"> <li>• Investigated in France, Netherlands, Switzerland, UK and USA.</li> <li>• Not currently planned to be implemented anywhere.</li> </ul>
Disposal in outer space (proposed for wastes that are highly concentrated)	<ul style="list-style-type: none"> <li>• Investigated by USA.</li> <li>• Investigations now abandoned due to cost and potential risks of launch failure.</li> </ul>
Deep boreholes (at depths of a few kilometers)	<ul style="list-style-type: none"> <li>• Investigated by Australia, China, Denmark, Italy, Japan, Russia, Sweden, Switzerland, UK and USA.</li> <li>• Not implemented anywhere.</li> </ul>
Rock-melting (proposed for wastes that are heat generating)	<ul style="list-style-type: none"> <li>• Investigated by Russia, UK and USA.</li> <li>• Not implemented anywhere.</li> <li>• Laboratory studies performed in the UK.</li> </ul>
Disposal at subduction zones	<ul style="list-style-type: none"> <li>• Investigated by USA.</li> <li>• Not implemented anywhere.</li> <li>• Not permitted by international agreements.</li> </ul>
Sea disposal	<ul style="list-style-type: none"> <li>• Implemented by Belgium, France, Federal Republic of Germany, Italy, Japan, Netherlands, Russia, South Korea, Switzerland, UK and USA.</li> <li>• Not permitted by International agreements.</li> </ul>
Sub seabed disposal	<ul style="list-style-type: none"> <li>• Investigated by Sweden and UK (and organizations such as the OECD Nuclear Energy Agency).</li> <li>• Not implemented anywhere.</li> <li>• Not permitted by international agreements.</li> </ul>
Disposal in ice sheets (proposed for wastes that are heat-generating)	<ul style="list-style-type: none"> <li>• Investigated by USA.</li> <li>• Rejected by countries that have signed the Antarctic Treaty or committed to providing solutions within national boundaries.</li> </ul>
Direct injection (only suitable for liquid wastes)	<ul style="list-style-type: none"> <li>• Investigated by Russia and USA.</li> <li>• Implemented in Russia for 40 years and in USA</li> <li>• Investigations abandoned in USA in favor of deep geological disposal of solid wastes.</li> </ul>

Requirements for and implementation of the reversibility of radioactive waste disposal in geological repositories are also being considered in various countries. While the debate is not yet closed on these issues, the progress which has been made in the scientific and technical aspects of geological disposal over recent decades gives assurance to the waste management community that this is a fine technical solution which is supported by good scientific understanding.

## **1.1 The geological underground disposal**

Disposal of radioactive wastes in a deep stable geological environment is intended to provide sufficient isolation, both from human activity and from dynamic natural processes that eventual releases of radionuclides will be in such low concentrations that they do not pose a hazard to human health and the natural environment.

A geological disposal system can be defined as a combination of conditioned and packaged solid wastes and other engineered barriers within an excavated or drilled repository located at a depth of some hundreds of meters in a stable geological environment. The geologic formation, in which the waste is emplaced, referred to as the 'host rock', generally constitutes the most important isolation barrier. The various barriers act in concert, initially to contain the radionuclides, therefore allowing them to decay, and then to limit their releases to the accessible environment.

Disposal of radioactive wastes in a deep stable geological environment is intended to provide sufficient isolation, both from human activity and from dynamic natural processes, that eventual releases of radionuclides will be in such

low concentrations that they do not pose a hazard to human health and the natural environment.

A geological disposal system can be defined as a combination of conditioned and packaged solid wastes and other engineered barriers within an excavated or drilled repository located at a depth of some hundreds of meters in a stable geological environment. The geological formation in which the waste is emplaced, referred to as the 'host rock', generally constitutes the most important isolation barrier. The various barriers act in concert, initially to contain the radionuclides, therefore allowing them to decay, and then to limit their releases to the accessible environment.

A well chosen geological environment will act as a cocoon for the repository, protecting it from gross fluctuations in physical stress, water flow and hydrochemistry. Suitable geological environments for disposal of long lived radioactive wastes exist widely throughout the world. They can vary considerably in their nature and, thus, provide the desirable features mentioned above in different combinations and to different extents. Typically, suitable environments can be found in:

- 1) Extremely low permeability rocks in which advective groundwater flow is essentially precluded. These include massive evaporite deposits, such as salt domes and large formations of bedded salt, and some plastic clay and mudrock formations. In such host rocks, provided geological stability is maintained, there is no natural mechanism for water-borne radionuclide release to surrounding geological formations other than extremely slow diffusion through pore waters and along crystal boundaries, unless the presence of the repository itself adversely

affects host rock stability.

2) Deep groundwater systems which have displayed stable extremely low natural advective fluxes for periods of hundreds of thousands of years or longer. Typically, the groundwater in such systems would be saline, and possibly even dense brine, as a result of the largely stagnant nature of the groundwater system, isolated from significant fresh water recharge. It would also be chemically reducing, which minimizes the mobilization and transport potential of many radionuclides.

3) Groundwater systems which have low fluxes combined with long transport paths away from the disposal zone to potentially accessible groundwater systems or to the biosphere. Such environments might display thick (hundreds of meters) stable unsaturated zones (the region above the water table) and slow long distance migration pathways in deep groundwater bodies. They may also occur in saturated rocks in some coastal regions or in massive sedimentary basins, where infiltrating groundwater moves slowly to great depths before eventual discharge, perhaps with considerable mixing and extensive dilution in near surface waters.

Experience in many countries over the last twenty or thirty years has shown that acceptable conditions can be found in such diverse rock types as granites, metamorphic basement rocks, plastic clays, more indurated clay stones, bedded evaporites, salt domes, porous volcanic tuffs, highly compacted volcanic tuffs and various well lithified sedimentary or volcano sedimentary formations (Table 1.2).

Table 1.2 Host rock types for the geological disposal of solid radioactive waste

Host rock types	Examples
Crystalline rocks	
Granite	Canada, China, Japan, Finland,
Gneiss	Sweden
Argillaceous formations	
Strongly consolidated clays: claystone, mudstone	Hungary, Japan
Consolidated clays: shale, marl	France, Switzerland
Plastic clay	Belgium
Rock salt	
Bedded salt	USA
Salt domes	Germany
Volcanic tuffs	
Above water table	USA

## 1.2 Review of related researches

Groundwater has been a critical issue in geosphere environmental fields and has been researched from various perspectives. For example, construction of underground large and long-term use repositories such as high-level radioactive waste (HLW) disposal requires thorough understanding of groundwater systems, including hydrogeology, geologic structure, hydrochemistry, petrophysical and hydraulic properties, and fluid flow. Moreover, because of the complexity of such systems and limited quantities and locations of investigative data, understanding groundwater systems is difficult and involves uncertainty. Therefore, spatial modeling techniques are indispensable to accurately clarify these systems using the limited data.

Sedimentary rocks are confined to Earth's outer crust; they cover nearly

three-fourths of Earth's land surface and most of the ocean floor. Such rocks can be classified into three fundamental groups on the basis of composition and origin (Boggs, 2006): siliciclastic, chemical/biochemical, and carbonaceous. Siliciclastic sedimentary rocks are composed dominantly of silicate minerals, such as quartz and feldspar, and rock fragments. These materials originate mainly by the chemical and physical breakdown (weathering) of igneous, metamorphic, or older sedimentary rock. Chemical/biochemical sedimentary rocks are composed of minerals precipitated mainly from ocean or lake water by inorganic (chemical) and/or organic (biogenic) processes. Carbonaceous sedimentary rocks contain a substantial amount of highly altered remains of the soft tissue of plants and animals, referred to as organic matter. The general rock type is summarized in table 1.3.

The siliceous hard shale of marine diatomaceous and derived rocks exist extensively in the lower Pliocene and Miocene sections of northern Japan and the northern pacific region (M. E. Tucker, 2001). In Japan, they were deposited in three major Neogene sedimentary basins: East Hokkaido, Central Hokkaido, and Southwest Hokkaido to Tohoku (Tada and Iijima, 1983). Moreover, sedimentary rocks are also abundant in central part seaside and northern Kyushu (Fig. 1.1).

Groundwater systems in sedimentary rock are one of the main topics of HLW disposal technology development worldwide (Simmons *et al.*, 2002; Yager *et al.*, 2007; Beauheim *et al.*, 2014). This is because of the favorable characteristics of sedimentary rock for long-term HLW disposal repositories, which have low permeability, a small diffusion coefficient, and low adsorption capacity for radionuclides (Krooss and Leythaeuser, 1988; Neuzil, 2003; Rutqvist and

Stephansson, 2003; Omar *et al.*, 2009).

### Fault zone hydrology

As the plumbing of the earth, fault zones in the shallow crust impact a suite of geological processes. Functions of fault zones are variable as conduit or barrier systems of fluid flow, as seen in many studies on the safety of potential HLW repositories (Ferrill *et al.*, 1999; Douglas *et al.*, 2000; Flint *et al.*, 2001),

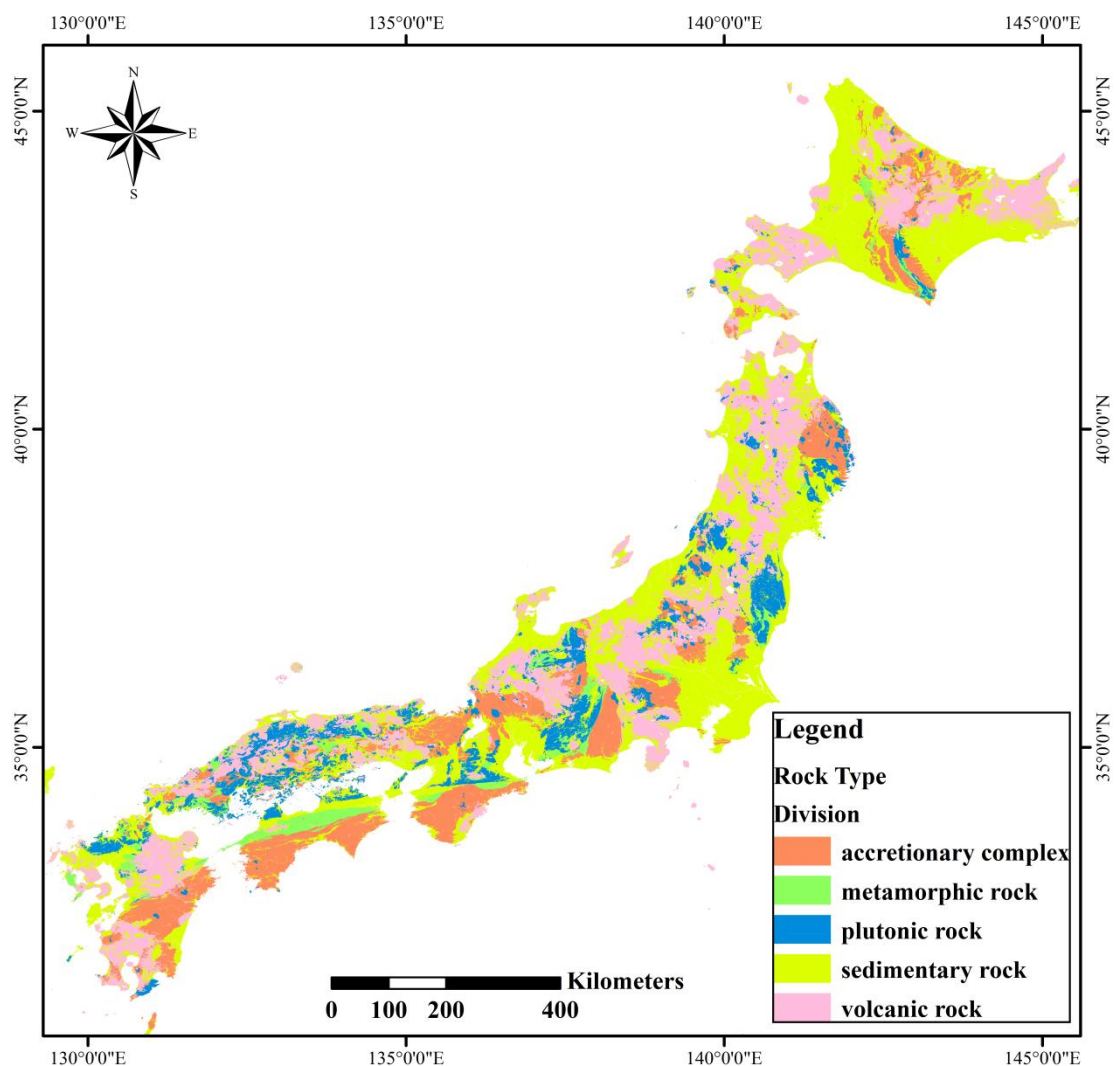


Fig. 1.1 Brief rock type in Japan

Table 1.3 Principal groups of sedimentary rock

Siliciclastic sediments	Chemical/biochemical sediments	Carbonaceous sediments
conglomerates, sandstones, mudrocks, and shales	limestone, chert, evaporites (gypsum, phosphorites), and ironstone	coal and oil shale

aquifers (Lachmar, 1994; Bense and Person, 2006; Mayer *et al.*, 2007; Gassiat *et al.*, 2013), geothermal reservoir exploration (Tarcan and Gemici, 2003; Teng and Koike, 2007; Seebeck *et al.*, 2010; Llanos *et al.*, 2015), and CO<sub>2</sub> capture and storage (Annunziatellis *et al.*, 2008; Shukla *et al.*, 2010; Castelletto *et al.*, 2013).

Darcy's Law as fundamental law of fluid flow through porous media illustrates that underground fluid flow is governed by rock permeability and the hydraulic gradient within the rock mass. Structural geological tools used to explore deformation processes as well as internal structure and architecture of fault zone structure is crucial to obtain a major understanding of the permeability structure of fault zones. However, hydraulic gradients within fault zones are greatly governed by hydrological processes such as groundwater recharge rates that force topography-driven flow, and other processes like fluid flow driven by sediment compaction. Therefore, checking hydraulic gradients display near fault zones and delineation of fluid flow pathways in fault zones by performing tools from hydrogeology should also be important in development of a comprehensive understanding of the role of fault zones in hydrogeology (Karasaki *et al.*, 2008). Although there is a noticeable volume of researches in hydrogeology and structural geology fields about fault and groundwater, there is limited evidence of an

exchange of insights or integration between them.

Structural geological studies usually focus on surface, by using methods like outcrop investigation of fault zone properties, such as the length, orientation and porosity to collect the permeability of fault rocks. From outcrop investigation, a array of conceptual hydrological models have been researched in the literature suggesting that faults play as barriers impeding fluid flow, as conduits proliferating fluid flow, or even as conduit–barrier systems (Caine *et al.*, 1996; Aydin, 2000; Rawling *et al.*, 2001; Bense and Person, 2006). However, direct hydrological indications of the influences of specific faults on fluid flow to test and refine these surface based fault models are very limited.

Hydrological studies usually focus on underground, by interpreting the hydrological performance of fault zones from sets of boreholes and wells normally without investigating fault structure straightly from surface data such as outcrop. Usually it is not so often that hydrological studies is co-located in the fault zones, because groundwater monitoring systems are aimed to characterize hydrological properties of aquifers. Therefore, densely distributed sets of boreholes over fault zones are rare. However, the shape of the hydraulic head profile that might show steps or inflections in hydraulic gradient at fault zones can be used to infer the directions and rate of fluid flow at the fault zone (e.g. Haneberg, 1995; Bense *et al.*, 2003; Anderson and Bakker, 2008) and provide an indication of the hydrogeological behavior of a fault zone as a barrier or a conduit. Groundwater temperature, geochemistry and age (e.g., Bethke and Johnson, 2008; Leray *et al.*, 2012) can constrain groundwater flow paths across fault zones in conjunction with hydraulic head observations. Boreholes can also be used for hydraulic testing with

packer or pumping tests to enhance groundwater flow rates around fault zones to elucidate the fault zone hydrogeological structure (Anderson and Bakker, 2008). Sampling groundwater geochemistry, measuring hydraulic head, temperature and other parameters during pumping tests can result in detailed inferences on fault zone hydrogeological properties.

Differences in the methodologies used by hydrogeologists and structural geologists are partly due to contrasts in the type of data available in field areas. Dense networks of wells available to collect detailed hydrogeological evidence on fault behavior are typically found in developed areas where outcrops that are necessary for structural geological outcrop-based studies are usually sparse. Vice versa, where fault zones are well exposed in outcrop, a dense network of wells is often not available as these areas are generally less developed and the groundwater is not near the surface. Therefore, probably in part due to the differences in methods, data availability and field areas, there is limited evidence of an exchange of insights or integration between hydrogeology and structural geological disciplines.

Each method used by structural geologists and hydrogeologists has a characteristic scale over which the method integrates observations. Consequently, the use of the different methods results in faults being examined at various scales by the two disciplines. Generally, the methods used by structural geologists examine smaller integration scales of <0.01 m (microstructure) to e.g. 100 m (outcrop studies) whereas hydrogeologists often also infer fault hydrogeological behavior at larger integration scales of e.g. >10km. Most of the methods used by hydrogeologists integrate over larger scales than the typical width of many fault cores, which suggests that hydrogeological methods can only infer the effective

hydrogeological impact of fault zones rather than constrain the internal permeability structure of fault zones. Conversely, it may be difficult to elucidate a regional impact of faults on fluid flow from the smaller scale studies conducted by structural geologists (Bense *et al.*, 2013).

### **Groundwater in sedimentary rock**

Pore water with salinities commonly ranging from 5000 to  $3 \times 10^5$  mg/l TDS (total dissolved solids) comprises ~20% of most sedimentary basins (e.g., Hanor, 1987; Kharaka and Thordsen, 1992). This water, which is generally sampled while drilling for petroleum or is co-produced with oil and gas, has in situ temperatures of ~20 to >150 °C and fluid pressures of ~100 to ~1000 bar. The chemical and isotopic compositions of this water provide important information on the geochemical, hydrologic, thermal, and tectonic evolution of the Earth's crust. Deep basinal water is an important crustal reservoir of mobile elements, such as the halogens, and fluid and solute fluxes between this water and surface continental water and the oceans are an integral part of the hydrologic and exogenic cycles. Water in sedimentary basins also acts as an intermediate reservoir for volatiles degassing from the lower crust and mantle and as such can be used to study deep-seated processes (Ballentine and O'Nions, 1991; Kennedy *et al.*, 1997).

The geochemistry of basinal waters provides insight into a number of important processes that occur within sedimentary basins, especially the (1) generation, transport, accumulation, and production of petroleum; (2) chemical aspects of mineral diagenesis, including dissolution, precipitation, and the alteration of sediment porosity and permeability; (3) transport and precipitation of

copper, uranium; (4) tectonic deformation; (5) transport of thermal energy for geothermal and geo-pressured–geothermal systems; and (6) interaction, movement, and ultimate fate of large quantities of liquid hazardous wastes injected into the subsurface (Hanor *et al.*, 1988; Kharaka and Thordsen, 1992; Tuncay *et al.*, 2000).

There are probable two main reasons for interest in the geochemistry of formation waters in the past decades years. First, depleted petroleum fields and saline aquifers in sedimentary basins are being investigated as possible repositories for the storage of large amounts of anthropogenic CO<sub>2</sub> in the subsurface for thousands of years, thus moderating the anticipated future increases in the concentrations of atmospheric CO<sub>2</sub> and mitigating global warming, arguably the most important environmental issue facing the world today (Herzog and Drake, 1998; White *et al.*, 2003; Kharaka *et al.*, 2006). The success of such operations will depend largely on understanding water–mineral–CO<sub>2</sub> interactions in the subsurface (Hitchon, 1996; Gunter *et al.*, 2000). Second, petroleum production, drilling operations, and improperly sealed abandoned wells have caused major contamination of surface and groundwater and soils in energy-producing states throughout the world (Richter and Kreitler, 1993; Kharaka *et al.*, 1995; Kharaka and Dorsey, 2005).

The history of thought on the origin of saline subsurface water dates back to ancient times (White *et al.*, 1963; Hanor, 1983, 1987). With the rapid development of the oil and gas industry in the early twentieth century, a large database for the composition of formation waters co-produced with hydrocarbons became available. This led to further development of hypotheses regarding the origin of

basinal waters (Warren and Smalley, 1994; Breit *et al.*, 2001).

The short section here reviews what is known about the geochemistry of water in sedimentary basins. The emphasis is on water below the zone of shallow meteoric groundwater circulation, and on the main processes that are responsible for the modification of the chemical and isotopic composition of these waters including (Kharaka and Hanor, 2005): (1) mixing; (2) dissolution of evaporites, especially halite; (3) reflux and incorporation of bitterns, the residual water remaining after the precipitation of evaporites; (4) dissolution and precipitation of minerals other than evaporites; (5) interaction with rocks, principally clays, siltstone, and shale that behave as geological membranes; (6) interactions with organics, including petroleum and solid organic matter; and (7) diffusion, especially in and near salt domes.

### **1.3 Problem statement**

Sedimentary rocks are extensively exist in Japan as shown in Fig. 1.1, although some research sites, like Horonobe Underground Research Laboratory of Japan Atomic Energy Agency (JAEA), focus deep groundwater modeling in sedimentary rock (Hama *et al.*, 2007; Sasamoto *et al.*, 2011; Kozai *et al.*, 2013; Ikawa *et al.*, 2014), functions of the faults have not been well understood.

Fluid flow in the upper crust relies on fault geometry and fault zone structure composed of a fault core and damage zone (Caine *et al.*, 1996). This is because the fault zone strongly affects hydraulic conductivity and hydraulic gradient, which in turn control groundwater flow patterns. There have been many studies of regional hydrogeochemical characteristics and groundwater modeling for

sedimentary rocks (Bense *et al.*, 2003; Tarcan and Gemici, 2003; Folch and Mas-Pla, 2008; Beauheim *et al.*; 2014). However, few have provided insights from an interdisciplinary perspective, honoring fault structures in three dimensions.

Moreover, the contribution of structural geology, hydrogeology, and hydrogeochemistry to the study of fault zone hydrogeology in sedimentary rock can largely be told as above. To gain a more integrated, comprehensive understanding of this setting study, challenges could still be summarized as follows: 1) Colocated study areas to better use hydrogeological and geochemical data to test conceptual models derived from surface-focused studies (geological structure). This would involve targeted drilling and well studied outcrops along strike in the well-instrumented well fields. 2) Better integrate approaches and data fusion from structural geology, hydrogeology and geochemistry, use multidisciplinary methods such as geophysics, petroleum geology and spatial modeling.

Therefore, detailed delineation of fault structure and clarification of its spatial relationship with hydrochemistry are crucial for groundwater systems, which requires an interdisciplinary perspective, integrated methods, and data integration.

### **1.3 Main objective**

The Horonobe Underground Research Laboratory (HURL) was established to strengthen the reliability of relevant disposal technologies via investigations and research on the deep geological environment of sedimentary host rocks.

This study uses the Horonobe area of northern Japan as an illustration for the

regional fault zone groundwater modeling in sedimentary rock. The selection of study area owes to the availability of a unique dataset from deep borehole logging data. Geostatistical techniques suitable for clarifying hydrochemical properties from a limited dataset are identified. Based on the above background, the present study aims to regionally characterize hydrochemical properties of groundwater in a sedimentary rock area; clarify their correlation with geologic and fault structures; interpret the groundwater source and chemical evolution; and generate a generic modeling that could be applied in other underground researches in Japan.

#### **1.4 Originality and contributions**

The research of this dissertation generated several contributions to fault zone hydrogeology and underground water modeling. Originality of this research can be summarized by the following three points:

- In comparison with traditional hydrologic research, a groundwater modeling pattern was proposed in this work. This modeling pattern considers geological structure in three-dimension, especially a regional fault zone. It is an integrated model that combined different data source, geophysical and geochemical perspective.

- As for a sparse dataset, only ten boreholes, in study area, this research successfully proposed a possible solution that integrated ‘hard data’ (groundwater salinity data) with ‘soft data’ (resistivity logging data) by conditional simulation to solve the spatial interpolation.

- The effectiveness of fault dip towards groundwater distribution and

evolution was significantly and probable firstly depicted in the geostatistical analysis as a parameter. This means a statistical-geological-geochemical treatment in such complex research is indispensable, and moreover, can be developed to a generic model for sedimentary host rock underground research in Japan and world.

Based on those perspective and ideas, it is strongly believe that the originality and contribution in this dissertation is high and can be widely used to similar underground research and exploration.

## **1.5 Thesis structure**

Chapter 1 describe about the introduction of this study which includes problem statement, main objectives, and research flow.

Chapter 2 introduce about spatial random process and the methodologies to handle data from spatial random process. That includes geostatistical process estimation, geostatistical process simulation.

Chapter 3 introduce about the site area chosen in this study and the preliminary data processing. The background of study area includes geology, geography, hydrology, geophysics, geochemistry, borehole logging process. The preliminary data processing includes the data acquisition, data revision, data fusion from different source.

Chapter 4 introduce about the geostatistics-based analysis of groundwater properties integrated with geological structure in 3D. The analysis include Kriging paradigm estimation of hydrogeochemistry data, and also the stochastic simulation of these index.

Chapter 5 introduce about origin and evolution analysis of groundwater in sedimentary rock area. The origin analysis employs the stable isotope to indicate the groundwater type with geological classification. The evolution analysis integrated the stable isotope data with a fault zone clarification to show the regional groundwater flow pattern under the effect of the local main (Omagari) fault damage zone.

Chapter 6 introduce about the conclusion and future work. Conclusion includes the necessary discussions on the deep groundwater system modeling in this study. Based on these useful discussions, we could find there are some interesting points worth improving more works to get better results.

## **1.6 Summary**

This chapter aims to introduce the background, motivation and structure of this dissertation. The background was first introduced from the need of underground water modeling in radioactive waste especially high level nuclear waste disposal. Then are the major problems that need to be solved. The motivation of each problem was pointed out and then the originality and contributions of this dissertation were introduced. Finally, the structure of this dissertation was listed.

## **Chapter 2**

### **Spatial Multivariate Modeling**

This chapter is aimed to set the scene for what follows by introducing the development of spatial statistics as a noticeable sub-branch of the statistics discipline and the methods used in this study. As with many other areas of statistical methodology, the important developments came not from the study of mathematics for its own sake, but from the needs of substantive applications, including in this case areas as diverse as astronomy, agriculture, ecology and mineral exploration.

#### **2.1 The beginning of spatial variant**

The fundamental feature of spatial statistics is its concern with phenomena whose spatial location is either of intrinsic interest or contributes directly to a stochastic model for the phenomenon in question. You are here. What happens north, south, east, or west of you is very likely to be (positively) dependent on what is happening here. Spatial considerations were implicit in R. A. Fisher's

(1966) seminal work on the development of design-based inference for data from agricultural field trials at the Rothamsted Experimental Station in Hertfordshire, England. Fisher recognized that near-neighboring plots tend to give similar yields, thus violating the assumption of mutually independent perturbations. Fisher commented this difficulty as “the widely verified fact that patches in close proximity are commonly more alike, as judged by the yield of crops, than those which are farther apart” (Fisher, 1966, p. 66). This expresses a “law of Geography” that says nearby things tend to be more alike than those far apart. Because there is a flux of causal relationships in the space–time continuum that, when integrated out over time or captured in a micro-instant of time, shows neighboring values to be more highly correlated. A caveat that should be mentioned is that physical barriers like rivers and mountains can affect what is meant by “nearby” or “neighboring.” Also, the presence of competition can lead to correlations that are negative; to put a biological face on the point, under big trees only small trees can grow.

## **2.2 Modeling continuous spatial variation**

A less ambitious and more realistic goal than a search for a universal law is to develop a parsimonious class of models that can succeed in capturing the empirical behavior of spatial variation in a range of assumptions. From this point of view, a convenient working assumption is that the spatial phenomenon under investigation can be modeled as a Gaussian spatial process,  $S(x)$ , whose mean can be described by a suitable linear model. To complete the specification of the model, we then need only to specify the covariance between  $S(x)$  and  $S(x')$  for

any two locations,  $x$  and  $x'$ . This task is considerably simplified if we are prepared to assume spatial stationarity, in which case the covariance specification reduces to a scalar parameter  $\delta^2 = \text{Var}\{S(x)\}$  and a correlation function  $\rho(u) = \text{Corr}\{S(x), S(x')\}$  where  $u$  is the distance between  $x$  and  $x'$ .

It took a while for this idea to bear fruit, and when it did, it did so independently in at least two very different fields: forestry (Matern, 1960) and mining engineering (Krige, 1951).

Bertil Matern set out the class of models for the correlation structure of real-valued, spatially continuous stationary processes that now bear his name. The Matern correlation function takes the form

$$\rho(u) = \{2^{k-1}\Gamma(k)\}^{-1}(u/\phi)^k K_k(u/\phi),$$

where  $\phi$  is a scale parameter and  $K_k(\cdot)$  denotes a modified Bessel function of order  $k$ . One of the attractions of this class of models is that the integer part of  $k$  determines the mean square differentiability of the underlying process.

D. G. Krige was for many years a professor at the University of the Witwatersrand, South Africa. He promoted the use of statistical methods in mineral exploration and, in Krige (1951), set the seeds for the later development, by Georges Matheron and colleagues at LEcole des Mines in Fontainebleau, France, of the branch of spatial statistics known as geostatistics. The spatial prediction method known as kriging is named in his honor. In a different scientific setting, the objective analysis of Gandin (1960), essentially the same thing as kriging, was for a long time the standard tool for constructing spatially continuous weather maps from spatially discrete observations on the ground and in the air.

## **Geostatistics**

As noted above, geostatistics has its origins in the South African mining industry, but was developed into a self-contained methodology for spatial prediction at LEcole des Mines, Fontainebleau, France (Matheron, 1955, 1963, 1965). The original practical problem for which geostatistical methods were developed is to predict the likely yield of a mining operation over a spatial region  $D$ , given the results of samples of ore extracted from a finite set of locations. Put more formally, suppose that  $S(x)$  is a spatially continuous random process and that data  $Y_i : i = 1, \dots, n$  are obtained as, possibly noise-corrupted versions of, the realized values of  $S(x)$  at sampling locations  $x_i : i = 1, \dots, n$ , hence  $Y_i = S(x_i) + U_i$  where the  $U_i$  are independent with mean zero and variance  $\tau^2$ . Let  $T = \int_D S(x)dx$ . Then, the basic geostatistical problem is to use the data  $Y_i : i = 1, \dots, n$  to make predictive inference about  $T$ . In its simplest manifestation (called, not unreasonably, *simple kriging*), the process  $S(\cdot)$  is assumed to have constant mean, estimated by the sample mean of the data, and known covariance structure. The point predictor of  $T$  is then the integral of the best (in mean square error sense) linear predictor of  $S(x)$ . A somewhat better method, known as the *ordinary kriging*, replaces the sample mean by the generalized least squares estimate of  $\mu$ , thereby taking account of the estimated covariance structure of  $S(\cdot)$ . A further extension, called *universal kriging*, replaces the constant mean  $\mu$  by a regression model,  $\mu(x) = d(x)'\beta$ , where  $d(x)$  is a vector of spatially referenced explanatory variables.

## 2.3 Spatial Random Processes

A spatial process can be a temporal snapshot, a temporal aggregation, or a temporally frozen state of a space–time process. Aggregation over longer time scales occurs in studies of climate; climate is sometimes characterized as a long-term average of daily weather, although we prefer to think of it as a long-term statistical distribution. Finally, an ore deposit deep underground represents a temporally “frozen” state in the evolution of its mineralization.

Some probabilistic theory for such processes shall be reviewed before introducing geostatistics.

### 2.3.1. Spatial Random field

In this section, we consider probability models for a spatial variable that varies over a continuous domain of interest,  $D \subset \mathbb{R}^d$ , where the spatial dimension is typically  $d = 2$  or  $d = 3$ . The approach relies on the notion of a spatial stochastic process  $\{Y(\mathbf{s}): \mathbf{s} \in D \subseteq \mathbb{R}^d\}$ , in the sense that

$$Y(\mathbf{s}) = Y(\mathbf{s}, \omega) \quad (2.1)$$

is a collection of random variables (RV), where  $\mathbf{s} \in D \subseteq \mathbb{R}^d$  is spatial location,  $\omega \in \Omega$  is realization chance.

At any single spatial location  $\mathbf{s} \in D$ , we think of  $Y(\mathbf{s})$  as a random variable that can more fully be written as  $Y(\mathbf{s}, \omega)$ , where the elementary event  $\omega$  lies in some abstract sample space,  $\Omega$ . If we restrict attention to any fixed, finite set of spatial locations  $\{\mathbf{s}_1, \dots, \mathbf{s}_n\} \subset D$ , then

$$(Y(\mathbf{s}_1), \dots, Y(\mathbf{s}_n))^T$$

is a random vector, whose multivariate distribution reflects the spatial

dependencies in the variable of interest. Each component corresponds to a spatial site. Conversely, if we fix any elementary event  $\omega \in \Omega$ , then

$$\{Y(\mathbf{s}): \mathbf{s} \in D \subseteq \mathbb{R}^d\} \text{ and } (y_1, \dots, y_n)^T = (Y(\mathbf{s}_1, \omega), \dots, Y(\mathbf{s}_n, \omega))^T$$

are realizations of the spatial stochastic process (2.1).

In applications, it is important to ensure a valid mathematical specification of the spatial stochastic process. The celebrated Kolmogorov existence theorem states that the stochastic process model is valid if the family of the finite-dimensional joint distributions is consistent under reordering of the sites and marginalization. An important special case is that of a Gaussian process where the finite-dimensional distributions are multivariate normal and characterized by their mean vectors and covariance matrices.

### 2.3.2. Stationary and Intrinsic Stationary Processes

A spatial stochastic process is called *strictly stationary* if the finite dimensional joint distributions are invariant under spatial shifts. Essentially, this means that for all vectors  $\mathbf{h} \in \mathbb{R}^d$ ,

$$F(y_1, \dots, y_n; \mathbf{s}_1 + \mathbf{h}, \dots, \mathbf{s}_n + \mathbf{h}) = F(y_1, \dots, y_n; \mathbf{s}_1, \dots, \mathbf{s}_n).$$

In the case of a Gaussian process  $\{Y(\mathbf{s}): \mathbf{s} \in \mathbb{R}^d\}$ , where the finite dimensional distributions are determined by their second-order properties, then it is, in particular, that

$$E(Y(\mathbf{s})) = E(Y(\mathbf{s} + \mathbf{h})) = \mu$$

and

$$\text{Cov}(Y(\mathbf{s}), Y(\mathbf{s} + \mathbf{h})) = \text{Cov}(Y(\mathbf{0}), Y(\mathbf{h})) = C(\mathbf{h}),$$

where the function  $C(\mathbf{h})$ ,  $\mathbf{h} \in \mathbb{R}^d$ , is the *covariance function*. A process

which satisfies these two conditions is called *weakly stationary* or *second-order stationary*. It follows that a Gaussian process, which is second-order stationary, is also strictly stationary. This is a very special property that depends critically on the Gaussian assumption.

## 2.4 Geostatistical process estimation

Geostatistics has been successfully applied in many fields for predicting values or categories of target-regionalized variables at unsampled points from irregularly distributed, discrete sample data (e.g., Desbarats and Bachu, 1994; Yu *et al.*, 2003; Liu and Koike, 2007; Iskandar *et al.*, 2012). The essential goal of a geostatistical method is often prediction of the spatial process at locations where the process is not observed. Spatial estimation and prediction by geostatistics are undertaken by deriving the most probable value or category and generating multiple equiprobable maps at grid cells with fine interval over a grid covering the region of interest.

Suppose that a spatially distributed variable is of interest, which in theory is defined at every point over a bounded study region of interest,  $D \subset R^d$ , where  $d = 2$  or  $3$ . We suppose further that this variable has been observed (possibly with error) at each of  $n$  distinct points in  $D$ , and that from these observations we wish to make inferences about the process that governs how this variable is distributed spatially and about values of the variable at locations where it was not observed. The geostatistical approach for achieving these objectives is to assume that the observed data are a sample (at the  $n$  data locations) of one realization of a continuously indexed spatial stochastic process (random field, or random

function)  $Y(\cdot) \equiv \{Y(\mathbf{s}): \mathbf{s} \in D\}$ .

### 2.4.1. Geostatistical Model

Because only one realization of  $Y(\cdot)$  is available, and the observed data are merely an incomplete sample from that single realization, considerable structure must be imposed upon the process for inference to be possible. The classical geostatistical model imposes structure by specifying that

$$Y(\mathbf{s}) = z(\mathbf{s}) + m(\mathbf{s}), \quad (2.2)$$

where  $m(\mathbf{s}) \equiv E[Y(\mathbf{s})]$ , the mean function, is assumed to be deterministic and continuous, and  $z(\cdot) \equiv \{z(\mathbf{s}): \mathbf{s} \in D\}$  is a zero-mean random "error" process satisfying a stationarity assumption. One common stationarity assumption is that of second-order stationarity, which specifies that

$$\text{Cov}[z(\mathbf{s}), z(\mathbf{s}')] = C(\mathbf{s} - \mathbf{s}'), \text{ for all } \mathbf{s}, \mathbf{s}' \in D.$$

In other words, this asserts that the covariance between values of  $Y(\cdot)$  at any two locations depends on only their *relative* locations or on their spatial lag vector.

Intrinsic stationarity specifies that

$$\frac{1}{2} \text{var}[z(\mathbf{s}) - z(\mathbf{s}')] = \gamma(\mathbf{s} - \mathbf{s}') = \gamma(\mathbf{h}), \text{ for all } \mathbf{s}, \mathbf{s}' \in D. \quad (2.3)$$

The function  $\gamma(\cdot)$  defined by (2.3) is called the semivariogram (and the quantity  $2\gamma(\cdot)$  is known as the variogram). A second-order stationary random process with covariance function  $C(\cdot)$  is intrinsically stationary, with semivariogram given by

$$\gamma(\mathbf{h}) = C(\mathbf{0}) - C(\mathbf{h}),$$

The variogram can be used in some cases where a covariance function does not exist. More generally, Matheron introduced the class of the *intrinsically*

*stationary* processes, which are such that certain spatial increments are second-order stationary, so that a *generalized covariance function* can be defined. More details can be found in Cressie (1993), and Chiles and Delfiner (1999).

Model (2.2) purports to account for large-scale spatial variation (trend) through the mean function  $m(\cdot)$ , and for small-scale spatial variation (spatial dependence) through the process  $z(\cdot)$ . In practice, however, it is usually not possible to unambiguously identify and separate these two components using the available data. Like Cressie (1991) comments “One person’s deterministic mean structure may be another person’s correlated error structure.” Consequently, it will have to settle for a plausible, but admittedly nonunique, decomposition of spatial variation into large-scale and small-scale components.

In addition to capturing the small-scale spatial variation, the error process  $z(\cdot)$  in (2.2) accounts for measurement error that may occur in the data collection process. This measurement error component typically has no spatial structure; hence, for some purposes it may be desirable to explicitly separate it from the spatially dependent component. That is, it may write

$$z(\mathbf{s}) = \eta(\mathbf{s}) + \varphi(\mathbf{s}), \quad (2.4)$$

where  $\eta(\cdot)$  is the spatially dependent component and  $\varphi(\cdot)$  is the measurement error.

The stationarity assumptions introduced above specify that the covariance or semivariogram depends on locations  $\mathbf{s}$  and  $\mathbf{s}'$  only through their lag vector  $\mathbf{h} = \mathbf{s} - \mathbf{s}'$ . A stronger property not needed for making inference from a single sampled realization but important nonetheless is isotropy. Here describe just intrinsic isotropy; second-order isotropy differs only by imposing an analogous

condition on the covariance function rather than the semivariogram. An intrinsically stationary random process with semivariogram  $\gamma(\cdot)$  is said to be (intrinsically) isotropic if  $\gamma(\mathbf{h}) = \gamma(h)$ ; that is, the semivariogram is a function of the locations only through the (Euclidean) distance between them. If the process is not isotropic, it is said to be anisotropic. Perhaps the most tractable form of anisotropy is geometric anisotropy, for which  $\gamma(\mathbf{h}) = \gamma((\mathbf{h}'\mathbf{A}\mathbf{h})^{1/2})$  where  $\mathbf{A}$  is a positive definite matrix. Isotropy can be regarded as a special case of geometric anisotropy in which  $\mathbf{A}$  is an identity matrix.

The objectives of a geostatistical analysis can now be expressed more specifically in terms of model (2.2). Characterization of the spatial structure is tantamount to the estimation of  $m(\cdot)$  and either  $C(\cdot)$  or  $\gamma(\cdot)$ . The prediction objective can be expressed as seeking to predict the value of  $Y(\mathbf{s}_0) = m(\mathbf{s}_0) + z(\mathbf{s}_0)$  at an arbitrary site  $\mathbf{s}_0$ .

#### 2.4.2. Estimation of the Semivariogram

The primary stage of a geostatistical analysis is to estimate the second-order dependence structure of the random process  $Y(\cdot)$  from the residuals of the fitted provisional mean function. To describe this in more detail, we assume that  $z(\cdot)$  is intrinsically stationary, in which case the semivariogram is the appropriate mode of description of the second-order dependence.

Consider first a situation in which the data locations form a regular rectangular grid. Let  $\mathbf{h}_1 = \begin{pmatrix} h_{11} \\ h_{12} \end{pmatrix}, \dots, \mathbf{h}_k = \begin{pmatrix} h_{k1} \\ h_{k2} \end{pmatrix}$  represent the distinct lags between data locations (in units of the grid spacings), with displacement angles  $\phi_u = \tan^{-1}(h_{u2}/h_{u1}) \in [0, \pi)$  ( $u = 1, \dots, k$ ). Attention may be restricted to

only those lags with displacement angles in  $[0, \pi)$  without any loss of information because  $\gamma(h)$  is an even function. For  $u = 1, \dots, k$ , let  $N(\mathbf{h}_u)$  represent the number of times that lag  $\mathbf{h}_u$  occurs among the data locations. Then the empirical semivariogram (sample semivariogram) is defined as follows:

$$\hat{\gamma}(\mathbf{h}_u) = \frac{1}{2N(\mathbf{h}_u)} \sum_{s_i - s_j} \{\hat{z}(s_i) - \hat{z}(s_j)\}^2 \quad (u = 1, \dots, k)$$

Under model (2.2) with constant mean, this estimator is unbiased; if the mean is not constant in model (2.2), the estimator is biased as a consequence of estimating the mean structure, but the bias is not large in practice.

When data locations are irregularly spaced, there is generally little to no replication of lags among the data locations. To obtain quasi-replication of lags, first partition the lag space  $H = \{\mathbf{s} - \mathbf{s}': \mathbf{s}, \mathbf{s}' \in D\}$  into lag classes  $H_1, \dots, H_k$ , and assign each lag with displacement angle in  $[0, \pi)$  that occurs among the data locations to one of the classes. Then, a similar estimator:

$$\hat{\gamma}(\mathbf{h}_u) = \frac{1}{2N(H_u)} \sum_{s_i - s_j \in H_u} \{\hat{z}(s_i) - \hat{z}(s_j)\}^2 \quad (u = 1, \dots, k)$$

Here  $\mathbf{h}_u$  is a representative lag for the entire bin  $H_u$ , and  $N(H_u)$  is the number of lags that fall into  $H_u$ .

One undesirable feature of the empirical semivariogram is its sensitivity to outliers, a consequence of each of its ordinates being a scaled sum of squares. An alternative and more robust estimator is (Cressie and Hawkins, 1980),

$$\bar{\gamma}(\mathbf{h}_u) = \frac{\left\{ \frac{1}{N(H_u)} \sum_{s_i - s_j \in H_u} |\hat{z}(s_i) - \hat{z}(s_j)|^{1/2} \right\}^4}{0.914 + [0.988/N(H_u)]}$$

### 2.4.3. Modeling the Semivariogram

Next, it is standard practice to smooth the empirical semivariogram by fitting a parametric model to it. There are several reasons for smoothing semivariogram. First, it is often quite bumpy; a smoothed version could be more reliable (have smaller variance) and therefore may increase understanding of the nature of the spatial dependence. Second, the empirical semivariogram will often fail to be conditionally non-positive definite, a property which must be satisfied to ensure that at the prediction stage to come, the prediction error variance is nonnegative at every point in  $D$ . Finally, prediction at arbitrary locations requires estimates of the semivariogram at lags not included among the class representatives  $\mathbf{h}_1, \dots, \mathbf{h}_k$  nor existing among the lags between data locations, and smoothing can provide these needed estimates.

To smooth the empirical semivariogram, a valid parametric model for the semivariogram and a method for fitting that model must be chosen. The choice of model among the collection of valid semivariogram models is informed by an examination of the empirical semivariogram, and also other considerations, like, conditional negative definiteness

$$\sum_{i=1}^n \sum_{j=1}^n a_i a_j \gamma(\mathbf{s}_i - \mathbf{s}_j) \leq 0 \text{ for all } n, \mathbf{s}_1, \dots, \mathbf{s}_n, \text{ and all } a_1, \dots, a_n, \text{ that } \sum_{i=1}^n a_i = 0$$

Often, the empirical semivariogram tends to increase roughly with distance in any given direction, up to some point at least, indicating that the spatial dependence decays with distance. In other words, values of  $Y(\cdot)$  at distant locations tend to be less alike than values at locations in close proximity.

A large variety of models satisfy the aforementioned validity requirements in

$R^2$  and  $R^3$  (Cressie, 1993), the following four appear to be the most commonly used (Fig. 2.1):

*Spherical*

$$\gamma(h) = \begin{cases} c \left( \frac{3h}{2a} - \frac{h^3}{2a^2} \right) & \text{for } 0 \leq h \leq a \\ 0 & \text{for } h \geq a \end{cases}$$

*Exponential*

$$\gamma(h) = c \left( 1 - \exp \left( -\frac{h}{a} \right) \right)$$

*Gaussian*

$$\gamma(h) = c \left( 1 - \exp \left( -\frac{h^2}{a^2} \right) \right)$$

*Power*

$$\gamma(h) = ch^a$$

For each of these models,  $c$  is positive; similarly,  $a$  is positive in each model except the power model, for which it must satisfy  $0 \leq a < 2$ .

Several attributes of an isotropic semivariogram model are sufficiently important to point out. The *sill* of  $\gamma(h)$  is defined as  $\lim_{h \rightarrow \infty} \gamma(h)$  provided that the limit exists. If this limit exists, then the process is not only intrinsically stationary, but also second-order stationary, and  $C(\mathbf{0})$  coincides with the sill. Note that the spherical, exponential, and Gaussian models have sills (equal to  $c$  in each of the parameterizations given above), but the power model does not.

Furthermore, if the sill exists, then the *range* of  $\gamma(h)$  is the smallest value of  $h$  for which  $\gamma(h)$  equals its sill, if such a value exists. If the range does not exist, there is a related notion of an *effective range*, defined as the smallest value of  $h$  for which  $\gamma(h)$  is equal to 95% of its sill; in this case, the effective range is often

a function of a single parameter called the *range parameter*. Of those models listed above that have a sill, only the spherical has a range (equal to  $a$ ); however, the exponential and Gaussian models have effective ranges of approximately  $3a$  and  $\sqrt{3}a$ , respectively, with  $a$  then being the range parameter.

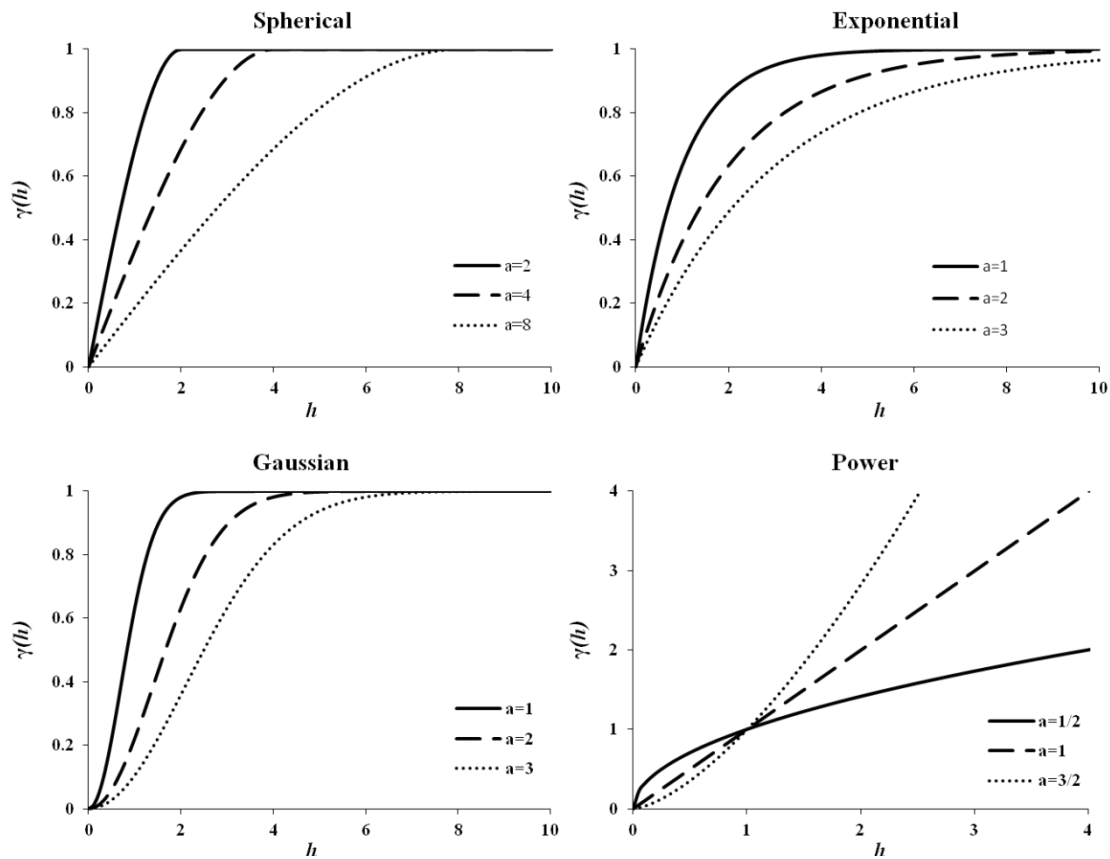


Fig. 2.1 Semivariogram models

The smoothness of the semivariogram near the origin (at small lags) is a key attribute for efficient spatial prediction (Stein, 1988; Stein and Handcock, 1989). Finally, the *nugget effect* of  $\gamma(h)$  is defined as  $\lim_{h \rightarrow 0} \gamma(h)$ . The nugget effect is zero for all the models listed above, but a nonzero nugget effect can be added to any of them. For example, the exponential model with nugget effect  $c_0$  is given

by

$$\gamma(h) = \begin{cases} c_0 + c \left(1 - \exp\left(-\frac{h}{a}\right)\right) & \text{if } h > 0 \\ 0 & \text{if } h = 0 \end{cases} \quad (2.5)$$

One rationale for the nugget effect can be given in terms of the measurement error model (2.4). If  $\eta(\cdot)$  in that model is intrinsically stationary and mean square continuous with a nuggetless exponential semivariogram,  $\varphi(\cdot)$  is an iid (white noise) measurement error process with variance  $c_0$ , and  $\eta(\cdot)$  and  $\varphi(\cdot)$  are independent, then the semivariogram of  $z(\cdot)$  will coincide with (2.5).

Two main procedures for estimating the parameters of a chosen semivariogram model have emerged: weighted least squares (WLS) and maximum likelihood (ML). The WLS approach is very popular among practitioners due to its relative simplicity.

#### **2.4.4. Cross-validating the fitted variogram**

Suppose that a variogram model  $2\gamma(\mathbf{h})$ ,  $\mathbf{h} \in \mathbb{R}^d$ , has been fitted to data  $\{Z(\mathbf{s}_i): i = 1, \dots, n\}$ . A way to diagnose any problems with the fit obtained is to *cross-validate* the variogram model.

Cross-validation has been a popular way of assessing statistical estimation and prediction since the 1970s. The basic idea is to delete some of the data and use the remaining data to predict the deleted observations. Then the prediction error can be inferred from the predicted minus actual values. Repeating this over many deleted subsets allows an assessment of the variability of prediction error.

In an estimation context, the deletion of observations to improve inference for an estimable parameter was called *jackknifing* by Tukey.

In jackknifing, the manufacture of pseudo values makes it different from the cross-validation approach taken here for spatial prediction.

After cross-validating the variogram successfully, we can say that prediction based on the fitted variogram is approximately unbiased and that the mean-squared prediction error is acceptable. Its role is one of model checking, to prevent blunder and to highlight potentially troublesome prediction points. It cannot prove that the fitted model is correct, merely that is not grossly incorrect.

#### 2.4.5. Kriging

The final stage of a classical geostatistical analysis is to predict the values of  $Y(\cdot)$  at desired locations, perhaps even at all points, in  $D$ . Methods dedicated to this purpose are called kriging, after the South African mining engineer D. G. Krige, who was the first to develop and apply them. Krige's original method, now called ordinary kriging, was based on the special case of model (3.2) in which the mean is assumed to be constant.

Consider the problem of estimating the value of a continuous attribute  $z$  at any unsampled site  $\mathbf{s}$  using only observed  $z$ -data available over the study area  $D$ . Kriging is a generic adopted by geostatisticians for a family of generalized least-squares regression algorithms in recognition of the pioneering work of Danie Krige (1951). All kriging estimators are the basic linear regression estimator  $Z^*(\mathbf{s})$  defined as

$$Z^*(\mathbf{s}) - m(\mathbf{s}) = \sum_{i=1}^n \lambda_i(\mathbf{s})[Z(\mathbf{s}_i) - m(\mathbf{s}_i)] \quad (2.6)$$

Where  $\lambda_i(\mathbf{s})$  is the weight assigned to datum  $z(\mathbf{s}_i)$  interpreted as a realization of the RV  $Z(\mathbf{s}_i)$ . The quantities  $m(\mathbf{s})$  and  $m(\mathbf{s}_i)$  are the expected

values of the RVs  $Z(\mathbf{s})$  and  $Z(\mathbf{s}_i)$ . The number of data involved in the estimation as well as their weights may change from one site to another.

The interpretation of the unknown value  $z(\mathbf{s})$  and data value  $z(\mathbf{s}_i)$  as realizations of RV  $Z(\mathbf{s})$  and  $Z(\mathbf{s}_i)$  allows us to define the estimation error as  $Z^*(\mathbf{s}) - Z(\mathbf{s})$ . All flavors of kriging share the same objective of minimizing the estimation or error variance  $\sigma_E^2(\mathbf{s})$  under the constraint of unbiasedness of the estimator,

$$\sigma_E^2(\mathbf{s}) = \text{Var}\{Z^*(\mathbf{s}) - Z(\mathbf{s})\}$$

is minimized under the constraint that

$$E\{Z^*(\mathbf{s}) - Z(\mathbf{s})\} = 0 \quad (2.7)$$

Three kriging can be distinguished according to the model considered for the trend  $m(\mathbf{s})$ :

1) Simple kriging (SK) considers the mean  $m(\mathbf{s})$  to be known and constants throughout the study area  $D$ :

$$m(\mathbf{s}) = m, \text{ known } \mathbf{s} \in D$$

2) Ordinary kriging (OK) accounts for local fluctuations of the mean by limiting the domain of stationarity of the mean to be constant but unknown:

$$m(\mathbf{s}) = \text{constant but unknown}$$

3) Kriging with a trend or universal kriging (UK) considers that the unknown local mean  $m(\mathbf{s})$  smoothly varies within each neighborhood over the entire study area  $D$ . The trend component is modeled as a linear combination of functions  $f_i(\mathbf{s})$  of the coordinates:

$$m(\mathbf{s}) = \sum_{i=0}^n a_i(\mathbf{s})f_i(\mathbf{s})$$

With  $a_i(\mathbf{s})$  constant but unknown

### Simple kriging

The modeling of the trend component  $m(\mathbf{s})$  as known stationary mean  $m$  allows it write the linear estimator 1 as a linear combination of RV  $Z(\mathbf{s}_i)$  and the mean value  $m$ :

$$\begin{aligned} Z_{SK}^*(\mathbf{s}) &= \sum_{i=1}^n \lambda_i(\mathbf{s}) [Z(\mathbf{s}_i) - m] + m \\ &= \sum_{i=1}^n \lambda_i(\mathbf{s}) Z(\mathbf{s}_i) + [1 - \sum_{i=1}^n \lambda_i(\mathbf{s})]m \end{aligned} \quad (2.8)$$

The weights  $\lambda_i(\mathbf{s})$  are then determined such as to minimize the error variance  $\sigma_E^2(\mathbf{s}) = \text{Var}\{Z_{SK}^*(\mathbf{s}) - Z(\mathbf{s})\}$  under the unbiasedness constraint (2.7).

The simple kriging (SK) estimator (2.8) is already unbiased since the error mean is equal to zero:

$$E\{Z_{SK}^*(\mathbf{s}) - Z(\mathbf{s})\} = m - m = 0$$

### Ordinary kriging

The local mean may vary significantly over the study area. Ordinary kriging (OK) accounts for such local variation of the mean by limiting the domain of stationarity of the mean to the local neighborhood centered on the location  $\mathbf{s}$  being estimated. The linear estimator (1) is then a linear combination of the RV  $Z(\mathbf{s}_i)$  plus the constant local mean  $m(\mathbf{u})$

$$Z^*(\mathbf{s}) = \sum_{i=1}^n \lambda_i(\mathbf{s}) Z(\mathbf{s}_i) + [1 - \sum_{i=1}^n \lambda_i(\mathbf{s})]m(\mathbf{s})$$

The unknown local mean  $m(\mathbf{s})$  is filtered from the linear estimator by forcing the kriging weights to sum to 1. The ordinary kriging estimatore  $Z_{OK}^*(\mathbf{s})$  is thus written as a linear combination only of the RV  $Z(\mathbf{s}_i)$ :

$$Z_{OK}^*(\mathbf{s}) = \sum_{i=1}^n \lambda_i(\mathbf{s}) Z(\mathbf{s}_i) \text{ with } \sum_{i=1}^n \lambda_i(\mathbf{s}) = 1 \quad (2.9)$$

Again, the weights  $\lambda_i(\mathbf{s})$  are determined such as to minimize the error variance for the unbiasedness constraint (2.7)

The OK estimator is unbiased since the error mean is equal to zero:

$$E\{Z_{OK}^*(\mathbf{s}) - Z(\mathbf{s})\} = \sum_{i=1}^n \lambda_i(\mathbf{s}) m(\mathbf{s}_i) - m(\mathbf{s}) = m(\mathbf{s}) - m(\mathbf{s}) = 0$$

OK is usually preferred to SK, because it requires neither knowledge nor stationarity of the mean over the entire area  $D$ .

### Universal kriging

The local estimation of the mean in ordinary kriging allows it to account for any trend over the study area  $D$ . Thus, OK implicitly considers a non-stationary random process model, where stationarity is limited within each search neighborhood. In some situations, it may be inappropriate to consider the local mean  $\mu$  as constant within search neighborhoods. Kriging with a trend or universal kriging (UK) consists of modeling the local trend within the neighborhood as a smoothly varying function; recall the function:

$$m(\mathbf{s}) = \sum_{i=0}^n a_i(\mathbf{s}) f_i(\mathbf{s})$$

The functions  $f_i(\mathbf{s})$  are known, whereas the coefficients  $a_i(\mathbf{s})$  are unknown and deemed constant within each local neighborhood. The linear estimator (2.6) is thus written

$$Z^*(\mathbf{s}) = \sum_{i=0}^n a_i(\mathbf{s}) f_i(\mathbf{s}) + \sum_{i=1}^n \lambda_j(\mathbf{s}) [Z(\mathbf{s}_j) - \sum_{i=0}^n a_i(\mathbf{s}) f_i(\mathbf{s}_i)]$$

The unknown coefficients  $a_i(\mathbf{s})$  are filtered from the linear estimator by

imposing the following constraints:

$$\sum_{j=1}^n \lambda_j(\mathbf{s}) f_j(\mathbf{s}_j) = f_i(\mathbf{s}) \quad (2.10)$$

By convention, the first trend function  $f_0(\mathbf{s})$  is the unit constant, that is,  $f_0(\mathbf{s}) = 1$ . Hence the first condition is similar to the OK constraint on the weights:  $\sum_{i=1}^n \lambda_i(\mathbf{s}) = 1$ .

The constraints (2.10) allow it to write the UK estimator as a linear combination of only the RV  $Z(\mathbf{s}_i)$ :

$$Z_{UK}^*(\mathbf{s}) = \sum_{i=1}^n \lambda_i(\mathbf{s}) Z(\mathbf{s}_i) \quad \text{with} \quad \sum_{i=1}^n \lambda_i(\mathbf{s}) f_i(\mathbf{s}_j) = f_i(\mathbf{s})$$

The kriging with trend estimator is also unbiased since the error mean is equal to zero.

Direct measurements of the interested attribute are often supplemented by secondary information originating from other related categorical or continuous attributes. The estimation generally improves when this additional and usually denser information is taken into consideration, particularly when the primary data are sparse or poorly correlated in space.

### **The cokriging methods**

Consider the situation where primary data  $\{z_1(\mathbf{s}_i), i = 1, \dots, n\}$  are supplemented by secondary data related to continuous attributes  $z_j, \{z_j(\mathbf{s}_i), i = 1, \dots, n, j = 2, \dots, N\}$ , at any possibly different sites. The linear estimator (2.6) is extended to incorporate this additional information:

$$Z_1^*(\mathbf{s}) - m_1(\mathbf{s}) = \sum_{i=1}^n \lambda_i(\mathbf{s}) [Z_1(\mathbf{s}_i) - m_1(\mathbf{s}_i)] + \sum_{j=2}^N \sum_{i=1}^n \lambda'_i(\mathbf{s}) [Z_i(\mathbf{s}_i) - m_i(\mathbf{s}_i)] \quad (2.11)$$

Where  $\lambda_i(\mathbf{s})$  is the weight assigned to the primary datum  $Z_1(\mathbf{s}_i)$  and  $\lambda'_i(\mathbf{s})$

is the weight assigned to the secondary datum  $Z_i(\mathbf{s}_i)$ . Typically, only the primary and secondary data closest to the site  $u$  being estimated are retained. The amount of data retained and the size of the search neighborhood need not be the same for all attributes.

All cokriging estimators are variants of expression (2.11). They are all required to be unbiased and to minimize the error variance  $\sigma_E^2(\mathbf{s})$ , that is

$$\sigma_E^2(\mathbf{s}) = \text{Var}\{Z_1^*(\mathbf{s}) - Z_1(\mathbf{s})\}$$

is minimized under the constraint that the expected error is zero:

$$E\{Z_1^*(\mathbf{s}) - Z_1(\mathbf{s})\} = 0$$

Here we describe the more general method of ordinary cokriging. Ordinary cokriging (OCK) allows for local variability of the means by restricting the stationarity of both primary and secondary variables to a local neighborhood centered on the location  $\mathbf{s}$  being estimated. For the case of a single secondary attribute  $z_2$ , the cokriging estimator (2.11) is written

$$Z_1^*(\mathbf{s}) = \sum_{i=1}^n \lambda_i(\mathbf{s})Z_1(\mathbf{s}_i) + \sum_{j=1}^n \lambda'_j(\mathbf{s})Z_2(\mathbf{s}_j) + \lambda_{m1}(\mathbf{s})m_1(\mathbf{s}) + \lambda_{m2}(\mathbf{s})m_2(\mathbf{s})$$

Where primary and secondary means are constant within each search neighborhood. The weights  $\lambda_{m1}(\mathbf{s})$  and  $\lambda_{m2}(\mathbf{s})$  are

$$\lambda_{m1}(\mathbf{s}) = 1 - \sum_{i=1}^n \lambda_i(\mathbf{s}), \quad \lambda_{m2}(\mathbf{s}) = -\sum_{j=1}^n \lambda'_j(\mathbf{s})$$

If the local means  $m_1(\mathbf{s})$  and  $m_2(\mathbf{s})$  are actually unknown, they can be filtered from the linear estimator by setting their respective weight to zero. The ordinary cokriging estimator is then written,

$$Z_{OCK}^1(\mathbf{s}) = \sum_{i=1}^n \lambda_i(\mathbf{s})Z_1(\mathbf{s}_i) + \sum_{j=1}^n \lambda'_j(\mathbf{s})Z_2(\mathbf{s}_j) \quad (2.12)$$

With these two constraints

$$\sum_{i=1}^n \lambda_i(\mathbf{s}) = 1, \quad \sum_{j=1}^n \lambda'_j(\mathbf{s}) = 0$$

The ordinary cokriging estimator (2.12) is unbiased:

$$E\{Z_{oCK}^1(\mathbf{s}) - Z_1(\mathbf{s})\} = \left[ \sum_{i=1}^n \lambda_i(\mathbf{s}) - 1 \right] m_1 + \sum_{j=1}^n \lambda'_j(\mathbf{s}) m_2 = 0$$

## 2.5 Geostatistical process simulation

Recall that the spatial index of the underlying process  $\{Z(\mathbf{s}): \mathbf{s} \in D\}$  varies continuously over  $d$ -dimensional subset  $D$  of  $\mathbb{R}^d$ . Each estimate  $z(\mathbf{s})$  is best in the least-squares sense because the local error variance is minimum. However, such kind of best estimated map may not be best in total situation. Typically, small values are overestimated, while large values are underestimated. Such conditional bias is a shortcoming when trying to detect patterns of extreme values. Another drawback of estimation is that the smoothing is not uniform, it depends on the local data configuration: smoothing is minimal close to the data locations and increase as the location being estimated gets farther away from data locations. A kriging estimate map appears more variable in densely sampled areas than in sparsely sample areas.

If real data are not available, or in order to assess uncertainties, one could always simulate, validating a method on data where the true values of the parameters are known can be an important aspect of setting its benefit. This part is concerned with methods for simulating spatial processes and their extension to conditional simulation.

The general differences between simulation and estimation can be compared in fig. 2.2. Because kriging estimation is based on the average prediction, there is

a smooth effect; while different realizations generated from simulation could give more possibilities.

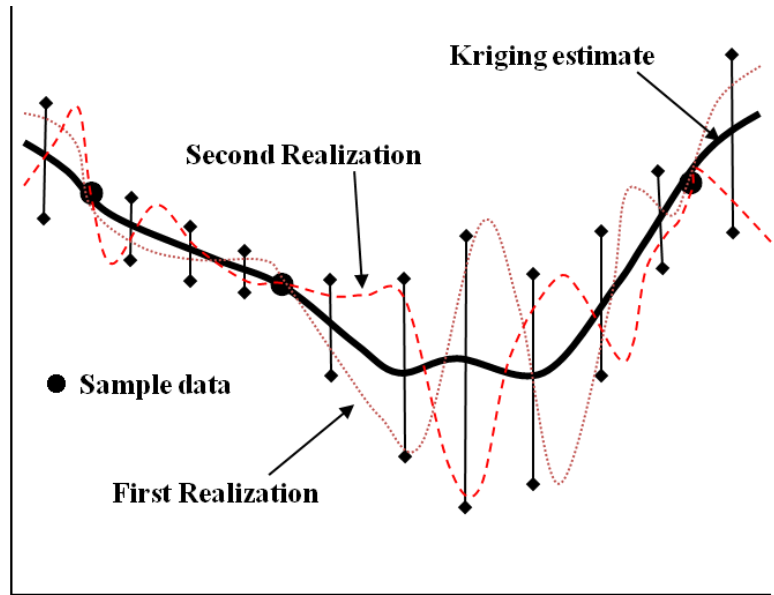


Fig. 2.2 Comparison of simulation and estimation

In actuality, a simulation of the whole process is usually carried out on a discrete grid and then approximated to  $D$ . Usually, spatial simulation methods are most appropriate for Gaussian processes, although it will be seen that sometimes small modifications can lead to more general random processes. The most obvious comes from transforming Gaussian process  $\{Z(\mathbf{s}): \mathbf{s} \in D\}$  to a lognormal process  $\{\exp(Z(\mathbf{s})): \mathbf{s} \in D\}$ . A requirement for simulation of any process is that all parameters of the process must be specified. The source of random variation is usually a pseudo random number generator, and the choice of a good one for spatial simulation needs considerable care.

Here the sequential Gaussian co-simulation is introduced as an example. Consider the situation where primary data  $\{z_1(\mathbf{s}_i), i = 1, \dots, n\}$  are supplemented by secondary data related to different continuous attributes  $\{z_j(\mathbf{s}_i), i = 2, \dots, n\}$

possibly at different locations. The objective is to simulate only the primary variable  $Z_1$  conditional to both primary and secondary information.

The sequential Gaussian simulation of primary variable  $Z_1$  proceeds as follows:

- 1) Define a random path visiting each node of the grid only once.
- 2) At each node, determine the parameters (mean and variance) of the Gaussian cdf using cokriging with the direct and cross semivariogram models of variables.
- 3) Draw a simulated value from that cdf, and add it to the data set.
- 4) Proceed to the next node along the random path, and repeat the two previous steps.
- 5) Loop until all  $N$  nodes are simulated.

Other realizations are obtained by repeating the entire process with a different random path for each realization.

For the conditional simulation mentioned above, it relies on an orthogonal decomposition of the spatial process into the kriging predictor plus the residual process. There is an implicit assumption that the process being simulate is Gaussian, otherwise the conditionally simulated quantity is not the posterior distribution. Therefore, statistical speaking, in order to yield the posterior distribution of the unobserved parts of the spatial process, it is needed to account for the measurement error in the observed parts.

## **2.6 Summary**

In this chapter, the main development of spatial statistics was introduced first. As a branch of spatial statistics, the interpolation methods of geostatistics were

introduced. In order to solve the sparse data problem, the conditional simulation was described to be another modeling method integrated with kriging paradigm. Especially, beyond ordinary kriging, the co-kriging with hard data and soft data was also a main tool to depict the spatial structure of saline water.

## Chapter 3

### Case Site and Fundamental Data Properties

#### 3.1 The HLW disposal situation

Key activities in development of a repository safety or performance assessment are the comprehensive identification of the relevant factors, often termed “features, events and processes” (FEPs), and the selection of factors that should be included in quantitative analyses. The processes of identifying, classifying and screening the factors form the first stages of the identification and selection of alternative futures relevant to assessment of repository performance, which is termed scenario development (NEA, 1992).

The role of the URL projects in Japan is to develop and confirm the relevant technologies that will be applied in a real geological environment. This is achieved by maintaining an awareness of the overall goal accurate understanding of the geological environment – while setting tasks such as data acquisition and evaluation of the applicability of the technologies.

When designing a disposal system and evaluating its safety based on the results of characterization of the geological environment, major challenges include understanding the spatial heterogeneities of the actual geological environment and addressing the uncertainties associated with these

heterogeneities. This involves frequent trial and error and repeated feedback. In general, the depth of understanding will increase in proportion to the extent of investigations.

As described above, the Horonobe URL project involves geoscientific research and R&D on geological disposal technology for sedimentary formations, with three major goals:

- to establish the basis for techniques for characterizing the deep geological environment;
- to develop the basis for engineering technologies for use in the deep underground;
- to confirm the applicability of geological disposal technologies in specific geological environment.

### **3.2 Investigation and background setting**

The investigations in and around the URL area can be divided into three types: investigations using existing information, ground exploration and borehole investigations. The investigations using existing information involve integration and interpretation of information obtained during the investigations covering the whole area of Horonobe Town and identifying issues not addressed in this stage (Fig. 3.1). Based on the results and focusing on determining the spatial distribution of the Omagari Fault and the characteristics of the geological environment and acquiring geological information for the URL site, the latter two types of investigation were conducted.

The investigations of geology and geological structures were carried out to

acquire the information necessary for hydrogeological, hydrochemical and rock mechanical characterization and to establish relevant investigation techniques. The areas covered included topography, geological heterogeneity, thickness of the overburden (unconsolidated deposits) and features that are important such as solute transport pathways.

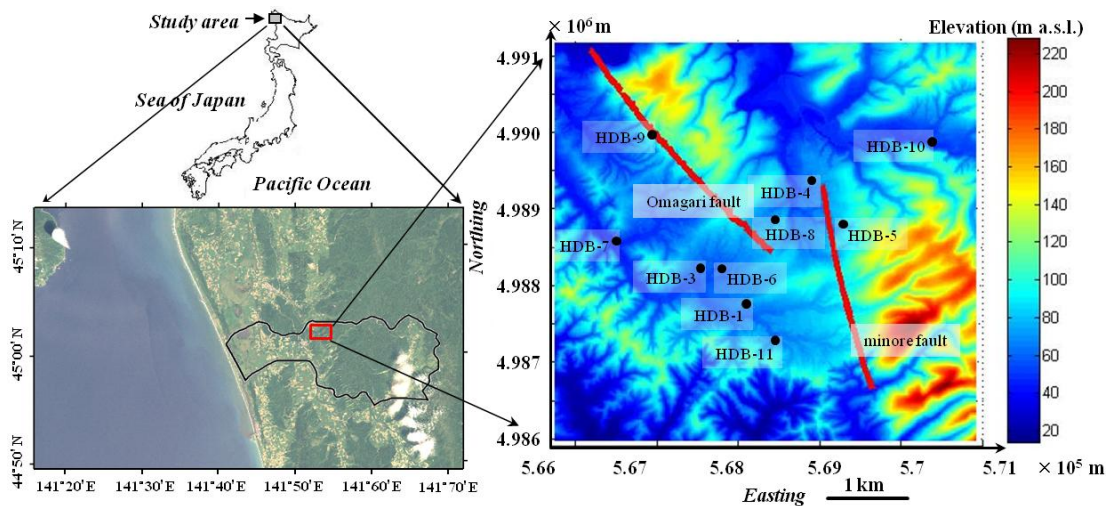


Fig. 3.1 Research area and boreholes location with main fault.

### 3.2.1 Surface-based investigations in Horonobe area

The main aims of the investigations during this stage were to clarify the topography, geological heterogeneity, thickness of the overburden and features important for solute transport for the whole area of Horonobe Town. The information obtained represents an important basis for understanding the area of interest and will provide input for hydrogeological and hydrochemical modeling.

The investigations conducted include:

- reconnaissance surveys to clarify geological heterogeneity (Higashinaka *et al.*, 2002);

- topographical surveys to examine terrace facies and reconnaissance surveys to determine the thickness of the overburden (Yasue *et al.*, 2004);
- topographical surveys (lineament investigations) (Saga, 2004, 2005), reconnaissance surveys (Ishii *et al.*, 2006), AMT electromagnetic surveys (Ishii *et al.*, 2006), ground-penetrating radar surveys (Yasue *et al.*, 2006), reflection seismic surveys (Ishii *et al.*, 2006; Higashinaka *et al.*, 2002), re-analysis of data from previous reflection seismic surveys (Higashinaka *et al.*, 2005) and gravity surveys (Higashinaka *et al.*, 2004; Tsukuwi *et al.*, 2007) to clarify structures potentially important as solute transport pathways.

### **Topography**

The Soya Hill, located in the northern region of Hokkaido, is divided into west, central and east parts by the Omagari and Horonobe Faults, the two major structural features that run north to south (Nagao, 1960; Koaze *et al.*, 2003). The URL area selected for this investigation phase is located near the boundary between the west and central parts. The west part is dominated by the Teshio Plain consisting of the Sarobetsu Lowland and the Ubushi Lowland, with hills at 80–190 m elevation, stretching in an N-S direction. The central part is located between the Omagari Fault and the Horonobe Fault and has hilly terrain with altitudes of 100–300 m elevation (Yasue *et al.*, 2005; Niizato *et al.*, 2005). The E-W extent gradually narrows towards the south.

### **Geological heterogeneity**

Horonobe Town is located at the eastern edge of the Tenpoku sedimentary drainage basin, where the Palaeogene Haboro and Magaribuchi Formations, the Soya Coal-bearing, Onishibetsu and Masuporo Formations (Early–Middle Miocene), the Wakkanai and Koetoi Formations (Late–Middle Miocene to Pliocene), the Yuchi and Sarabetsu Formations (Pliocene to Early Pleistocene), terrace sediments later than the Middle Pleistocene and Holocene sediments are distributed on Cretaceous bedrock (Oka and Igarashi, 1997). Of these formations, the Haboro and Magaribuchi Formations were not identified from the ground surface but were observed in deep borehole investigations. The Wakkanai, Koetoi, Yuchi and Sarabetsu Formations consist of a series of sediments made up of abyssal, shallow marine, semi-terrestrial and terrestrial deposits that unconformably overlie the Masuporo Formation (Oka and Igarashi, 1997; Takahashi *et al.*, 1984; Fukusawa, 1983). The Wakkanai and Koetoi Formations consist of siliceous rocks, while the Yuchi and Sarabetsu Formations consist of coarse-grained clastic material. The stratigraphy is based primarily on the classification of lithofacies. It should be pointed out that the boundaries of the formations do not necessarily coincide with the boundaries of geological eras (Takahashi *et al.*, 1984); there are heteropic facies between the Koetoi Formation and the Yuchi Formation and between the Yuchi Formation and Sarabetsu Formation (Oka and Igarashi, 1997; Fukusawa, 1983). In the following paragraphs, a general description for the formations distributed in and around the URL area is given (Fig. 3.2); the Masuporo, Yuchi and Sarabetsu Formations are discussed first, followed by the Wakkanai and Koetoi Formations, the latter being the main formations to be characterized.

Table 3.1 Geological stratigraphy in research area

		Formation	Lithology	Thickness (m)	Silica diagenesis	
Quaternary	Holocene	Alluvium	Sand, mud, gravel	0~85	Opal-A zone	
	Pleistocene	Late	Terrace deposits	5~50		
		Middle	Sarabetsu	Alternating beds of conglomerate, sandstone and mudstone with coal seams		650~900
Neogene	Pliocene	Early	Yuchi	Fine to medium grained sandstone	100~1000	
		Late	Koetoi	Massive diatomaceous mudstone including opal-A	300~1000	
	Miocene	Late	Wakkanai	Massive siliceous mudstone including opal-CT	200~1000	Opal-CT zone
		Early				
		Middle				

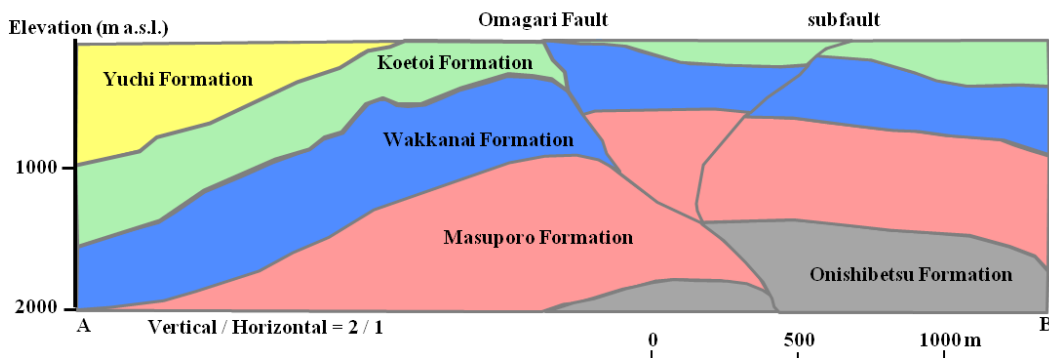
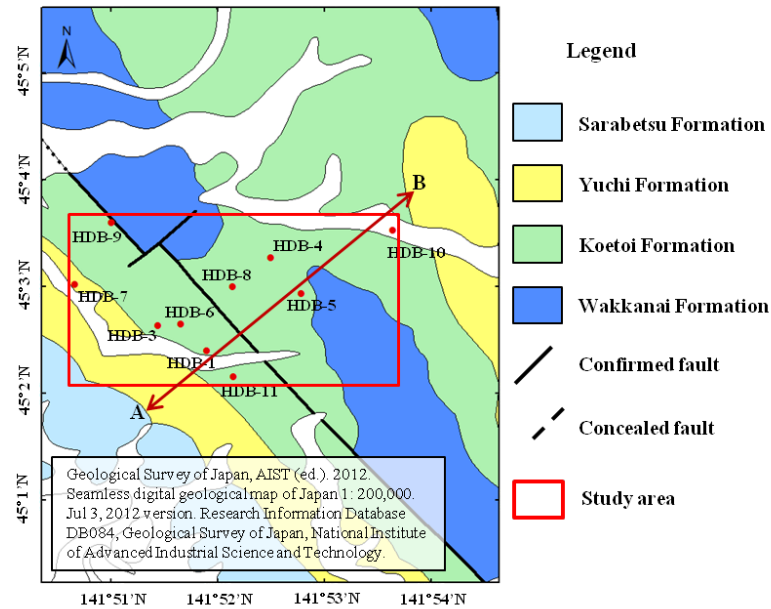


Fig. 3.2 Geologic map of study area and cross-section along A–B, showing general geological structure, after the Geological Survey of Japan, AIST (2012).

The Masuporo Formation consists of alternating layers of conglomerates, sandstones and mudstones, often intercalated with slumping beds. The thickness of the formation varies between around 900 m and 1000 m.

There are diverging opinions on the definition of the Wakkanai and Koetoi Formations. Focusing on lithology, Nagao (1960) and Mitani *et al.* (1971) classified the formation consisting primarily of so-called “hard shale” (siliceous shale or siliceous mudstone – both are mudstones consisting of silica minerals with low crystallinity, i.e. opal CT) as the Wakkanai Formation and the formation above this, consisting primarily of diatomaceous mudstones (mudstones consisting of non-crystallised amorphous silica minerals, i.e. opal A), as the Koetoi Formation. On the other hand, Fukusawa (1985) focussed on the sedimentary structure and reclassified the formation consisting of siliceous or diatomaceous shale with clear bedding as the Wakkanai Formation and the formation above this, consisting of siliceous mudstones or diatomaceous mudstones with no clear bedding, as the Koetoi Formation. The latter also demonstrated by lithological examination that the diatomaceous shale had been hardened to form siliceous shale in the Wakkanai Formation and the diatomaceous mudstone to siliceous mudstone in the Koetoi Formation through progressive burial diagenesis of siliceous minerals. Although there are differing views on the definition of the Wakkanai and Koetoi Formations, the definition of Nagao (1960) and Mitani *et al.* (1971) was adopted for the Horonobe URL project, because only geological maps based on the definition of Nagao and Mitani *et al.* are widely available. These studies were a basis for regional groundwater flow analysis that

was needed at the initial stage of the investigation. In short, the Wakkanai Formation consists primarily of siliceous mudstones with no clear bedding or siliceous shale with clear bedding; the upper part of the formation is a transition zone to diatomaceous mudstones. The thickness of the formation varies between around 600 m and 1000 m and the lower boundary age is estimated to be 13 Ma based on the radiometric age of volcanoclastic rocks (Fukusawa, 1985) formed at the base of the siliceous shale. The Koetoi Formation consists primarily of diatomaceous mudstone that appears massive on first inspection and gradually changes in an upward direction to sandy mudstone. The thickness of the formation varies between around 400 m and 700 m.

The Yuchi Formation consists of soft fine-grained sandstone. The thickness of the formation varies between around 400 m and 800 m.

The Sarabetsu Formation consists of alternating layers of conglomerate, sandstone and siltstone, intercalated with a lignite seam. The maximum thickness of the formation is about 700 m and the age is presumed from shell and pollen fossils to be about 1.3–0.7 Ma (Oka and Igarashi, 1997).

In the central part of Horonobe Town, the features known as the Horonobe Fault (N1–N5 faults) and the Omagari Fault, which are large enough to be shown on the geological map, run parallel in an NNW-SSE direction. These faults may be important as solute transport pathways.

The Horonobe Fault consists of several individual faults (N1–N5 faults) with a strike of NNW-SSE and right-echeloning with a step width of about 1 km. Although fault traces can be identified as a lineament in the topography, no change in the topography in the Late Pleistocene is observed.

The Omagari Fault extends more than 25 km (Nagao, 1960) in length and connects to the Tono Fault in the south (Hirooka, 1962; Fukusawa, 1987). The location of the fault at the surface is assumed to be primarily at the boundary between the Wakkanai Formation in the east and the Koetoi Formation in the west (Mitani *et al.*, 1971). On the east side of the fault, a fold structure with an axis in the direction N20–15 °W is aligned en echelon (Hirooka, 1962; Masaya *et al.*, 1982). The fault was interpreted as being a normal fault tilted to the west since the fault plane inclines westward at the ground surface and the east side of the fault uplifts (Nagao, 1960; Nagao and Makino, 1959). However, on the basis of a later geophysical survey, the fault was interpreted as being a reverse fault with uplift on the east side (Mitani *et al.*, 1971; Yamamoto, 1979; Ogura and Kamon, 1992). Oka (1986) also interprets this fault as a reverse fault.

The Omagari Fault was observed in outcrop 5 km south of the URL area. At this location, a fault plane about 10–20 cm wide containing fault breccia was observed, forming the boundary between the Wakkanai Formation and the Koetoi Formation, as well as a cluster of minor faults containing fault breccia about 1–10 cm wide or fault gouges 0.5–3.0 cm wide, which were dominant in the range of about 120 m from the above fault plane (Fig. 3.3). This indicates that the Omagari Fault consists of a 10–20 cm wide fault nucleus and a damaged zone about 120 m wide (Ishii *et al.*, 2006). From the topographical surveys (lineament surveys) performed near the fault outcrop, small lineaments were traced on the extension of the strike direction of the fault (NNW-SSE direction) that would indicate the existence of the fault (Yasue and Ishii, 2005). Some information on the location of the fault had already been obtained from the geophysical surveys. In addition, a

structure concordant with the strike direction of the fault that could be related to the fault was observed by the ground-penetrating radar surveys near the fault outcrop (Yasue *et al.*, 2006). More detailed on location, orientation, and fracturing pattern of the fault were determined by borehole televiewer survey, resistivity logging, and drilling core study including microfracture analysis (Ishii *et al.*, 2006; Ishii, 2012). General orientation of the unfolded major faults in boreholes related to the fault is N50 °W in strike with nearly vertical dips, whereas orientation of unfolded subfaults varies in the boreholes. Table 3.1 shows the orientations of bedding planes and faults, in boreholes. The major fault orientations in HDB-6, HDB-9, and HDB-11 are similar, and have lower dip angles than those in HDB-5. The major fault orientations in HDB-10 differ significantly from those within the other boreholes.

Table 3.2 Orientations (dip direction/dip) of bedding planes and faults in boreholes

Borehole	Bedding plane	Fault		Fault (unfolded)	
		Major	Minor	Major	Minor
HDB-5	265/35	015/65		29/81	
HDB-6	225/35	010/53		17/83	
HDB-9	230/40	030/50	170/57	35/88	138/47
HDB-10	055/40	217/57	160/50	37/85	180/68
HDB-11	230/40	005/55	280/45	15/86	331/34

### 3.2.2 Borehole investigations

Deep borehole investigations (boreholes HDB-1 to HDB-11, Fig. 3.4) were conducted to clarify the geological heterogeneity of the rock formations and shallow borehole investigations (Takahata *et al.*, 2004; Watanabe, 2004) were

used to determine the thickness of the overburden (unconsolidated deposits). The deep borehole investigations, as well as gas investigations (Matsui *et al.*, 2006; JNC, 2005) in the shallow boreholes, were also aimed at clarifying features that could be important as solute transport pathways. The gas investigations involved measurement of the concentrations of CH<sub>4</sub> and CO<sub>2</sub> immediately above the groundwater surface in the boreholes (maximum depth of 30 m). The boreholes for the measurements were aligned so as to cross the strikes of the faults at right angles to better determine the influence of the Omagari Fault.

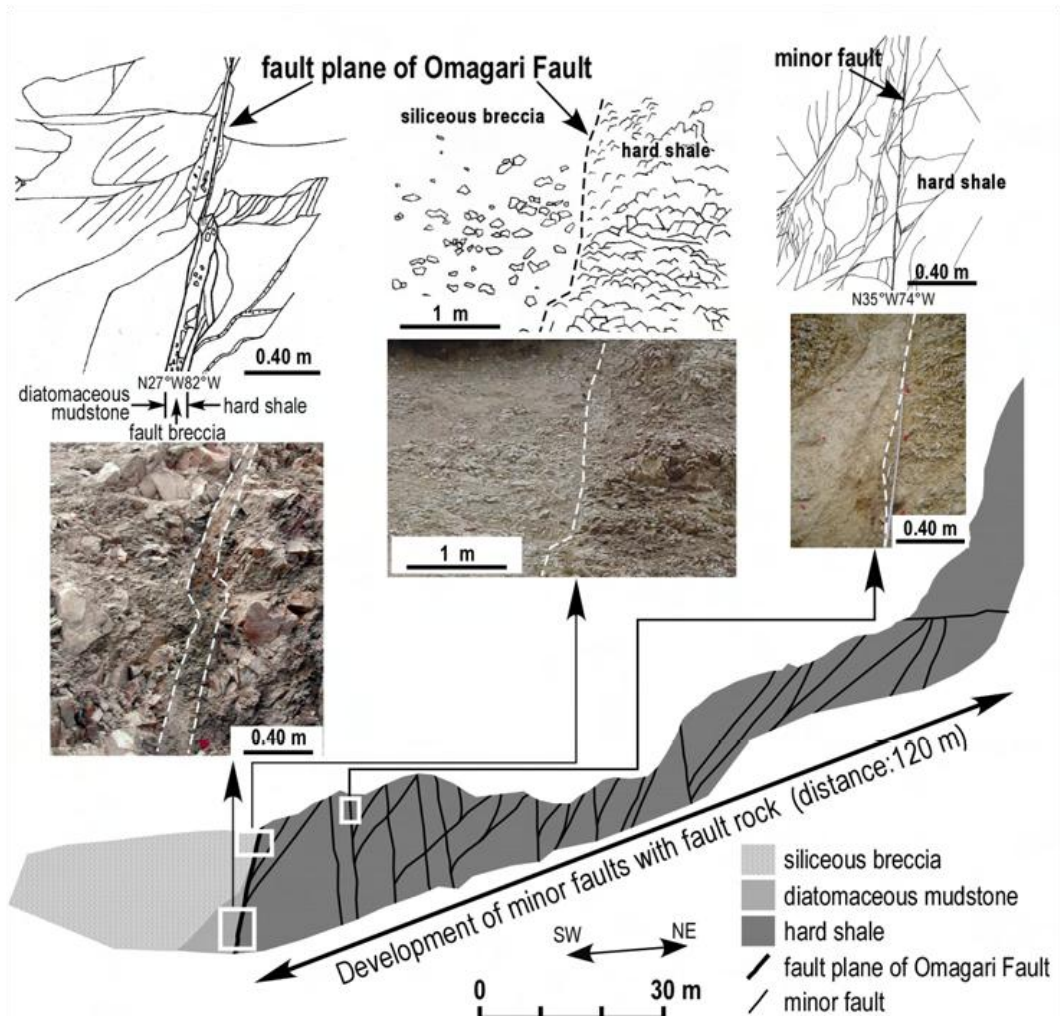


Fig. 3.3 Sketches at the fault outcrop of the Omagari Fault. In the boreholes HDB-4 and HDB-5, there were numerous fractures and circulation loss sections during drilling,

suggesting that these fractures may be important as solute transport pathways.

Examining the results of the deep borehole investigations (core logging, borehole wall image analysis), most of the fractures observed in the boreholes were judged to be shear fractures, based on the intercalation of fault rocks and the presence of striations and slickensides on the surface of the fractures (JAEA, 2010). The fractures can be divided into either minor faults at a high angle to the bedding plane or those parallel to the bedding plane. In addition, since the former minor faults tend to gather densely, the clustered zone was defined as a fracture or fault zone (Ishii and Yasue, 2005). The sections where drilling fluid was lost during drilling and also where the hydraulic conductivity was high during in situ hydraulic tests corresponded to a fault zone.

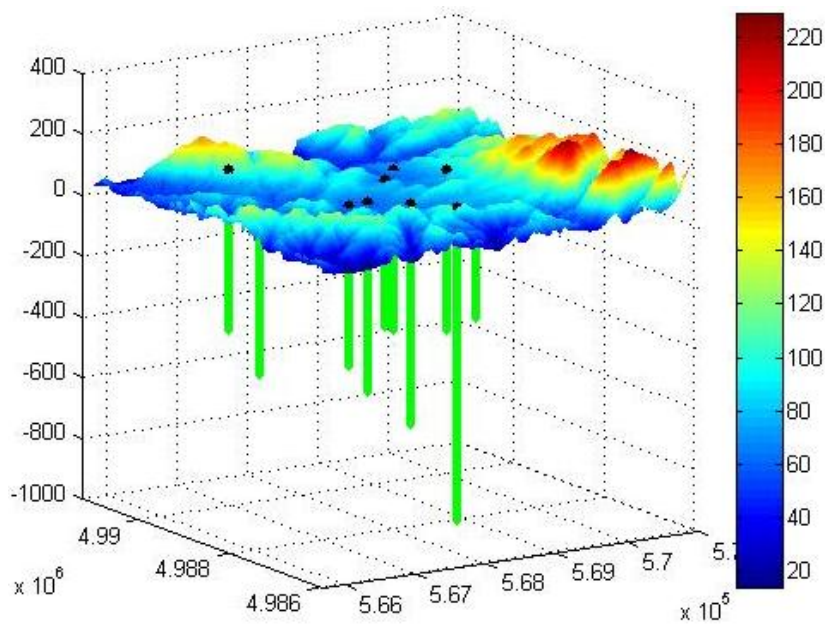


Fig. 3.4 Plot of topography and boreholes in Horonobe URL

### 3.3 Geological modeling

Since the Omagari fault is located in and around Horonobe URL and surface investigation suggested that damage zone of Omagari fault could be solute transport pathways, it is worth noting that geological structure of formations, Omagari fault and its minor fault is important for depicting relationship of groundwater spatial distribution and groundwater flow evolution.

A conceptual model of the geological structure in and around the URL area was built by Ishii and Fukushima (2006) shown in Fig. 3.5.

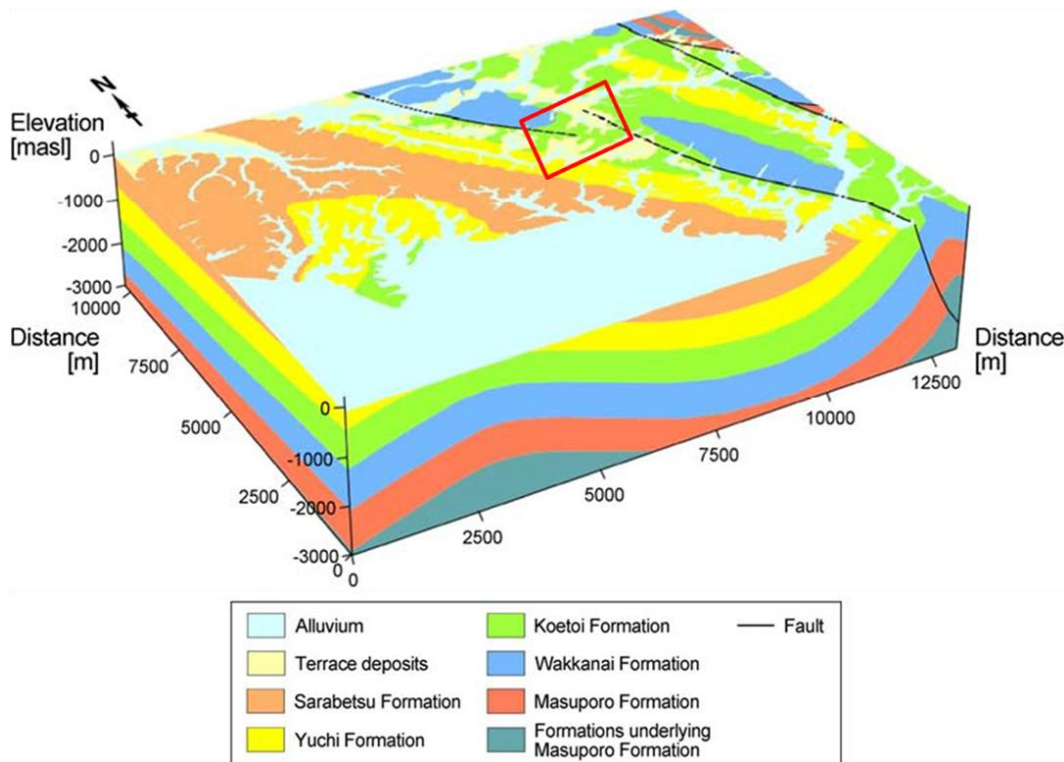


Fig. 3.5 Conceptual model of geological structure and formations in Horonobe.

Distributed in the area are the Wakkanai Formation consisting of siliceous mudstones (or siliceous shale), the Koetoi Formation consisting of diatomaceous mudstones and the Yuchi Formation consisting of sandstones. Discontinuities present in the rocks include the large-scale Omagari Fault and minor faults at a

high angle to the bedding plane where dip-slip prevails and almost parallel to the bedding plane where strike-slip prevails, associated with the fold structure (minor faults that are almost parallel to the bedding plane tend to develop in the limb rather than axis of the fold). Minor faults at a high angle to the bedding plane tend to form fault zones by distributing densely together en echelon; these features, in particular the fault zones, are likely to function as preferential pathways for groundwater.

Moreover, a conceptual model of Omagari fault was built to show distribution of minor fault and damage zone in Fig. 3.6.

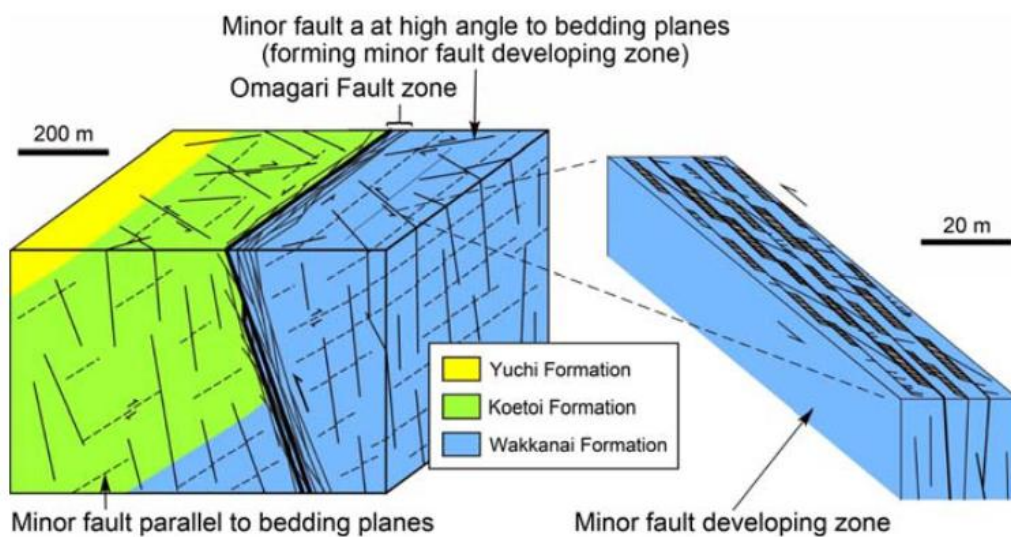


Fig. 3.6 Conceptual model of faults in and around the URL area Modified from Ishii and Fukushima

Discrete points were extracted from these geological model for analysis of relationship between saline water and geological structure in 3D (Fig. 3.7).

We reconstructed a 3D geological model using point data of these planes for comparison with the hydrochemical properties. The resultant model clearly

delineates the structures of the Yuchi, Koetoi, and Wakkanai formations and the faults (Fig. 3.8).

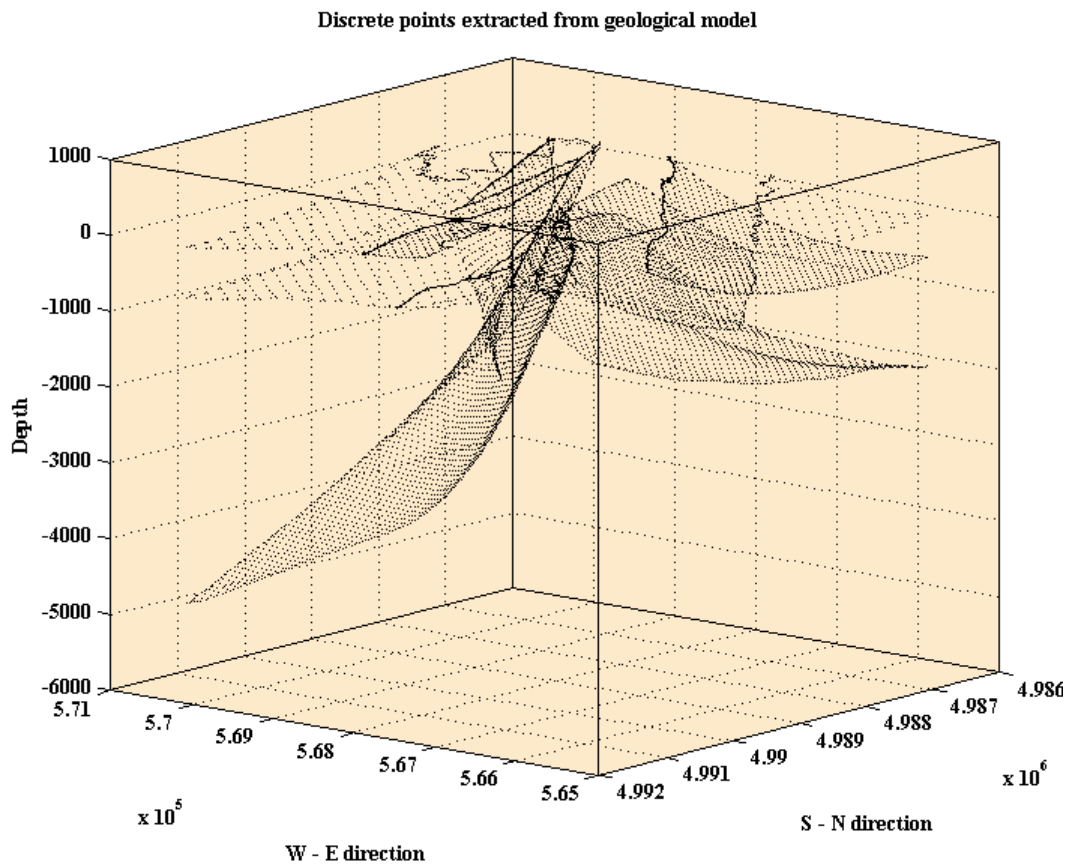


Fig. 3.7 Discrete points extracted from 3D geological models.

### 3.4 Data sampling and analyses

Because saline groundwater was detected by the borehole investigations during petroleum and natural gas exploration (Fujioka and Saga, 1980), an abundant distribution of saline groundwater was estimated around HURL. Eleven deep vertical boreholes from 470- to 1020-m deep were drilled by the Japan Atomic Energy Agency (JAEA) for fundamental investigations of geologic structure, groundwater quality and its relation to formations, and groundwater flow path

(Ota *et al.*, 2011). These boreholes were labeled HDB-1 through HDB-11. Well log tests of resistivity, rock density, porosity, and temperature were also conducted, using boreholes chiefly in the Wakkanai and Koetoi formations. Except for data

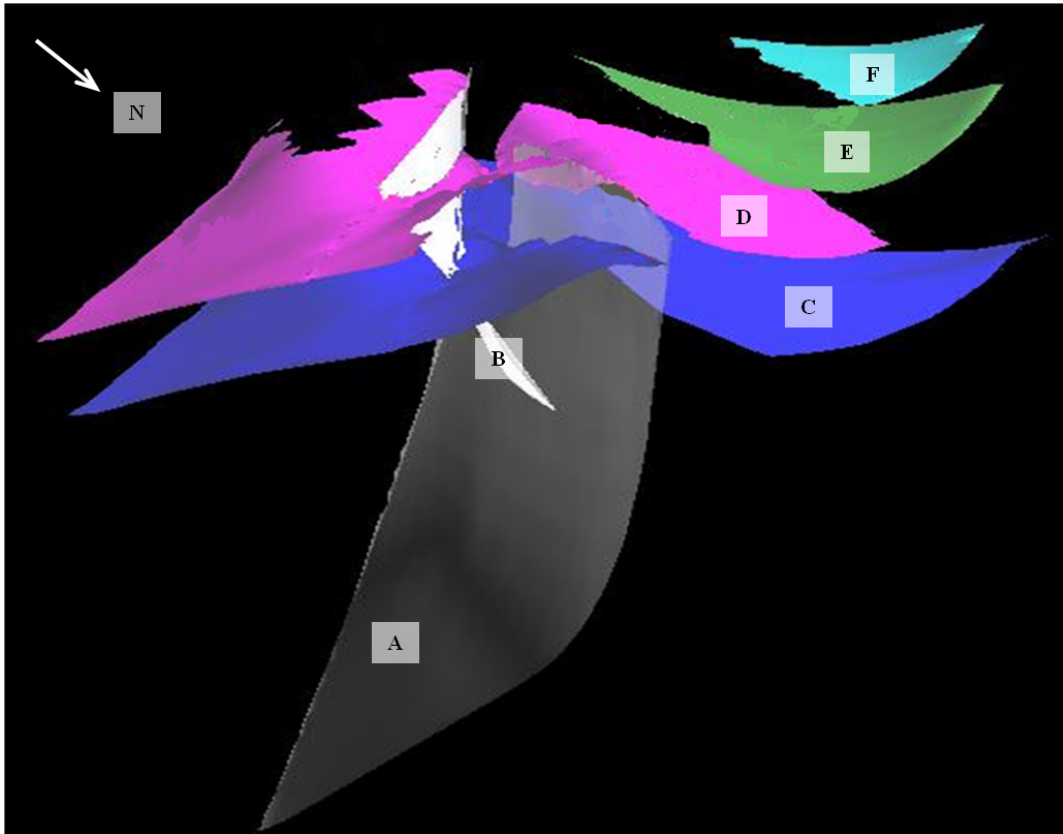


Fig. 3.8 3D geologic model showing formation boundaries (top and bottom planes) and plane shapes of Omagari Fault and subfault, along with distribution of boreholes (red lines). Letter designators are as follows. A: Omagari Fault, B: subfault, C: western part of boundary between Wakkanai and Masuporo formations, D: western part of boundary between Koetoi and Wakkanai formations, E: boundary between Yuchi and Koetoi formations, and F: boundary between Sarabetsu and Yuchi formations.

from borehole (HDB-2) drilled in the early selection stage of the HURL site and located far from HURL (5 km southwestward), geological columns, groundwater chemical data, and well log data at the 10 sites (Fig. 4.2) were used in this study. The well log data are more detailed than water chemical data in terms of data interval along the borehole, which are 0.1 m versus ~50 m, respectively. The

horizontal minimum distance between adjacent borehole sites was 262 m.

Groundwater was sampled in combination with hydraulic packer tests in deep boreholes HDB-1 drilled in the URL site selection stage. Since the hydraulic conductivities of the sedimentary formation were low over the entire length of the boreholes, the groundwater was sampled from a section with relatively high hydraulic conductivity (approximately  $10^{-10}$ – $10^{-9}$  m/s).

Groundwater chemistry was analyzed using pore water squeezed from core samples under uniaxial high pressure of 500 MPa (Kiho *et al.*, 1999).

As significantly high  $\text{SO}_4^{2-}$  concentrations were observed in the pore water from boreholes HDB-1. This was considered to be due to oxidation of sulphides in the cores, as the squeezing operation occurred a few weeks after the cores were sampled. In order to avoid the chemical disturbance caused by oxidation, soon after the cores were obtained, a photograph was taken and geological observations were made immediately after sampling. The cores were then waxed for storage and transport and pore water was finally squeezed in the laboratory

Since the quantity of the squeezed pore water was limited, i.e. a few to a few tens of milliliters, an analysis was conducted for only major ion compositions ( $\text{Na}^+$ ,  $\text{K}^+$ ,  $\text{Ca}^{2+}$ ,  $\text{Mg}^{2+}$ ,  $\text{Cl}^-$ ,  $\text{SO}_4^{2-}$ , and  $\text{HCO}_3^-$ ), stable hydrogen and oxygen isotopes ( $\delta\text{D}$  and  $\delta^{18}\text{O}$ ), and salinity were measured because of the small volume of squeezed water.

For the deep aqueous fluids in sedimentary basins, various descriptive terms have been used in the literature by different criteria. Based on the references from Hanor (1987), Kharaka and Thordsen (1992), White *et al.* (1963), and Sheppard (1986), the following terminology has been used in this study. *Salinity*:

Synonymous with total dissolved solids (TDS), generally reported in milligrams per liter (mg/l) as determined directly by summing measured dissolved constituents, or indirectly from electrical conductivity or spontaneous potential response. *Chlorinity*: The dissolved chloride concentration, generally reported in mg/l. *Brine*: Water of salinity higher than that of average seawater, that is, more than  $3.5 \times 10^4$  mg/l TDS. *Saline water*: Water of salinity  $(1-3.5) \times 10^4$  mg/l. *Brackish water*: Water of salinity  $(0.1-1) \times 10^4$  mg/l. *Freshwater*: Water of salinity less than 1,000 mg/l. *Meteoric water*: Water derived from rain, snow, streams, and other bodies of surface water that percolates in rocks and displaces interstitial water that may have been connate, meteoric, or of any other origin. *Connate water*: The word connate was introduced by Lane (1908) to describe what he presumed to be seawater of unaltered chemical composition trapped in the pore spaces of a Proterozoic pillow basalt since the time of extrusion onto the seafloor. The term has since taken on a variety of meanings. While some authors prefer to use connate in its original sense (e.g., Hanor, 1987), others have used it to refer to waters that have been modified chemically and isotopically, but have been out of contact with the atmosphere since their deposition, although they need not be present in the rocks with which they were deposited (e.g., White *et al.*, 1963; Kharaka and Thordsen, 1992).

To supplement the data from pore water, chemical data from pumped water, which were obtained after adequately removing drilling fluids to exclude contamination, were included in the analyses. The degree of contamination was determined by monitoring pH, Eh, and EC in returned water during the pumping up (Hama *et al.*, 2007). In total 123 pore-water and 22 pumped-water samples

were taken at the 10 borehole sites.

Hydraulic tests were conducted at all boreholes to measure hydraulic conductivities by the Cooper and Hvorslev methods, which used either pulse withdrawal (PW), slug withdrawal (SW), or pressure recovery after slug withdrawal during shut-in (SWS) (Yamamoto et al., 2002). The total number of test intervals was 66, and ranged from 9 to 142 m.

Because  $\text{Cl}^-$  concentration is a critical factor for classifying groundwater quality by salinity, it was selected for the following variography and spatial modeling. To reduce bias of the original  $\text{Cl}^-$  concentration and following resistivity data, the data were transformed into logarithms. The log-transformed data were approximated by a lognormal distribution and used for variography and kriging calculation (Fig. 3.9).

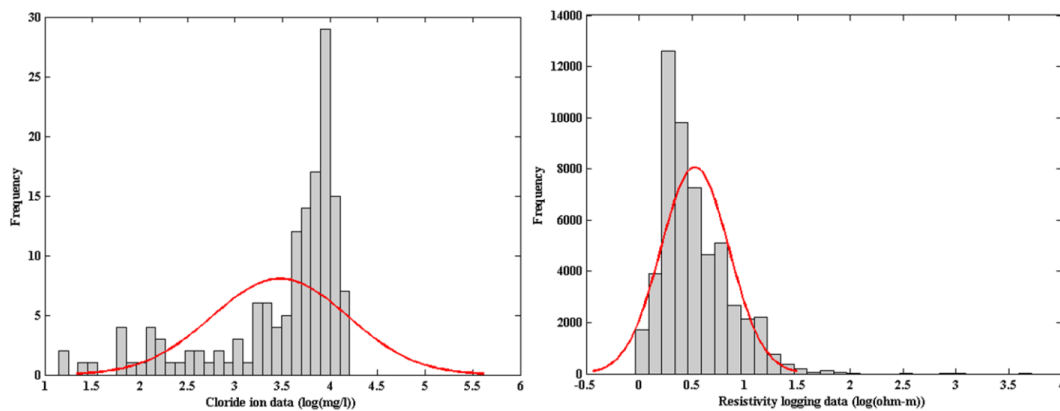


Fig. 3.9 Distribution of log-transformed values

### 3.5 Summary

The site background in Horonobe underground research laboratory was

introduced in this chapter from topography, geological heterogeneity, and boreholes investigations. Because three-dimension geological structure is indispensable in this work, the concept model of geology is introduced, especially, based on this geology concept model, a discrete points 3D geological structure of each formations, the main Omagari fault and its subfault were built for the following research.

The sampling data of saline water generally were very limited, even be added with pumped water data, there were only 145 data could be used in the whole modeling work. Moreover, the data spatial distribution is also different, there were more data distributed in vertical than horizontal direction. Those data were transformed by log-transformation for the geostatistical estimation and simulation. As so far, the data preparation was finished.

### Spatial Characterization of Groundwater Chemistry

#### 4.1 General characteristics of groundwater chemistry

To detect a general trend of major ion concentrations, hexadiagrams were drawn along a cross-section, onto which the 10 geological columns were projected (Fig. 4.1). The hexadiagrams are clearly classified into two types along the depth direction, freshwater of Na-HCO<sub>3</sub> type and saline water of Na-Cl type in the shallow and deep parts, respectively. This was common for all boreholes.

However, it was found that, boundary depths were variable in location within the range -50 m a.s.l. at HDB-3 to -250 m a.s.l. at HDB-4 and HDB-5. Furthermore, as seen at HDB-3 and HDB-1, the boundary depths varied even in the same strata. In this case, depths were -50 m a.s.l. at HDB-3 and -160 m a.s.l. at HDB-1 in the Koetoi Formation. A possible cause of this difference is spatial variation in permeability of sedimentary rocks.

To clarify the permeability variation, hydraulic conductivity data from the above tests were plotted versus depth and formation (Fig. 4.2). Overall, the data are widely dispersed, by a factor of 10<sup>7</sup>, and values near the same depth greatly vary even from the same formation. Correlation of conductivity with depth was weak. Among the three formations, Wakkanai had the greatest variation in hydraulic conductivity because of the mixture of intact parts, shown in the figure by red bars and fault damage zones by gray bars. The Koetoi and Yuchi

formations have variations by factors of 10 and 100, respectively. Intact parts in the Wakkanai Formation were the least permeable, with hydraulic conductivity less than  $10^{-8}$  m/s. This feature may be attributable to the formation's main constituent, siliceous mudstone. Permeability of the Yuchi Formation was similar to that of the intact parts of Wakkanai Formation, except for the deepest part around 700-m depth. In general, hydraulic conductivity of the Koetoi Formation, from  $10^{-9}$  to  $5.25 \times 10^{-7}$  m/s, was greater than that of the Yuchi Formation. Although damage zones of the Wakkanai Formation also had a wide range of hydraulic conductivity, a part of the zones was confirmed to form a highly permeable regime over 150–400 m depths. Another notable feature is that their hydraulic conductivity values were correlated with depth only roughly; the values tended to decline with depth because of a decrease in porosity by overburden proportional to depth.

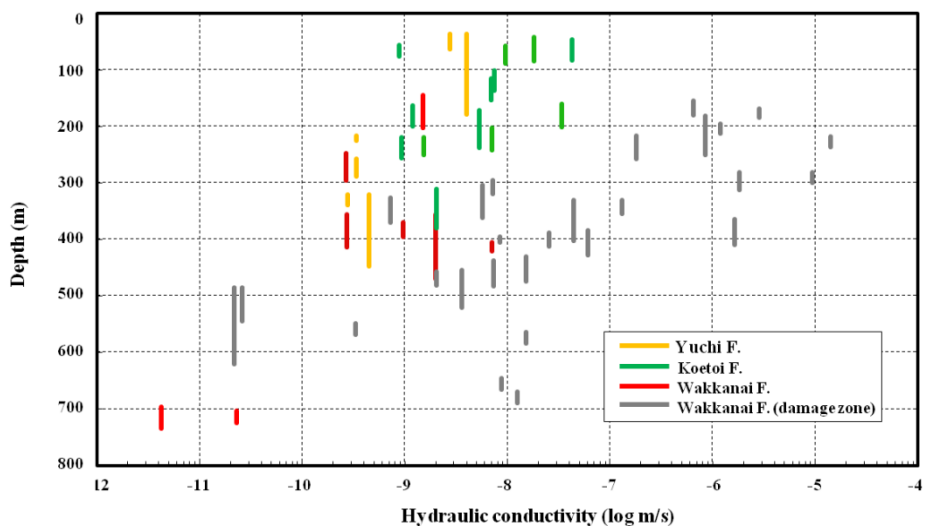


Fig. 4.1 Plots of hydraulic conductivity from well tests in Yuchi, Koetoi, and Wakkanai formations and damage zones. Bars depict test intervals.

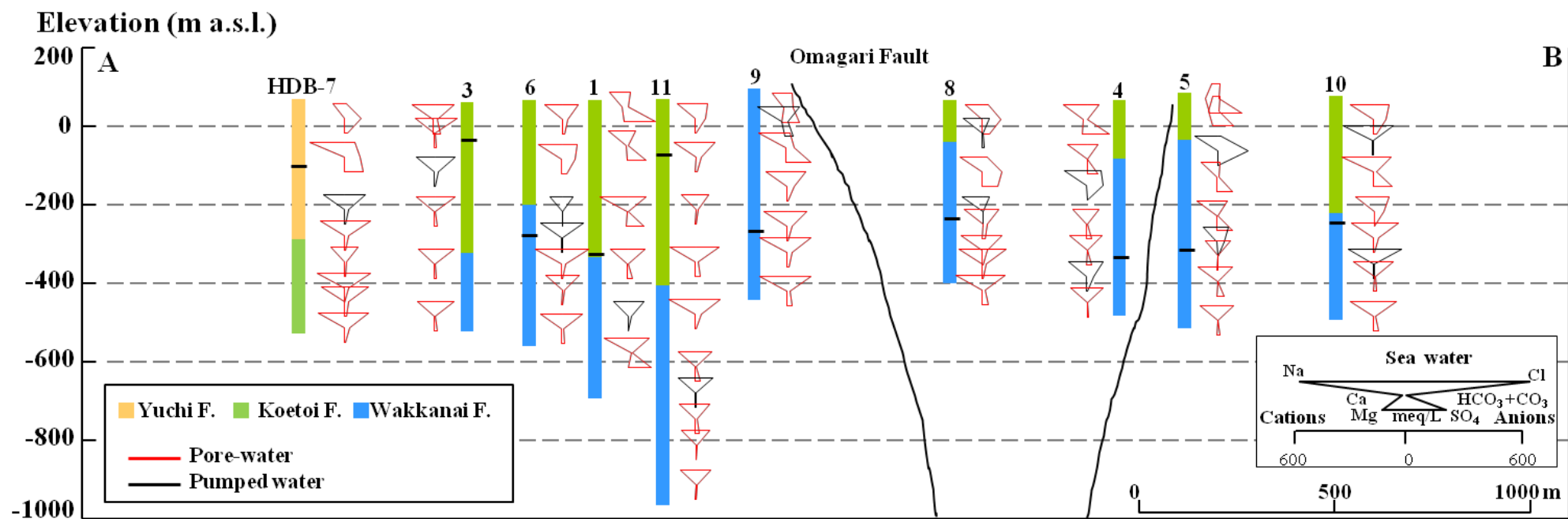


Fig. 4.2 Stiff diagrams of groundwater samples in each borehole and geological columns, which are projected on the A–B cross-section in Fig. 3.2.

## 4.2 3D distribution of chloride ion concentration

Because  $\text{Cl}^-$  concentration is a critical factor for classifying groundwater quality by salinity, it was selected for the following variography and spatial modeling. To reduce bias of the original  $\text{Cl}^-$  concentration and following resistivity data, the data were transformed into logarithms. The log-transformed data were approximated by a lognormal distribution and used for variography and kriging calculation.

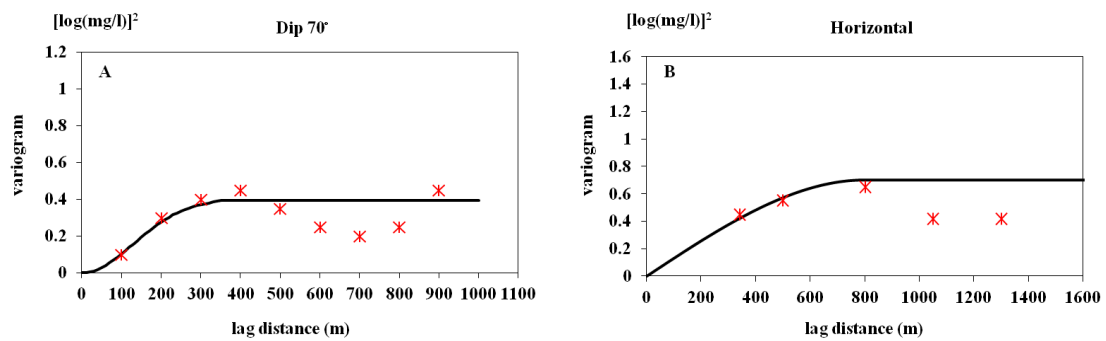


Fig. 4.3 Comparison of omnidirectional experimental semivariograms of  $\text{Cl}^-$  concentration along dip direction of Omagari Fault, the main fault in the study area (A), and along the horizontal direction (B).

Obviously from the geological cross-section in Fig. 3.2, the Omagari Fault is a significant element that displaces all the formations, and probably affects the physical properties of rocks and spatial trend of groundwater chemistry. Although the dip of Omagari Fault is widely variable in the boreholes from  $45^\circ$  to around  $90^\circ$ , and this variability is nearly the same as the subfault (Ishii *et al.*, 2006; Ishii, 2012), their average dip is  $70^\circ$  from the geological model in Fig. 3.4. Therefore, dip angle  $70^\circ$  was considered in the variography. Two omnidirectional  $\gamma_Z^*(\mathbf{h})$  of  $\text{Cl}^-$  concentration along the horizontal and  $70^\circ$  dip directions are compared in Fig. 4.3. Effectiveness of considering the dip is proven by this comparison, because the spatial correlation of  $\text{Cl}^-$  concentration is more clearly extracted by  $\gamma_Z^*(\mathbf{h})$  along

the dip, which increases more smoothly and substantially with separation distance  $\mathbf{h}$ .  $\gamma_Z^*(\mathbf{h})$  along the  $70^\circ$  dip can be approximated well by the Gaussian model, as shown by the curve in Fig. 4.3. The range (maximum distance over which all data pairs are dependent) and nugget effect (microscale variation that causes discontinuity at the origin) of this model were 320 m and 0.01, respectively. The smallness of the nugget effect and strong fit of  $\gamma_Z^*(\mathbf{h})$  to the semivariogram model near the origin show suitable conditions for accurate spatial estimation and simulation (Stein, 1987).

For the spatial modeling, the target region was set to a size of  $3 \text{ km} \times 4 \text{ km} \times 1 \text{ km}$  and discretized into parallelepipedic blocks of  $30 \text{ m} \times 40 \text{ m} \times 10 \text{ m}$  along east–west, north–south, and vertical directions, respectively. First, a 3D distribution of the  $\text{Cl}^-$  concentration was estimated by OK. Cross-validation for correlation between the OK prediction and sample value is shown by a scatter plot in Fig. 4.4. Because the coefficient of determination ( $R^2$ ) for the correlation was 0.58, the OK estimates are regarded to have adequate accuracy despite the limited sample data. The OK result was integrated with the formation boundary shape between the Koetoi and Wakkanai formations and geometries of the Omagari Fault and subfault (Fig. 4.5A), which highlights the following noteworthy features. The deep part of the region is mainly occupied by saline and brackish water with high  $\text{Cl}^-$  concentration from 8000 to 12,000 mg/l, in particular in the Wakkanai Formation below  $-450 \text{ m a.s.l.}$  Such high concentrations are equivalent to 42%–60% seawater (19,000 mg/l) and had  $\sim 16,000 \text{ mg/l}$  as a maximum. The Omagari Fault and subfault were found to make a clear boundary between those high concentrations and low  $\text{Cl}^-$  concentrations, less than 8000 mg/l. This boundary may be caused by the aforementioned high permeability of the fault

damage zone (Fig. 4.2). There was the greatest consistency of high  $\text{Cl}^-$  concentrations with formation shapes in the western parts of the Koetoi and Wakkanai formations (Fig. 4.5B).

Because resistivity data were much greater in number than water quality data, the 3D resistivity distribution was modeled by SGS and integrated with the geometries of formations and faults (Fig. 4.6). Extensive high resistivity zones of 5–9  $\Omega\cdot\text{m}$  dominate the shallow parts, from the ground surface to –500 m a.s.l. in the northeast and to –200 m a.s.l. in the southwest. Below these depths, there are low resistivity zones attributable to the high  $\text{Cl}^-$  concentrations. A noteworthy feature is that high resistivity zones greater than 3  $\Omega\cdot\text{m}$  were distributed linearly along the Omagari Fault and concentrated in the damage zones between it and the subfault. This proves that those zones are highly permeable and possibly act as a feasible pathway for downward flow of freshwater.

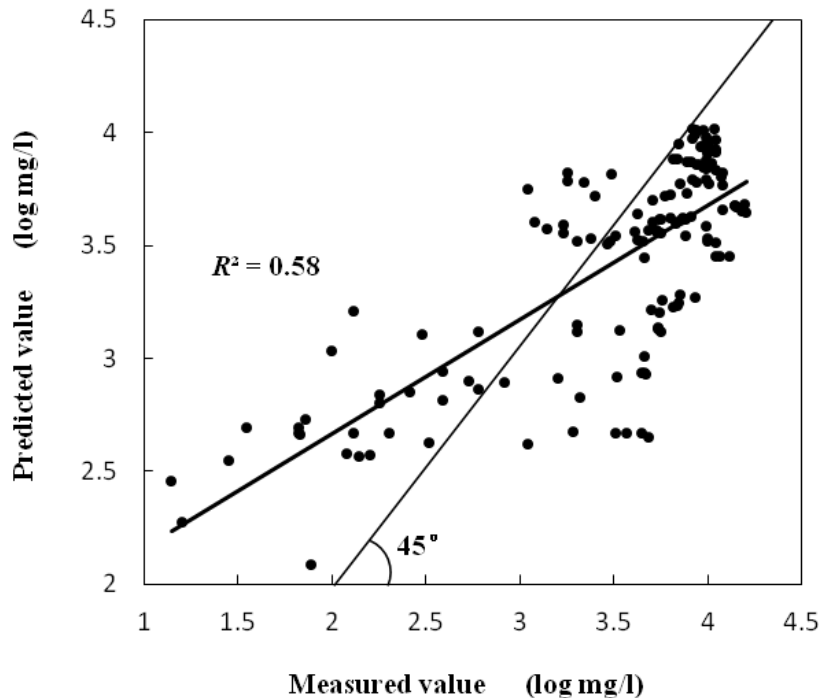


Fig. 4.4 Scattergram between measured and predicted  $\text{Cl}^-$  concentrations for cross-validation of the accuracy of OK result in Fig. 4.5.

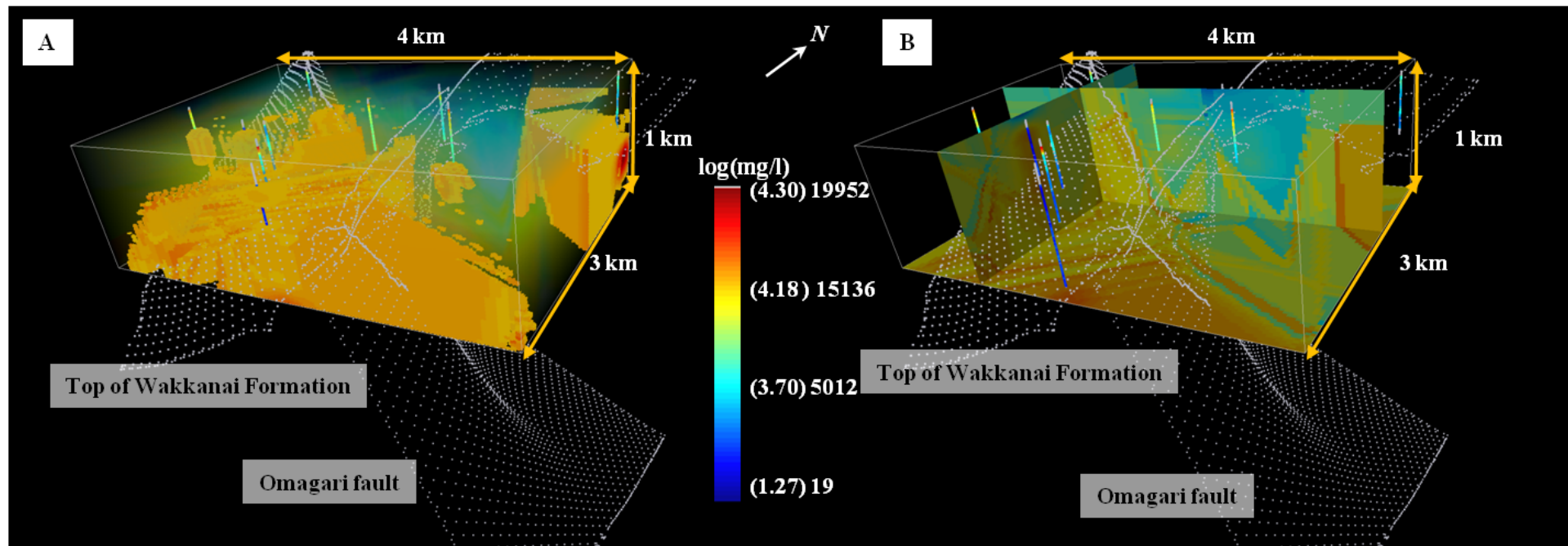


Fig. 4.5 Estimation of  $\text{Cl}^-$  concentration by ordinary kriging (OK) integrated with shapes of Omagari faults and boundaries of Koetoi and Wakkanai formations. A: distribution of relatively high concentrations  $> 8000 \text{ mg/l}$  superimposed on sample data along each borehole; B: panel diagram of  $\text{Cl}^-$  concentration by OK with shapes of Omagari faults and boundaries of Koetoi and Wakkanai formations from geological model shown in Fig. 3.6.

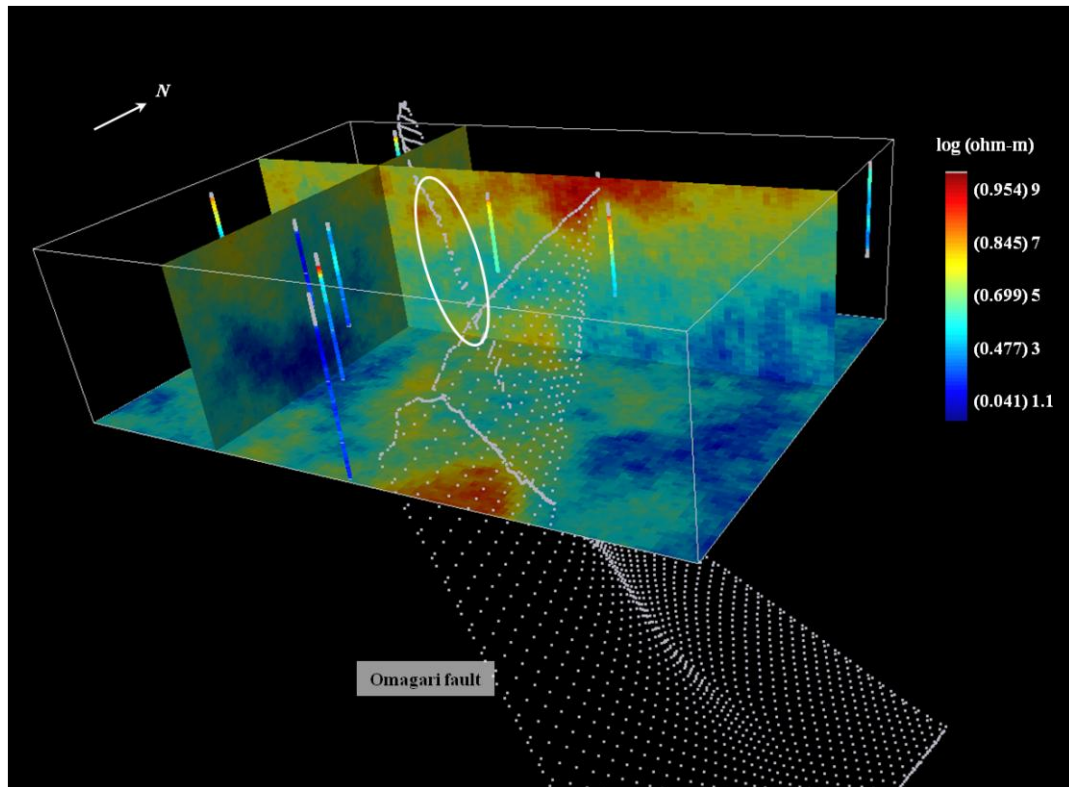


Fig. 4.6 Panel diagram of resistivity distribution by sequential Gaussian simulation (SGS) at same location as Fig. 4.5, superimposed on shapes of Omagari Fault and subfault. Ellipse indicates high resistivity zone in shallow part along Omagari Fault, which suggests downward flow of meteoric waters.

Because the sampling interval of resistivity is much denser than the groundwater chemical sample, and there are total only 145 hydrochemical data. Moreover, resistivity is useful to depict groundwater type and groundwater flow patterns. Therefore, resistivity is very suitable to be used as a secondary variable for hydrochemical modeling. The relationship between resistivity and chloride ion is shown in Fig. 4.7; it is easy to find that there is a negative correlation between them.

As readily estimated, there was strong negative correlation between the  $\text{Cl}^-$  concentration and resistivity data, as shown by a linear correlation coefficient  $R = -0.94$  (Fig. 4.8A). Therefore, SGCS was used to improve the  $\text{Cl}^-$  concentration model by OK.

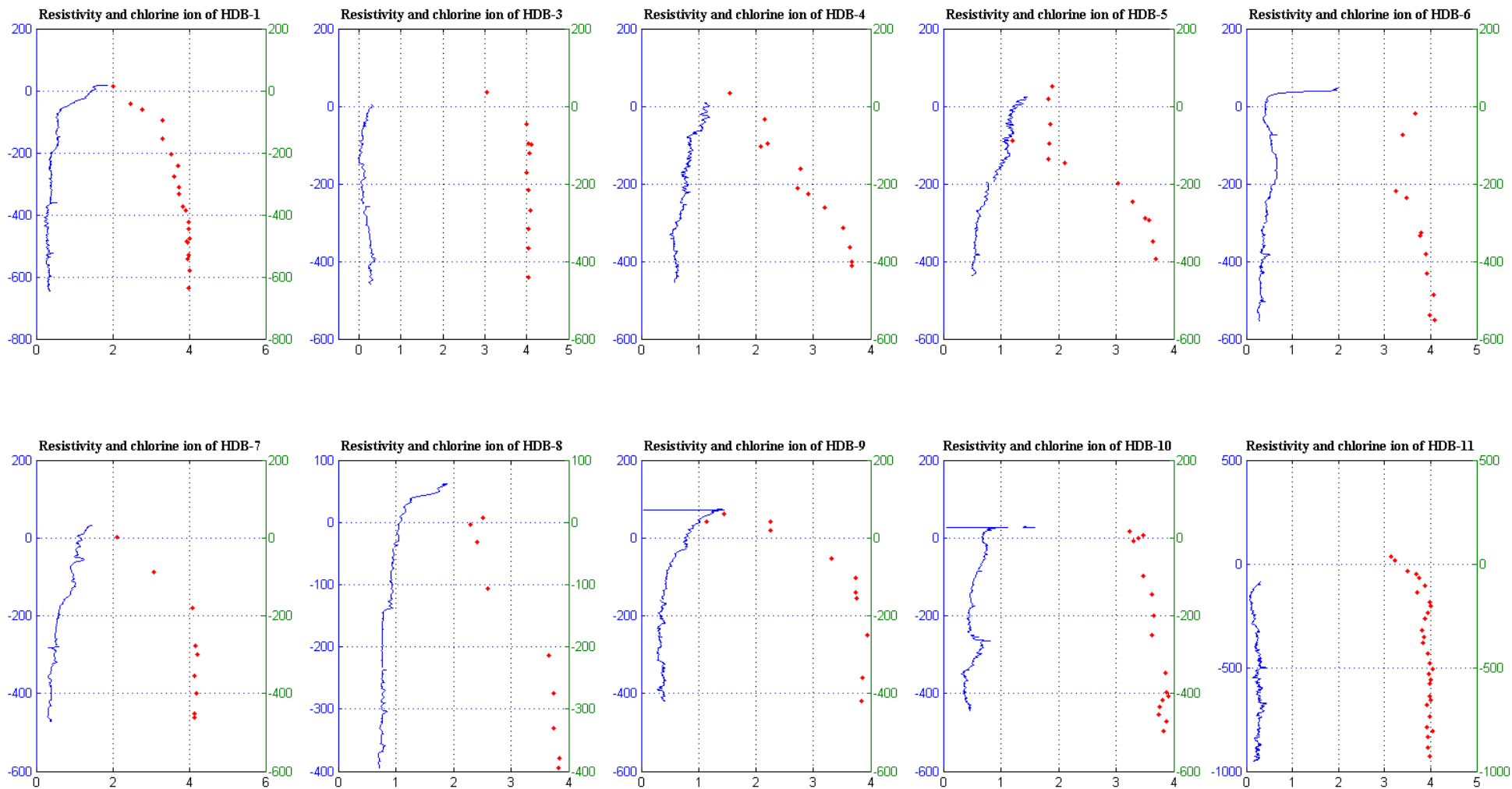


Fig. 4.7 plot of resistivity and concentration of chloride ions

As for the  $\gamma(\mathbf{h})$  of  $\text{Cl}^-$  concentration, omnidirectional experimental

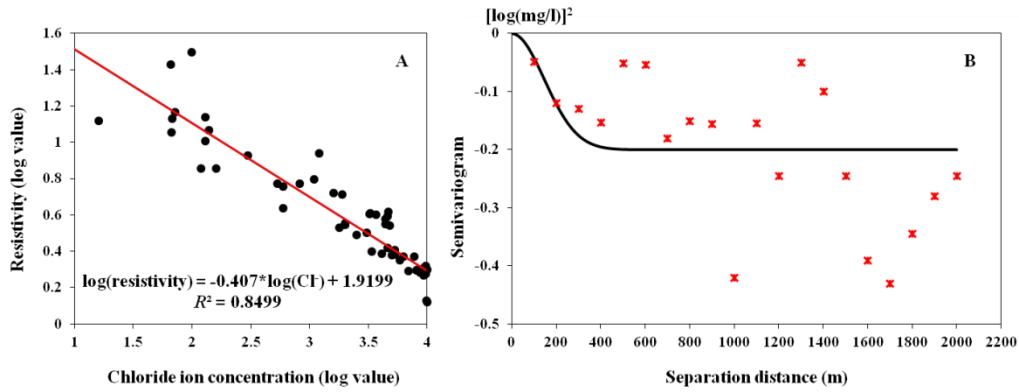


Fig. 4.8 Correlation plot and cross-variogram of resistivity and  $\text{Cl}^-$

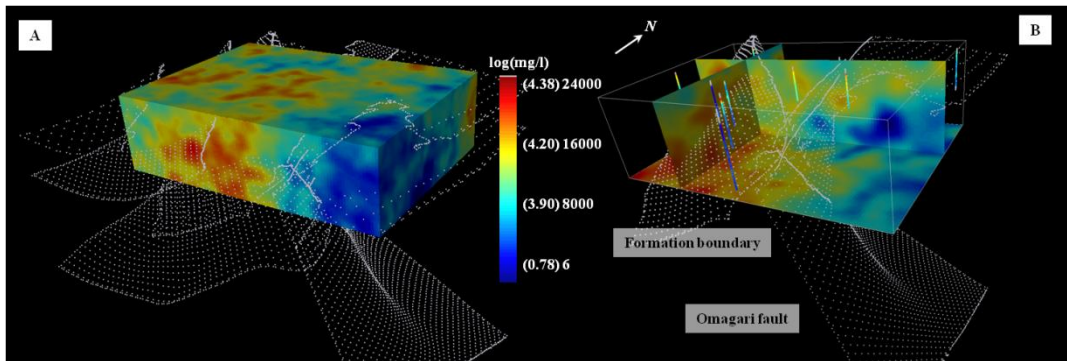


Fig. 4.9 Ten CSGS of  $\text{Cl}^-$  concentration with resistivity (A) and panel diagram of it (B)

cross-semivariogram  $\gamma_c(\mathbf{h})$  between that concentration and resistivity along the  $70^\circ$  dip parallel to the faults fit the Gaussian model well, with range 360 m and nugget effect 0 (Fig. 4.8B). The sill had a negative value because of the negative correlation between the two variables. The average of 10 SGCS realizations was taken as the final result (Fig. 4.9). Effects of bias of sample data locations and data sparseness appeared in the OK result, in that similar values were elongated along the perpendicular bisector between two neighboring borehole sites and presented unnatural linear patterns. Therefore, the OK result represents only the most remarkable features of the  $\text{Cl}^-$  concentrations in groundwater. The effects can be reduced by SGCS, as demonstrated by more variable spatial changes in

concentration in the SGCS result. Nevertheless, the general trend of that result is nearly the same as that of OK, in that the distributions of high concentration zones are mostly coincident in each model, and the Omagari Fault and subfault delineate the main boundary between the high and low concentrations along the Omagari strike (north–northwest to south–southeast).

### **4.3 Summary**

The 3D estimation and simulation of chloride ion were presented in this chapter. One of the most important results is that the geological structure of main Omagari fault showed a strong effect in depicting the spatial structure of chloride ion by variogram; some comparisons illustrated that good fitness of Gaussian model after the dip of Omagari fault was considered into variogram as a parameter. This was not only meaning the importance of geological structure in such modeling, but also showed a way to build statistical-geophysical-geochemical modeling paradigm.

By combination of resistivity logging data, the co-sequential Gaussian simulation successfully improved the smooth effect from kriging estimation and simulated the uncertainty in the spatial modeling. Moreover, the co-sequential Gaussian simulation also was consistent with the kriging estimation on the chloride ion distribution mapping.

## Chapter 5

### Origin of Groundwater and Temporal Change in Salinity

#### 5.1 Origin of groundwater

The oxygen and hydrogen isotopes of H<sub>2</sub>O have become the most useful tools in the study of the origin and evolution of subsurface waters (Sheppard, 1986; Kharaka and Thordsen, 1992). Prior to the use of isotopes, it was generally assumed that most of the formation waters in marine sedimentary rocks were connate marine in origin (White *et al.*, 1963). Clayton *et al.* (1966) were the first to use the isotopic composition of H<sub>2</sub>O to show that waters in several sedimentary basins are predominantly of local meteoric origin. The connate water was lost by compaction and flushing. The extensive use of isotopes of water, solutes, and associated minerals coupled with studies of the regional geology and paleohydrology have shown that subsurface waters generally have a complicated history and that they are commonly mixtures of waters of different origins (Graf *et al.*, 1966; Connolly *et al.*, 1990; Kharaka and Thordsen, 1992; Birkle *et al.*, 2002).

The distribution and controls on the isotopic composition of present-day precipitation and surface waters, especially in mountainous terrains, are complex (e.g., Kharaka *et al.*, 2002). This isotopic composition together with data for

paleoclimates and regional paleogeography can be used to deduce the isotopic composition of old surface waters, including ocean water. An understanding of these parameters is needed to interpret the origin of deep basin brines (Kharaka and Thordsen, 1992). Reactions between water and minerals, dissolved species, associated gases, and other liquids with which they come into contact can modify the isotopic composition of water, especially the value of  $\delta^{18}\text{O}$ . In addition to mixing of waters of different isotopic composition, the following are the main processes that modify the isotopic composition of formation waters in sedimentary basins: (1) isotopic exchange between water and minerals; (2) evaporation and condensation; (3) fractionation caused by the membrane properties of rocks; and (4) isotopic exchange between water and other fluids, especially petroleum.

Because of the practicality of these stable isotopes, they were used to interpret the origin and chemical evolution of the groundwater, in particular the saline water in the deep part. Vertical variations in  $\delta\text{D}$  and  $\delta^{18}\text{O}$  values along each borehole demonstrate that the two isotopes had identical behavior, because they became heavier with depth (Fig. 5.1). Both were light in the shallow part above -400 m a.s.l., whereas the deep part below this depth is enriched by heavy isotopes. Moreover, both of them were near the surface groundwater which was plotted by modern meteoric rain water.

$\delta\text{D}$  and  $\delta^{18}\text{O}$  diagram shown in Fig. 5.2 indicated that there were generally two sources of groundwater. One of them is around surface water, while the other is cluster approaching to stander mean ocean water (SMOW). The first one can be identified as derived from fresh water (modern meteoric rain water); the second one can be identified as related to sea water. But there were some groundwater

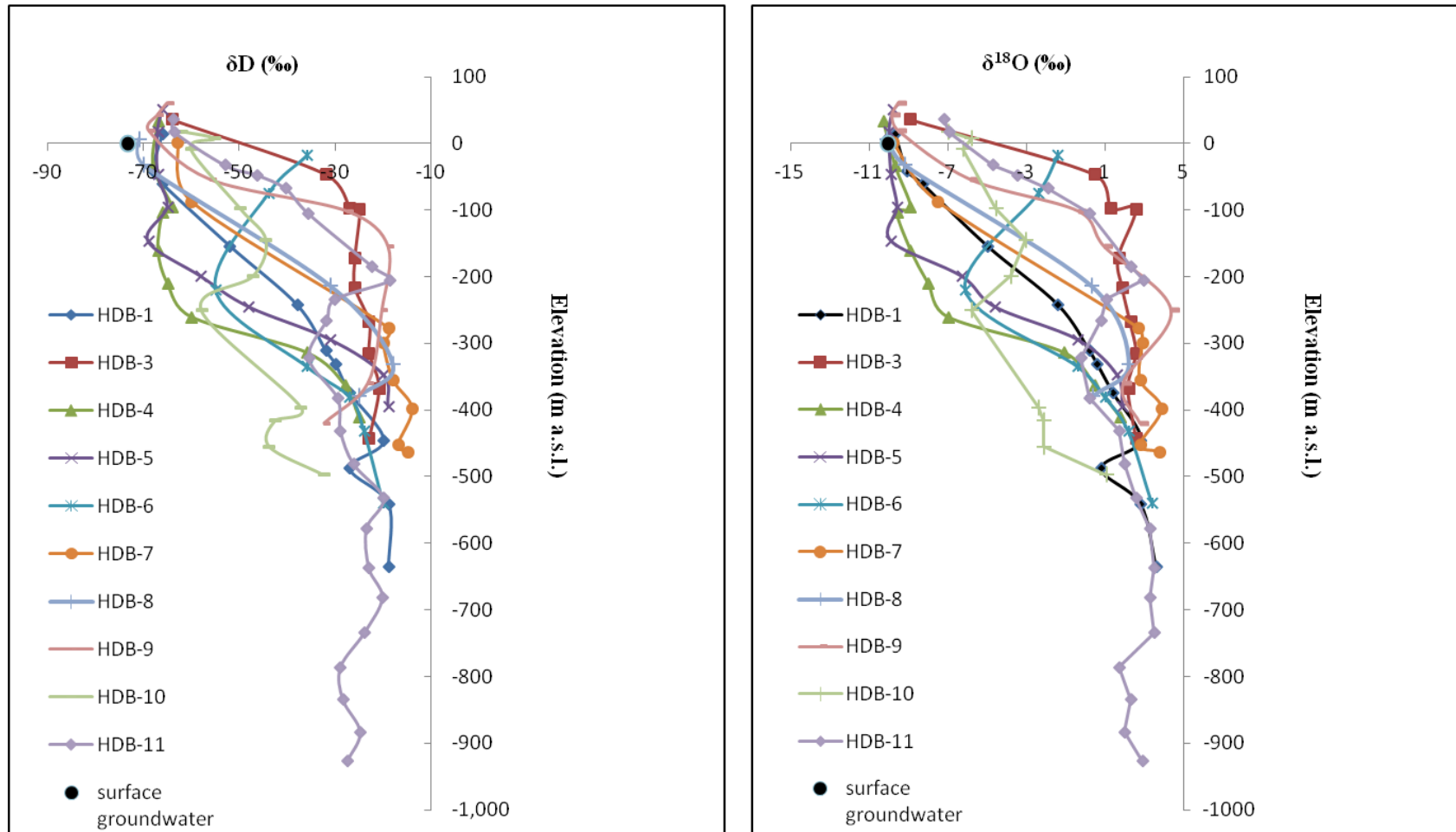


Fig. 5.1 Changes of  $\delta D$  and  $\delta^{18}O$  in pore-water samples with depth for each borehole.

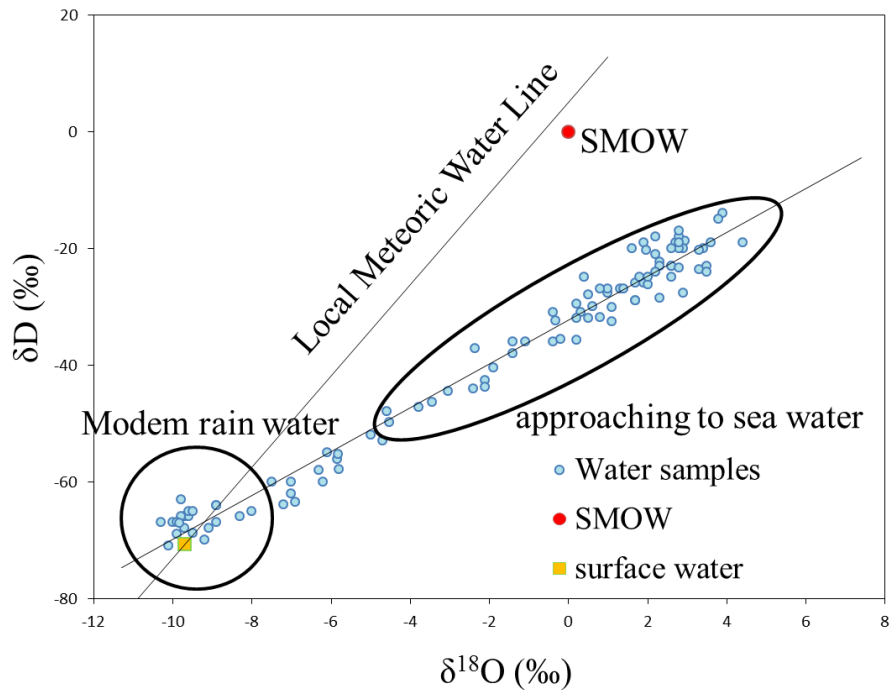


Fig. 5.2  $\delta D$  and  $\delta^{18}O$  diagram shows a general two type of saline water

distributed between these two type, and the second type was far apart from SMOW. There is a need for more detailed analysis about the source of groundwater.

In addition to the stable isotopes, there is a transition zone in the upper part of Wakkanai Formation below the Koetoi Formation. In this zone, the lithology changes downward from diatomaceous mudstone (Koetoi Formation) to siliceous mudstone (Wakkanai Formation), which is a key factor for origin interpretation. The zone is distinguishable in each borehole by log data of density, porosity and resistivity (Fig. 5.3). Because density increased monotonically with depth, porosity was 50%–60%, and resistivity was nearly constant between 2–3  $\Omega$ -m. These petrophysical properties are typical in the well log data of HDB-1 (Fig. 5.4). Depth of the transition zone varied with location, and its thickness increased approaching the Omagari Fault and subfault. This may be from the fracturing of rocks by the faults. Considering the transition zone, the water samples were separated into three general groups. These are Group I from the Koetoi Formation, Group II from the transition zone of Koetoi to upper Wakkanai formations, and Group III from the deep Wakkanai Formation below the transition zone. This

separation is based on the assumption that water quality has a relationship with these three zones of differing petrophysical properties.

$\delta D$  and  $\delta^{18}O$  data of the three groups are plotted in a  $\delta D$ - $\delta^{18}O$  diagram (Fig. 5.5) with the local meteoric water line (LMWL), using precipitation data at Hokushin meteorological station, 2 km northeast of HURL. LMWL was formulated as  $\delta D = 7.8\delta^{18}O + 4.9$  ( $R^2 = 0.83$ ). A regression line for the  $\delta D$  and  $\delta^{18}O$  data ( $R^2 = 0.98$ ) is below the LMWL and intersects it at  $\delta D = -66.77\text{‰}$  and  $\delta^{18}O = -9.20\text{‰}$ , close to the mean value of the present rainfall,  $\delta D = -773.4\text{‰}$  and  $\delta^{18}O = -10.05\text{‰}$ . Among the three groups, waters of Group I are the lightest and most concentrate around the intersection, and have more negative  $\delta D$  values than stratigraphically deeper samples. Hydraulic conductivities in the shallow part were confirmed to be relatively high, especially in the Wakkanai Formation damage zone, with values  $\geq 10^{-6}$  m/s (Fig. 4.1). The formation of a high resistivity zone was likewise detected along the Omagari Fault (Fig. 4.6). These two features suggest that the relatively dilute and low  $Cl^-$  waters of Group I in the Koetoi Formation near the Omagari Fault, which acts as a permeable pathway, probably originated from Holocene meteoric water.

Most data of Group III show relatively heavy values of  $\delta D$  and  $\delta^{18}O$  in the ranges  $-30\text{‰}$  to  $-15\text{‰}$  and  $0\text{‰}$  to  $+4\text{‰}$ , respectively, and are the closest to standard mean ocean water (SMOW) among the three groups. Based on studies of  $\delta D$  and  $\delta^{18}O$  in many fields, these values of oil field brine are larger than most surface waters (Rankama, 1954; Clark and Fritz, 1997; Kloppmann *et al.*, 2001; Shouakar-Stash *et al.*, 2007), and the brine probably originated from ocean water rather than meteoric waters. Therefore, the origin of the blackish and saline waters in the deep part of HURL is inferred as fossil seawater trapped during diagenetic sedimentation in the Miocene. This fossil water was aged 1 Ma or older by the dating method using  $^4He$  and  $^{36}Cl$  (Nakata and Hasegawa, 2010). The  $\delta D$  and  $\delta^{18}O$  data of Group II are widely scattered. The transition zones are generally in the depth range  $-200$  to  $-400$  m a.s.l., in which hydraulic conductivities varied from  $10^{-10}$  to  $10^{-8}$  m/s (Fig. 4.1). This wide range of rock permeability may cause the heterogeneity of Group II waters, which are probably a mixture of deep saline and shallow fresh waters.

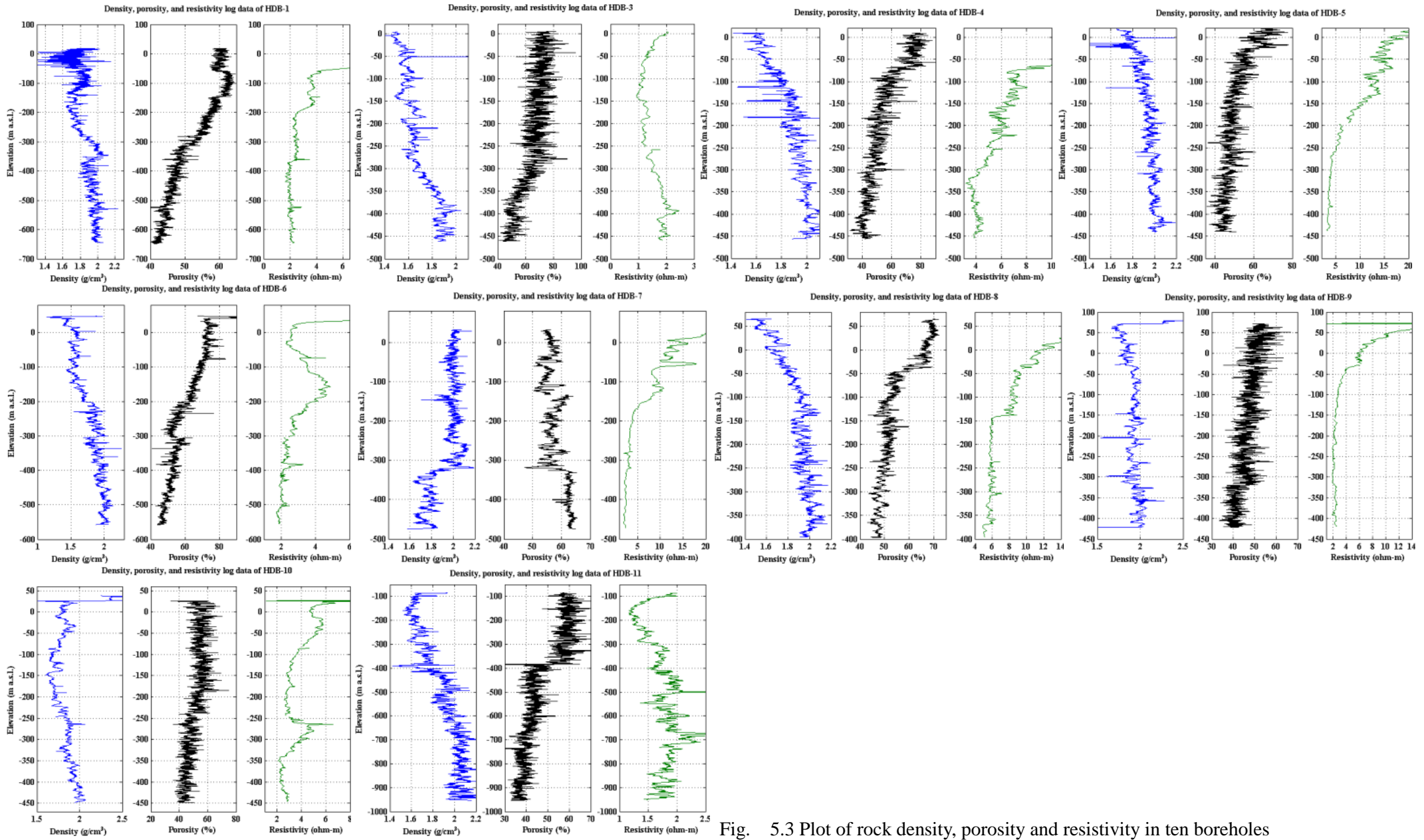


Fig. 5.3 Plot of rock density, porosity and resistivity in ten boreholes

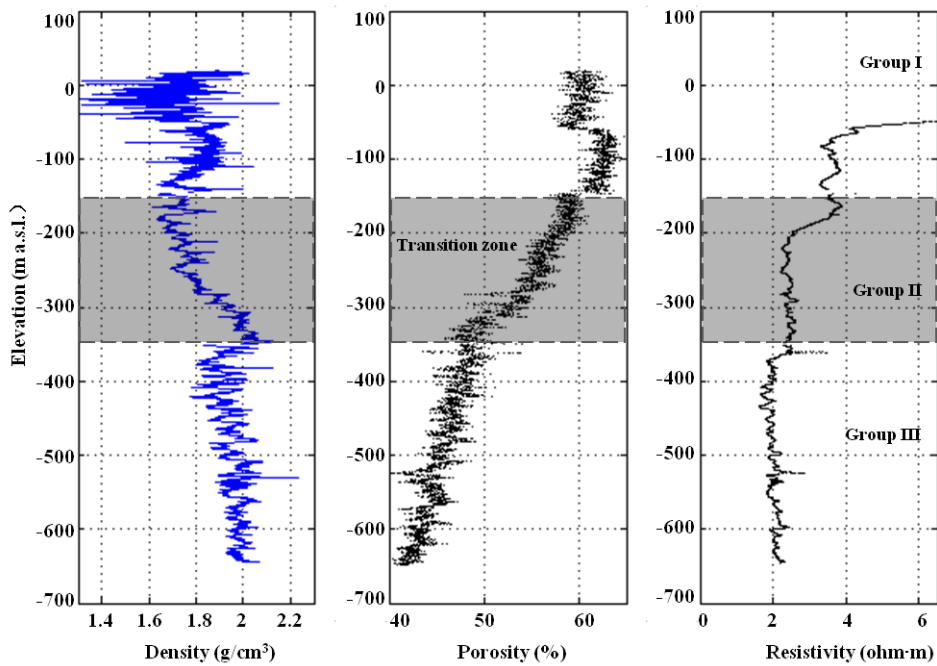


Fig. 5.4 Density, porosity, and resistivity log data of HDB-1 showing three zones of similar rock properties. Water sample data from the three zones are identified as Groups I, II, and III.

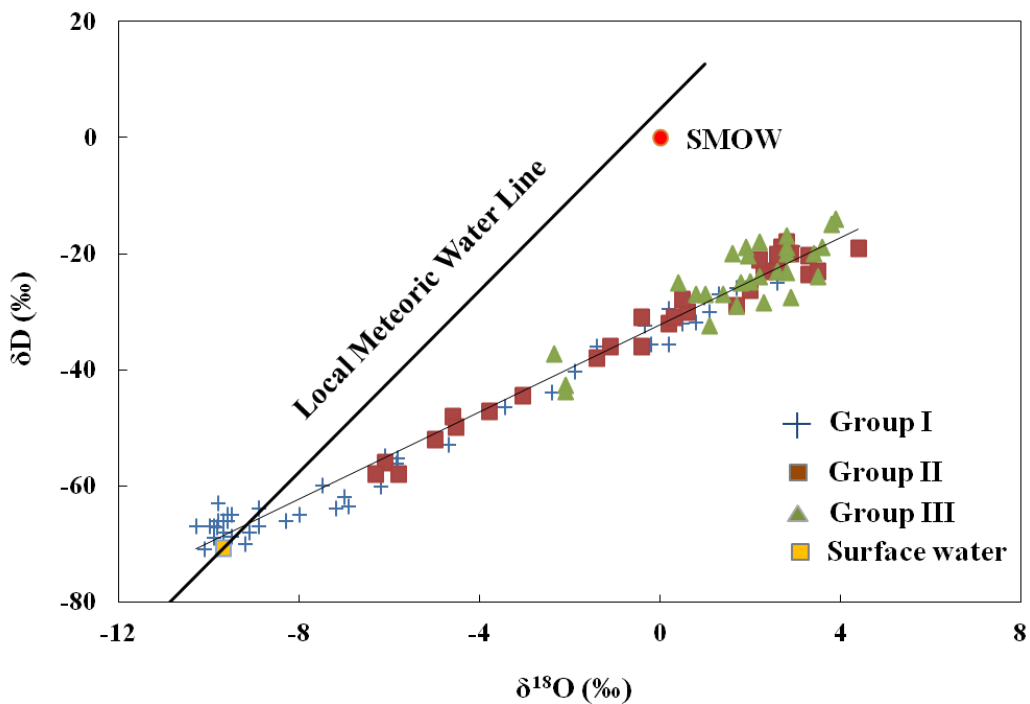


Fig. 5.5 Stable isotope,  $\delta D$  and  $\delta^{18}O$  diagram with Local Meteoric Water Line (LMWL). Data are classified into three groups.

## 5.2 Chemical evolution of saline water

Although the waters of group III were inferred to originate from fossil seawater as mentioned above, their salinities were generally less than 60% of the present seawater. This dilution facilitates building a model of chemical evolution of the HURL groundwater as follows.

The study area was divided into two parts, based on the 3D geological structure model, using a criterion of the distance from the Omagari Fault and subfault. This represents the internal region relatively close to these faults, within 700 m perpendicularly from the fault planes. This includes HDB-1, HDB-4, HDB-5, HDB-6, HDB-8 and HDB-9, and the external region separated from the faults by that distance, including HDB-3, HDB-7, HDB-10, and HDB-11 (Fig. 3.1). We selected 700 m by considering the maximum width of the Omagari Fault effect on hydraulic conductivity as the damage zone (Fig. 4.1), and from the extent of the relatively high  $\text{Cl}^-$  concentration zone estimated by OK (Fig. 4.5A). Because  $\delta\text{D}$  may be conserved during chemical evolution and is less prone to diagenetic alteration as compared with  $\delta^{18}\text{O}$ , scatter plots of  $\delta\text{D}$  with other chemical components can aid the interpretation of the chemical transition mechanism of groundwater (Connolly *et al.*, 1990). Two combinations,  $\delta\text{D}$ - $\delta^{18}\text{O}$  and  $\delta\text{D}$ - $\text{Cl}^-$  concentration, are plotted separately for the internal and external regions (Fig. 5.6). From the two  $\delta\text{D}$ - $\delta^{18}\text{O}$  scattergrams, both  $\delta\text{D}$  and  $\delta^{18}\text{O}$  of Group I waters in the internal region are confirmed to concentrate around the plot of surface water and are lighter than in the external region. This property implies deeper infiltration of freshwater along the Omagari Fault zone in the shallow part of the internal region. The most remarkable feature in the external region is extremely high  $\text{Cl}^-$  concentration data, beyond the regression line, around the heaviest  $\delta\text{D}$  and  $^{18}\text{O}$  values. Such peculiar waters are evident in all three groups.

Control factors that can modify chemical and stable isotopic compositions of groundwater in sedimentary rocks are filtration/fractionation of rock membrane properties, evaporation and condensation of seawater in rocks, and isotopic exchange between water and minerals (Kharaka and Hanor, 2005). Because the principal minerals of the Wakkanai and Koetoi formations are opal-CT and opal-A (Fig. 5.7), respectively, (a) Fault surface in siliceous mudstone showing the surface-parallel alignment of platy particles and silica films. The films have fused

silica textures. (b) Siliceous mudstone matrix adjacent to a fault surface, showing partially comminuted opal-CT lepispheres precipitated within pore spaces. (c) Fault surface in diatomaceous mudstone, showing the surface-parallel alignment of platy particles and silica films. The films have fused silica textures. (d) Diatomaceous mudstone matrix adjacent to the fault surface. The dilution of salinity in pore waters is partially attributable to upward density flow associated with mineral dehydration from opal-A to opal-CT (Iwatsuki *et al.*, 2009).

The scattergrams of  $\text{Cl}^-$  concentration with  $\delta\text{D}$  reveal that fossil seawater in the internal region, whose  $\text{Cl}^-$  concentrations are lower than 10,000 mg/l, have been generally more diluted than in the external region. A possible cause of this concentration feature is the difference in groundwater flow pattern between the internal and external regions, as described schematically in Fig. 5.8. In the internal region, vertical flows may have been prominent because of the Omagari Fault damage, which has acted as a main upward flow path for squeezed waters by compaction in the Wakkanai Formation, for dehydration waters in this formation, and also as downward flow for meteoric waters in the shallow parts. In the external region, lateral flows may have been dominant, which are generally parallel to shapes of the Koetoi and Wakkanai formations. As mentioned above, our flow-pattern model is supported by the fact that the high  $\text{Cl}^-$  concentrations are consistent with formation shapes as shown by the OK model (Fig. 4.5B), and also by a conceptual, regional-scale groundwater flow system in the Horonobe area (Ota *et al.*, 2011).

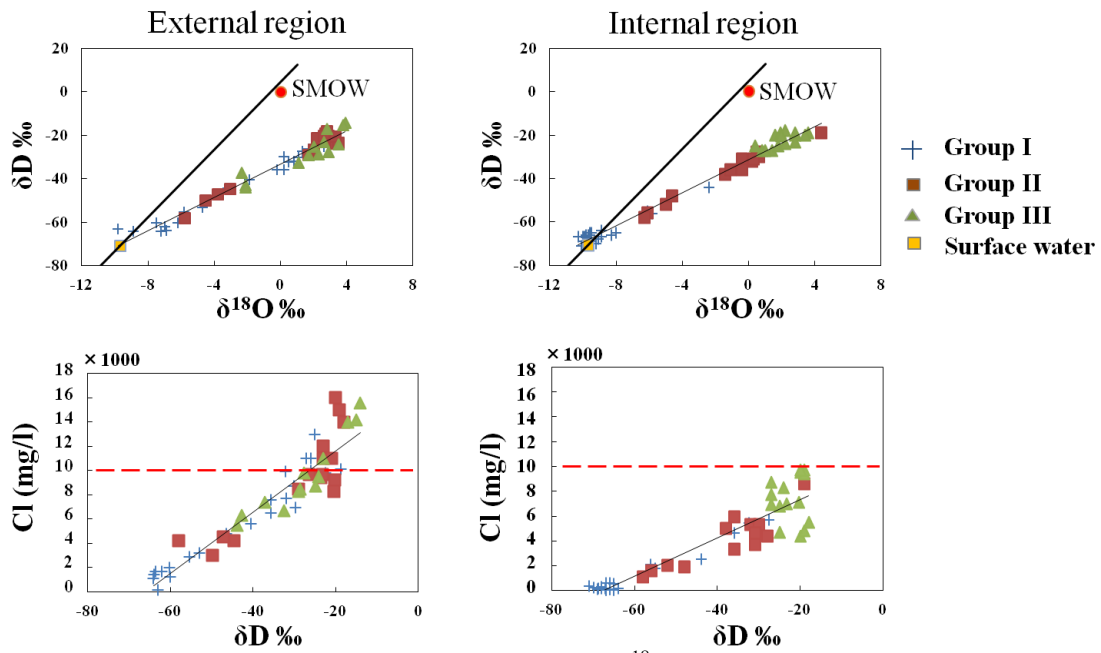


Fig. 5.6 Two scattergrams between  $\delta D$  and  $\delta^{18}O$  and  $Cl^-$  concentration and  $\delta D$  data of three groups in internal and external regions. The regions are defined by a criterion of distance from Omagari Fault and its subfault: internal ( $\leq 700$  m) and external ( $> 700$  m).

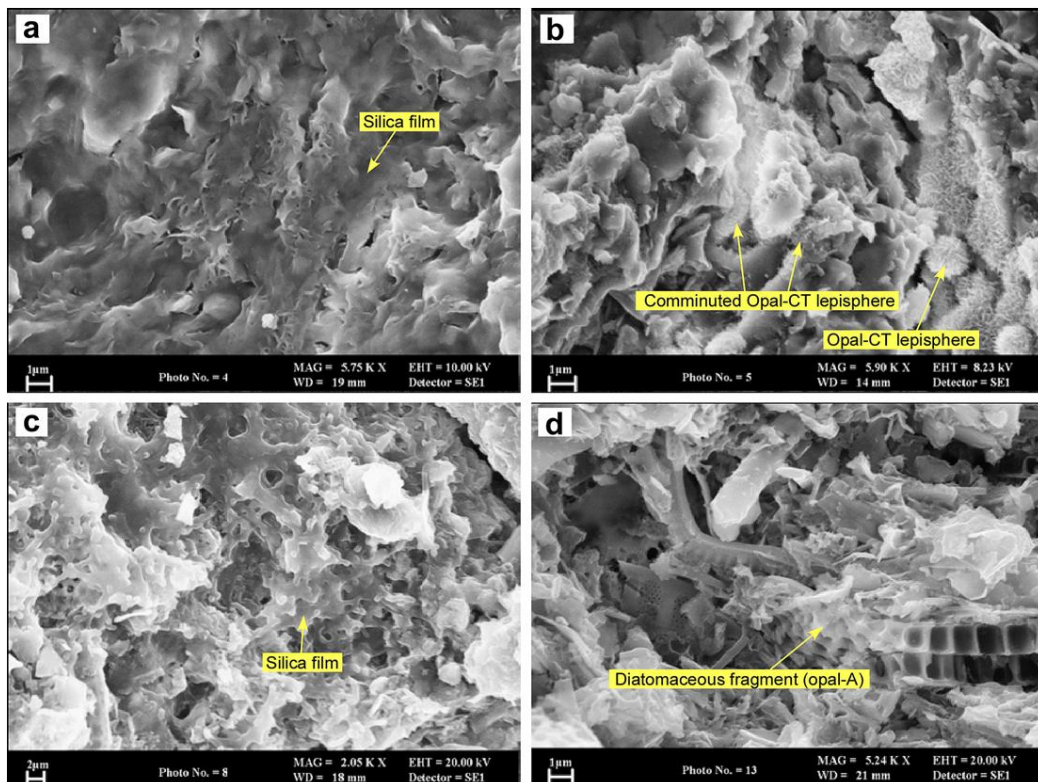


Fig. 5.7 High-resolution SEM images.

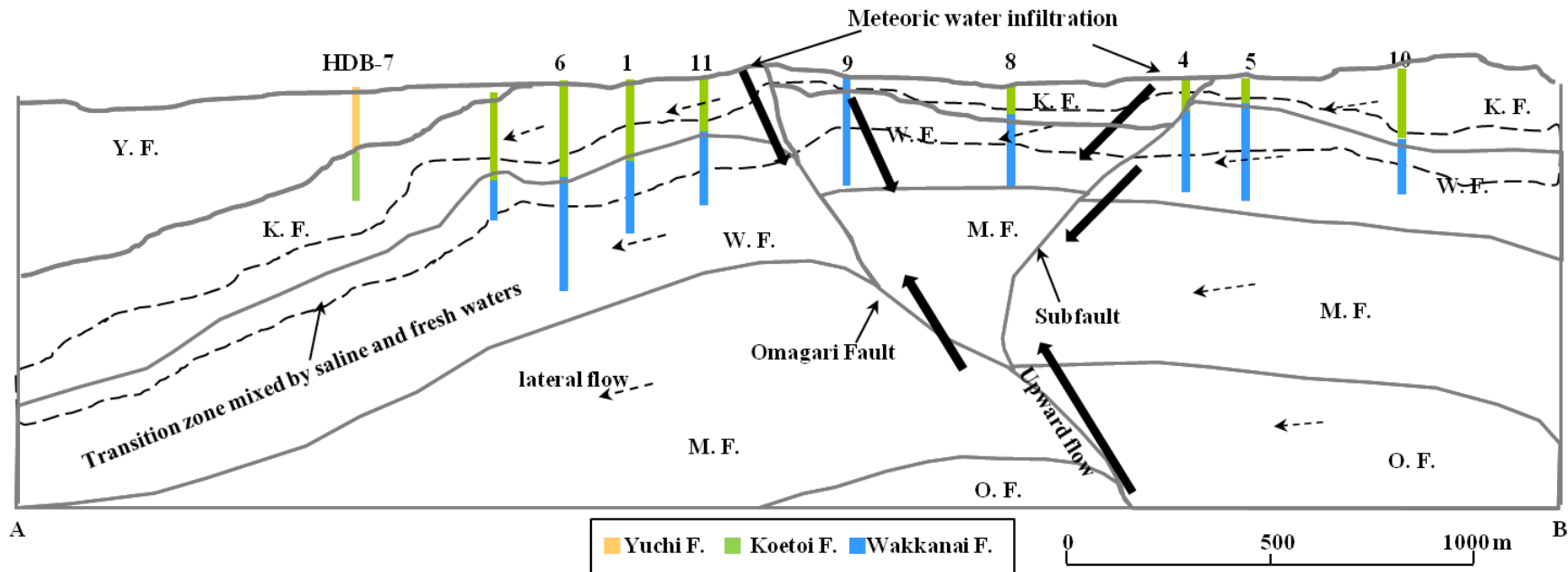


Fig. 5.8 Schematic model of groundwater flow patterns and zonation of fresh, saline, and mixing waters with geological structure along cross-section A-B (Fig. 4.1). Arrows indicate flow directions and magnitudes by their lengths. Y.F.: Yuchi Formation, K.F.: Koetoi Formation, W.F.: Wakkanai Formation, M.F.: Masuporo Formation, and O.F.: Onishibetsu Formation

### 5.3 Groundwater flow modeling in Horonobe area

From chapter 4, the spatial distribution of chloride ion is presented by ordinary kriging and co-sequential Gaussian simulation. It is clear that the Omagari fault and its minor fault played an important role in the spatial structure of saline groundwater. Moreover, the Schematic model of groundwater flow patterns in the fault region, especially the upward flow along Omagari fault can be further and better demonstrated by a groundwater flow modeling in a large scale.

The general groundwater flow differential equation following the Darcy law in 3D can be written as follow,

$$\frac{\partial}{\partial x} \left[ \mathbf{K}_{xx} \frac{\partial h}{\partial x} \right] + \frac{\partial}{\partial y} \left[ \mathbf{K}_{yy} \frac{\partial h}{\partial y} \right] + \frac{\partial}{\partial z} \left[ \mathbf{K}_{zz} \frac{\partial h}{\partial z} \right] + \mathbf{W} = S_s \frac{\partial h}{\partial t}$$

where  $K$  is hydraulic conductivity tensor components,  $h$  is water head,  $S_s$  is specific storage of a confined aquifer,  $t$  is time, and  $W$  is in/ out constant.

Solute flow in groundwater is usually modeled by advection, dispersion and diffusion equation. The target variable in the groundwater flow modeling is chloride ion concentration.

The solute flow in groundwater generally is balance of solute in micro-cube in time unit which means solute accumulation and concentration change in unit time and volume. Average flow velocity is described by Darcy velocity and effective porosity:

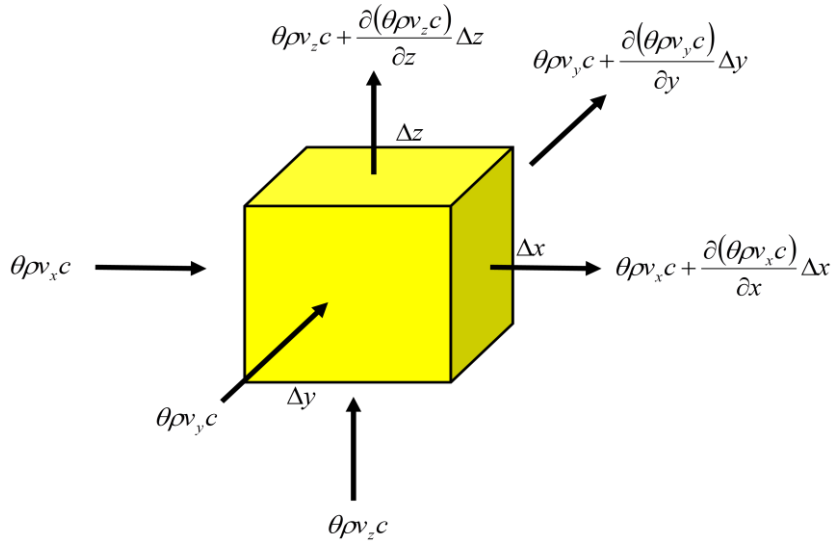
$$V_i = \frac{u_i}{n_e} \quad (i = 1,2,3) \quad (5.1)$$

If there is a concentration change  $\Delta C_{adv}$  in  $\Delta t$  time, the accumulated solute is presented by the change in  $(\rho\theta\Delta C_{adv}) \Delta x\Delta y\Delta z$ .

$$-(\rho\theta\Delta C_{adv})\Delta x\Delta y\Delta z = \Delta t \left\{ \frac{\partial(\rho\theta V_x c)}{\partial x} + \frac{\partial(\rho\theta V_y c)}{\partial y} + \frac{\partial(\rho\theta V_z c)}{\partial z} \right\} \Delta x\Delta y\Delta z \quad (5.2)$$

Here,  $\theta$ : water volume rate,  $\rho$ : solute density,  $c$ : concentration,  $V_i$ : average flow velocity.

This flow velocity is the solute in following micro cube.



When  $\Delta t \Delta x \Delta y \Delta z$  is removed in equation (5.1), and  $\Delta t \rightarrow 0$ ,  $\Delta x, \Delta y, \Delta z \rightarrow 0$ , there is:

$$-\frac{\rho\theta\Delta C_{adv}}{\partial t} = \frac{\partial}{\partial x_i}(\rho\theta v_i c) \quad (i = 1, 2, 3) \quad (5.3)$$

Concentration change in diffusion direction is presented by the solute flux passing  $J_{diff}$  through an area in unit time.

$$J_{diff} = -D_{diff} \frac{dc}{dx_i} \quad (i = 1, 2, 3) \quad (5.4)$$

Here  $D_{diff}$  is diffusion coefficient.

Diffusion of solute is about the Brownian motion in groundwater. Similar to this mechanism, dispersion coefficient  $D$  is also considered into groundwater flow. The accumulated solute in  $\Delta t$  time is presented by concentration change  $\Delta C_{dis}$  in cube, volume of solute is described by  $(\rho\theta\Delta C_{dis}) \Delta x \Delta y \Delta z$ .

$$(\rho\theta\Delta C_{dis})\Delta x\Delta y\Delta z = \Delta t \left\{ \frac{\partial}{\partial x} \left( \theta\rho D_x \frac{\partial c}{\partial x} \right) + \frac{\partial}{\partial y} \left( \theta\rho D_y \frac{\partial c}{\partial y} \right) + \frac{\partial}{\partial z} \left( \theta\rho D_z \frac{\partial c}{\partial z} \right) \right\} \Delta x\Delta y\Delta z \quad (5.5)$$

When  $\Delta t \Delta x \Delta y \Delta z$  is removed in equation (5.5), and  $\Delta t \rightarrow 0$ ,  $\Delta x, \Delta y, \Delta z \rightarrow 0$  there is:

$$\frac{\partial \rho \theta \Delta C_{dis}}{\partial t} = \frac{\partial}{\partial x_i} \left\{ \frac{\partial}{\partial x} \left( \theta \rho D_i \frac{\partial c}{\partial x_i} \right) \right\} \quad (i = 1, 2, 3) \quad (5.6)$$

Combing the diffusion and dispersion equation together, there is solute density flow:

$$\frac{\partial}{\partial t} (\theta \rho c) = \frac{\partial}{\partial x_i} \left( \theta \rho D_{ij} \frac{\partial c}{\partial x_j} \right) - \frac{\partial}{\partial x_i} (\theta \rho V_i c) + Q_c \quad (i = 1, 2, 3) \quad (5.7)$$

Here,  $\theta$ : water volume rate,  $\rho$ : solute density,  $D_{ij}$ : dispersion tension,  $Q_c$ : water source.

The analytic modeling area is the whole Horonobe town, which is 26100 m in W-E direction and 19200 m in S-N direction, and depth is 4010 m (Fig. 5.8).

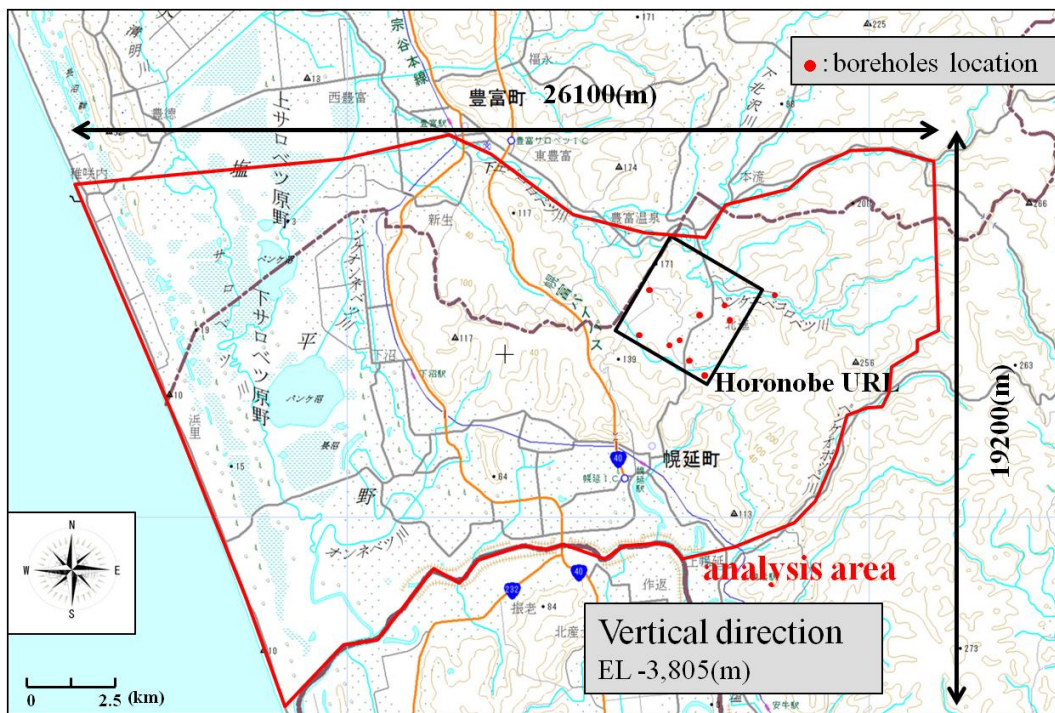


Fig. 5.8 The analytic modeling area

The study area was discreted into grid cells by 300×300 m in horizontal. Because topography largely affected underground water flow simulation, a 50 m mesh DEM (Digital Elevation Model) was used in this modeling (Fig. 5.9). The cells size in z direction is 10 m above 0 m a.s.l., and 50 m below 0 m a.s.l. which is shown in Fig. 5.10.



Table 5.1 Permeability setting

Hydrogeological division	Permeability (m/s)
Surface	$1.0 \times 10^{-6}$
Sarabetsu Formation	$1.0 \times 10^{-6}$
Yuchi Formation	Upper limit: $4.0 \times 10^{-9}$ Lower limit: $2.5 \times 10^{-10}$
Koetoi Formation	Upper limit: $2.5 \times 10^{-7}$ Lower limit: $1.7 \times 10^{-10}$
Wakkanai Formation	Upper limit: $1.4 \times 10^{-5}$ Lower limit: $3.6 \times 10^{-12}$
Masuporo Formation	$5.0 \times 10^{-11}$
Below Masuporo Formation	$5.0 \times 10^{-12}$
Omagari Fault	Upper limit: $1.0 \times 10^{-5}$ Lower limit: $3.6 \times 10^{-11}$
N1 Fault	$1.0 \times 10^{-7}$
Easter side of N1 Fault	$1.0 \times 10^{-10}$

The 3D geological structure of is also integrated into the analytic model. Boundary of model near sea is hydrostatic pressure fixed boundary; bottom and other sides of model are impermeable boundary.

In the groundwater flow modeling we define groundwater flow direction from west to east as E-Flow, east to west as W-Flow, surface to deep part as D-Flow, and deep part to surface as U-Flow (Table 5.2).

Table 5.2 Flow direction and values

	Flow Direction	Maximum ( $\text{m}^3/\text{s}$ )	Median ( $\text{m}^3/\text{s}$ )
E-Flow	West $\rightarrow$ East	$4.75 \times 10^{-3}$	$1.00 \times 10^{-6}$
W-Flow	East $\rightarrow$ West	$2.80 \times 10^{-2}$	$3.81 \times 10^{-6}$
D-Flow	Deep $\rightarrow$ Surface	$1.80 \times 10^{-1}$	$5.64 \times 10^{-5}$
U-Flow	Surface $\rightarrow$ Deep	$1.23 \times 10^{-1}$	$2.57 \times 10^{-5}$

Fig. 5.11 showed the cross-section of analytic model passing through Horonobe URL. Both W-E flow and U-D flow is mixed in shallow part of underground. General trend of groundwater flow is governed by topography, from hills of high elevation to flatland.

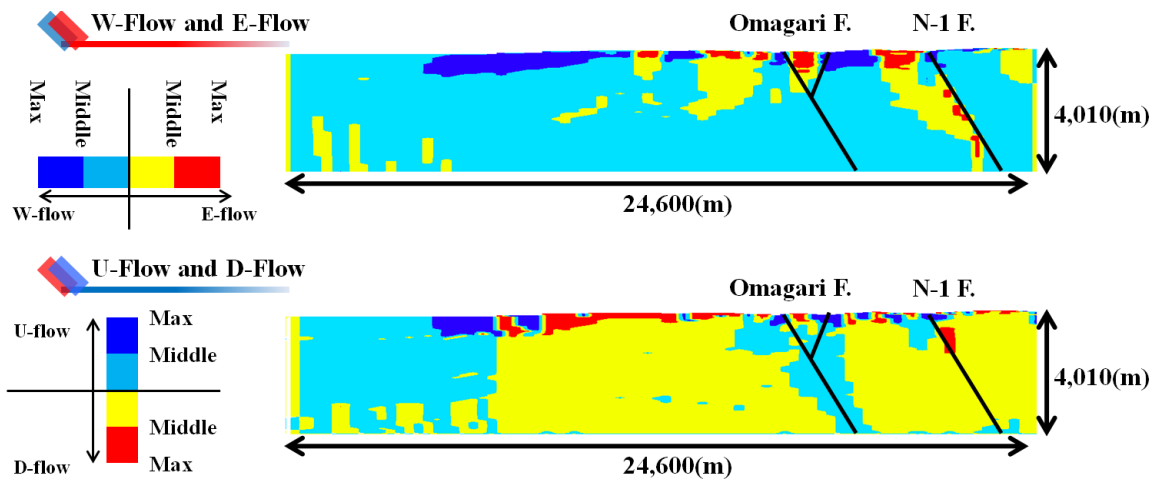


Fig. 5.11 Flow directions in cross-section

In the W-Flow and E-Flow, from EL-800 m in the model, W-Flow is obviously observed. In the U-Flow and D-Flow, from EL-400 m in the west side of plain has a significant U-Flow, and D-Flow is main trend in eastern hills.

Moreover, a unique characteristic of U-Flow is presented along the Omagari fault zone in the model. Therefore, this U-Flow is a strong evidence and proof for the schematic model of groundwater flow patterns in Fig. 5.7 which explained part of the reason for dilution in the deep saline water.

#### 5.4 Summary

Based on the spatial modeling of saline water in three-dimension, the water origin and salinity temporal change was presented in this chapter. Because the Omagari fault showed strong effect in the spatial modeling, the origin and salinity temporal change were also considered by integrating the fault zone.

By classifying the geophysical properties like rock density, porosity and resistivity, the transition zone was identified. The groundwater, thus, were introduced in three groups for the following analysis. From the diagram of  $\delta D$  and  $\delta^{18}O$ , the origin of saline water in deep part can be inferred to originate from fossil seawater trapped in diagenetic sedimentation during the Miocene. Waters in the

shallow part are mostly freshwater of meteoric water origin. The formation of a mixing zone of saline and fresh waters was found in the upper Wakkanai Formation and below the Koetoi Formation.

Meanwhile, based on the distance from the Omagari fault, internal and external zone can be classified for the regional groundwater flow pattern. From the comparisons of  $\delta D$  and  $\delta^{18}O$  and  $Cl^-$  concentration, it was found that in the region near the Omagari Fault and its subfault, vertical flows through the faults predominate, which are down flows of meteoric waters in the shallow part and the aforementioned up flows in the deep part. In a region distant from the faults, lateral flows along small fractures, topography, and shapes of the Koetoi and Wakkanai formations are general.

Moreover, the dilution of water salinity in the deep part may be partially attributed to the dehydration of opal-A to opal-CT in the Wakkanai Formation and upward density flow from the deep part along a permeable damage zone in the Omagari Fault.

## Chapter 6

### Conclusions and Future Work

#### 6.1 Conclusions

Because radioactive wastes of all types need to be responsibly managed in facilities under institutional control to provide public safety, protection of the environment and security from accidental or deliberate intrusion, suitable environment for such disposal assessment requires certain condition for groundwater and geological environment.

Sedimentary rocks have been chosen to be host rock for high level nuclear waste (HLW) disposal in research field due to favorable characteristics of sedimentary rock for long-term HLW disposal repositories. One of main and important topic in researches based on sedimentary rocks is groundwater modeling, especially saline water. This kind of research would demand following perspective, moreover, those requirements usually are inevitably difficult and become challenges deserved to be resolved.

They includes mapping spatial distribution of saline water (seawater or brine), which can be indexed by chloride ion, in three-dimension; integrating geological structure like formations and fault (zone) into the spatial mapping to depict relationship between deep groundwater and geological structure; developing model paradigm honoring various types of information (qualitative and quantitative), multi-source of data (hard data and soft data); being capable in methods to solve sparse dataset modeling.

This work, as for the sparse data, a co-sequential Gaussian simulation (CSGS)

integrating hard data like borehole sampling data and soft data like resistivity logging data is developed, moreover, the fault dip shows strongly act in the modeling that become a parameter in geostatistical estimation and simulation. This was not only meaning the importance of geological structure in such modeling, but also showed a way to build statistical-geophysical-geochemical modeling paradigm. This model paradigm that can be developed as generic model will lead to enhanced understanding of its performances for the costal sedimentary environment in Japan.

The main contents were presented and discussed in this thesis. This research clarified the regional 3D distribution of  $\text{Cl}^-$  concentration in sedimentary rock by geostatistical methods, and interpreted the origin and chemical evolution of groundwater using this model and stable isotope data for a HURL site of  $4 \text{ km} \times 3 \text{ km} \times 1 \text{ km}$  in northern Japan. Deep borehole data were used with geological columns, water chemical data, and well log data from 10 sites. Main results are summarized as follows.

1. The spatial correlation structure of  $\text{Cl}^-$  concentration was ably detected by considering the dip of main (Omagari) fault in the variography. The semivariogram of  $\text{Cl}^-$  concentration and cross-semivariogram with resistivity data along the dip direction were approximated by the Gaussian model.
2. Although a SGCS simulation method could reduce the smoothing effect of 3D  $\text{Cl}^-$  concentration originating from sparseness and bias of the sample data, general trends from SGCS and an OK estimation method were identical. Important features detected were as follows: the Omagari Fault and its subfault delineate a clear boundary between high and low  $\text{Cl}^-$  concentrations, probably from the permeable damage zones in the faults;  $\text{Cl}^-$  concentrations tended to increase with depth and reached 42–60% of seawater in deep parts below  $-450 \text{ m a.s.l.}$ ; the distribution of high  $\text{Cl}^-$  concentrations is consistent with shapes of the main two strata (Koetoi and Wakkanai formations).
3. From  $\delta\text{D}$  and  $\delta^{18}\text{O}$  of pore-water samples, waters in deep parts with relatively heavy  $\delta\text{D}$  and  $\delta^{18}\text{O}$  and high  $\text{Cl}^-$  concentration were inferred to originate from fossil seawater trapped in diagenetic sedimentation during the Miocene. Waters in the shallow part are mostly freshwater of meteoric water origin. The formation of a mixing zone of saline and fresh waters was found in the upper

Wakkanai Formation and below the Koetoi Formation.

4. The dilution of water salinity in the deep part may be partially attributed to the dehydration of opal-A to opal-CT in the Wakkanai Formation and upward density flow from the deep part along a permeable damage zone in the Omagari Fault. By integrating the distributions of  $\text{Cl}^-$  concentration,  $\delta\text{D}$  and  $\delta^{18}\text{O}$ , a plausible groundwater model was constructed as follows. In the region near the Omagari Fault and its subfault, vertical flows through the faults predominate, which are down flows of meteoric waters in the shallow part and the aforementioned up flows in the deep part. In a region distant from the faults, lateral flows along small fractures, topography, and shapes of the Koetoi and Wakkanai formations are general. Consequently, the geometry and permeability of the main fault were identified as controls of groundwater flow pattern and hydrochemistry in the sedimentary rock.

## **6.2 Future work**

This work generally consists of two main parts; each of the parts has interested points that can be improved.

For the spatial modeling of chloride ion, because of sparse data distribution, especially boreholes in horizontal points – only 10 points, the results of classical two-point geostatistics might be improved by multi-point geostatistics.

For the hydrogeochemical modeling of saline water, although stable isotope analysis integrated with geophysical rock properties indicated a groundwater flow pattern in the regional fault zone structure, a groundwater flow modeling could afford much more solid support from hydrological perspective of view.

## References

- Annunziatellis A, Beaubien S, Bigi S, Ciotoli G, Coltella M, Lombardi S. 2008. Gas migration along fault systems and through the vadose zone in the Latera caldera (central Italy): Implications for CO<sub>2</sub> geological storage. *International Journal of Greenhouse Gas Control* **2**(3): 353–372. doi:10.1016/j.ijggc.2008.02.003
- Beauheim RL, Roberts RM, Avis, JD. 2014. Hydraulic testing of low-permeability Silurian and Ordovician strata, Michigan Basin, southwestern Ontario. *Journal of Hydrology* **509**: 163–178. doi:10.1016/j.jhydrol.2013.11.033
- Bense VF, Person MA. 2006. Faults as conduit-barrier systems to fluid flow in siliciclastic sedimentary aquifers. *Water Resources Research* **42**(5): 1–18. doi:10.1029/2005WR004480
- Bense VF, Van den Berg EH, Van Balen RT. 2003. Deformation mechanisms and hydraulic properties of fault zones in unconsolidated sediments; the Roer Valley Rift System, The Netherlands. *Hydrogeology Journal* **11**(3): 319–332. doi:10.1007/s10040-003-0262-8
- Bense VF, Gleeson T, Loveless SE, Bour O, and Scibek J, 2013. Fault zone hydrogeology, *Earth Science Reviews*, doi:10.1016/j.earscirev. 2013.09.008.
- Caine JS, Evans JP, Forster CB. 1996. Fault zone architecture and permeability structure. *Geology* **24**(11): 1025–1028.
- Castelletto N, Gambolati G, Teatini P. 2013. Geological CO<sub>2</sub> sequestration in multi-compartment reservoirs: Geomechanical challenges. *Journal of Geophysical Research: Solid Earth* **118**(5): 2417–2428. doi:10.1002/jgrb.50180
- Clark I, Fritz P. 1997. *Environmental Isotopes in Hydrogeology*. CRC Press: 256-259.
- Clayton R, Friedman I, Graf DL, Mayeda TK, Meents WF, Shimp NF. 1966. The origin of saline formation waters: 1. Isotopic composition. *Journal of Geophysical Research* **71**(16): 3869–3882.
- Connolly CA, Walter LM, Baadsgaard H, Longstaffe FJ 1990. Origin and evolution of formation waters, Alberta Basin, Western Canada Sedimentary Basin. II. Isotope systematics and water mixing. *Applied Geochemistry* **5**: 397–413.
- Cressie N. 1993. *Statistics for Spatial Data*, rev. ed. John Wiley & Sons. Inc.
- Deutsch CV, Journel AG. 1998. *GSLIB: Geostatistical Software Library and User's Guide* (Applied Geostatistics Series). Oxford University Press; 2 ed.
- Desbarats AJ, Bachu S. 1994. Geostatistical analysis of aquifer heterogeneity from the core scale to the basin scale: A case study. *Water Resources Research* **30**(3): 673–684.
- Douglas M, Clark ID, Raven K, Bottomley D. 2000. Groundwater mixing dynamics at a Canadian Shield mine. *Journal of Hydrology* **235**: 88–103. doi:10.1016/S0022-1694(00)00265-1
- Ferrill DA, Winterle J, Wittmeyer G, Sims D, Colton S, Armstrong A, Morris AP. 1999. Stressed rock strains groundwater at Yucca Mountain, Nevada. *GSA TODAY* **9**(5): 1–8.
- Flint AL, Flint LE, Kwicklis EM, Bodvarsson GS, Fabryka-martin JM. 2001. Hydrology of Yucca Mountain, Nevada. *Reviews of Geophysics* **39**(4): 447–470.

- Folch A, Mas - Pla J. 2008. Hydrogeological interactions between fault zones and alluvial aquifers in regional flow systems. *Hydrological Processes* **22**: 3476–3487. doi:10.1002/hyp.6956
- Fujioka N, Saga H. 1980. Geological Consideration on the Petroleum Exploration in the Tenpoku Area, Hokkaido, Japan. *Journal of the Japanese Association of Petroleum Technologists* **45**(4): 183–192. (Japanese with English abstract)
- Fukusawa H. 1985. Late Neogene formations in the Tempoku-Haboro region, Hokkaido, Japan – Stratigraphy reinvestigation of the Wakkanai and Koetoi Formation. *The Journal of the Geological Society of Japan* **91**(12): 833–849. doi:dx.doi.org/10.5575/geosoc.91.833
- Gassiat C, Gleeson T, Lefebvre R, McKenzie J. 2013. Hydraulic fracturing in faulted sedimentary basins: Numerical simulation of potential contamination of shallow aquifers over long time scales. *Water Resources Research* **49**(12): 8310–8327. doi:10.1002/2013WR014287
- Geological Survey of Japan, AIST. 2012. Seamless digital geologic map of Japan 1:200,000, July 3, 2012 version. Research Information Database DB084.
- Goovaerts P. 1997. *Geostatistics for Natural Resources Evaluation*. Oxford University Press
- Grobe M, Machel HG. 2002. Saline groundwater in the Münsterland Cretaceous Basin, Germany: Clues to its origin and evolution. *Marine and Petroleum Geology* **19**(3): 307–322.
- Hama K, Kunimaru T, Metcalfe R, Martin AJ. 2007. The hydrogeochemistry of argillaceous rock formations at the Horonobe URL site, Japan. *Physics and Chemistry of the Earth* **32**: 170–180. doi:10.1016/j.pce.2005.12.008
- Higashinaka M. 2004. Gravity Data Reprocessing. JNC-TJ5410-2004-003. (Japanese with English abstract)
- Higashinaka M, Tsukuwi R, Ohta Y. 2002. Exploration of the Underground Structure Using Seismic reflection method in the Horonobe underground research program. JNC-TJ1410-2002-002. (Japanese with English abstract)
- Hirooka E. 1962. Petroleum Geological Study on Tenpoku District in Hokkaido, Japan. *Journal of the Japanese Association of Petroleum Technologists* **27**(6): 323–344. (Japanese with English abstract)
- Ikawa R, Machida I, Koshigai M, Nishizaki S, Marui A. 2014. Coastal aquifer system in late Pleistocene to Holocene deposits at Horonobe in Hokkaido, Japan. *Hydrogeology Journal* **22**(5): 987–1002. doi:10.1007/s10040-014-1106-4
- Ishii E. 2012. Microstructure and origin of faults in siliceous mudstone at the Horonobe Underground Research Laboratory site, Japan. *Journal of Structural Geology* **34**: 20–29. doi:10.1016/j.jsg.2011.11.001
- Ishii E, Yasue K, Tanaka T, Tsukuwi R, Matsuo K, Sugiyama K, Matsuo S. 2006. Three-dimensional distribution and hydrogeological properties of the Omagari Fault in the Horonobe area, northern Hokkaido, Japan. *The Journal of the Geological Society of Japan* **112**(5): 301–314. doi:10.5575/geosoc.112.301 (Japanese with English abstract)
- Iskandar I, Koike K, Sendjaja P. 2012. Identifying groundwater arsenic contamination mechanisms in relation to arsenic concentrations in water and host rocks. *Environmental Earth Sciences* **65**(7): 2015–2026. doi:10.1007/s12665-011-1182-x

- Iwatsuki T, Ishii E, Niizato T. 2009. Scenario Development of Long-term Evolution for Deep Hydrochemical Conditions in Horonobe Area, Hokkaido, Japan. *Journal of Geography* **118**(4): 700–716. (Japanese with English abstract)
- Kharaka YK, Hanor JS. 2005. Deep fluids in the continents: I. Sedimentary basins J.I. Drever (Ed.), *Surface and Ground Water, Weathering and Soils, Treatise on Geochemistry*, vol. 5 Elsevier: 499–540.
- Kiho K, Oyama T, Mahara Y. 1999. Production of the compaction type pore water extraction apparatus and its application to the deep-seated sedimentary rock. *Journal of the Japan Society of Engineering Geology* **40**(5): 260–269. (Japanese with English abstract)
- Kloppmann W, Négrel P, Casanova J, Klinge H, Schelkes K, Guerrot C. 2001. Halite dissolution derived brines in the vicinity of a Permian salt dome (N German Basin). Evidence from boron, strontium, oxygen, and hydrogen isotopes. *Geochimica et Cosmochimica Acta* **65**(22): 4087–4101.
- Koaze T, Nogami M, Ono Y, Hirakawa K (Eds.) 2003. *Regional Geomorphology of the Japanese Islands, vol. 2, Geomorphology of Hokkaido*. Univ. Tokyo Press, Tokyo.
- Kozai N, Ohnuki T, Iwatsuki T. 2013. Characterization of saline groundwater at Horonobe, Hokkaido, Japan by SEC-UV-ICP-MS: Speciation of uranium and iodine. *Water Research* **47**(4): 1570–1584. doi:10.1016/j.watres.2012.12.017
- Krooss BM, Leythaeuser D. 1988. Experimental measurements of the diffusion parameters of light hydrocarbons in water-saturated sedimentary rocks—II. Results and geochemical significance. *Organic Geochemistry* **12**(2): 91–108.
- Lachmar TE. 1994. Application of fracture-flow hydrogeology to acid-mine drainage at the Bunker Hill Mine, Kellogg, Idaho. *Journal of Hydrology* **155**: 125–149.
- Liu CX, Koike K. 2007. Extending Multivariate Space-Time Geostatistics for Environmental Data Analysis. *Mathematical Geology* **39**(3): 289–305. doi:10.1007/s11004-007-9085-9
- Llanos EM, Zarrouk SJ, Hogarth RA. 2015. Numerical model of the Habanero geothermal reservoir, Australia. *Geothermics* **53**: 308–319. doi:10.1016/j.geothermics.2014.07.008
- Matsuo K, Negi T, Yokoi K, Takahashi T, Teshima M. 2004. The Survey of the Omagari Fault Using Audio Frequency Magnetotelluric Method in Horonobe Research Project for the Subsurface Environment. JNC-TJ5410-2004-002. (Japanese with English abstract)
- Mayer A, May W, Lukkarila C, Diehl J. 2007. Estimation of fault-zone conductance by calibration of a regional groundwater flow model: Desert Hot Springs, California. *Hydrogeology Journal* **15**(6): 1093–1106. doi:10.1007/s10040-007-0158-0
- McIntosh JC, Walter LM. 2006. Paleowaters in Silurian-Devonian carbonate aquifers: Geochemical evolution of groundwater in the Great Lakes region since the Late Pleistocene. *Geochimica et Cosmochimica Acta* **70**(10): 2454–2479. doi:10.1016/j.gca.2006.02.002
- Mukherjee A, Fryar AE. 2008. Deeper groundwater chemistry and geochemical modeling of the arsenic affected western Bengal basin, West Bengal, India. *Applied Geochemistry* **23**(4): 863–894. doi:10.1016/j.apgeochem.2007.07.011
- Myers DE. 1982. Matrix formulation of co-kriging. *Mathematical Geology* **14**(3): 249–257.

- Nakata K, Hasegawa T. 2010. Research and development on groundwater dating (Part 10) - Application of groundwater dating by using  $^4\text{He}$  and  $^{36}\text{Cl}$  to groundwater in Horonobe, Hokkaido-, CRIEPI research Report, N09027. (Japanese with English abstract)
- Neuzil CE. 2003. Hydromechanical coupling in geologic processes. *Hydrogeology Journal* **11**(1): 41–83. doi:10.1007/s10040-002-0230-8
- Niizato T, Yasue K. 2005. A study on the long-term stability of the geological environments in and around the Horonobe area – Consideration of site specific features in assessing of the long-term stability of the geological environments. *Journal of Nuclear Fuel Cycle and Environment* **11**: 125-137. (Japanese with English abstract)
- Ogura N, Kamon M. 1992. The subsurface structures and hydrocarbon potentials in the Tenpoku and Haboro area, the northern Hokkaido, Japan. *Journal of the Japanese Association for Petroleum Technology* **57**(1): 32–44. (Japanese with English abstract)
- Oka T. 1986. Distribution and tectonic evolution of Late Cenozoic basins in Hokkaido. *Monograph Association for the Geological Collaboration in Japan* 31: 295-320. (Japanese with English abstract)
- Oka T, Igarashi Y. 1997. Latest Cenozoic formations in the northern part of Teshio Plain, Hokkaido –Sedimentary facies and pollen stratigraphy– in Commemorative Volume on Prof. Kato M. Oka and Kondo (Eds.), 341-365. (Japanese with English abstract)
- Omar H, Arida H, Daifullah A. 2009. Adsorption of  $^{60}\text{Co}$  radionuclides from aqueous solution by raw and modified bentonite. *Applied Clay Science* **44**(1-2): 21–26. doi:10.1016/j.clay.2008.12.013
- Ota K, Abe H, Kunimaru T. 2011. Horonobe Underground Research Laboratory project Synthesis of Phase I Investigation 2001-2005, Volume Geoscientific Research. JAEA-Research-2010-068, Japan Atomic Energy Agency.
- Rankama K. 1954. *Isotope geology*. Pergamon Press, Ltd.: London.
- Remy N, Boucher A, Wu JB. 2011. *Applied Geostatistics with SGeMS: A User's Guide*. Cambridge University Press, reprint ed.
- Rutqvist J, Stephansson O. 2003. The role of hydromechanical coupling in fractured rock engineering. *Hydrogeology Journal* **11**(1): 7–40. doi:10.1007/s10040-002-0241-5
- Sasamoto H, Arthur RC, Hama K. 2011. Interpretation of undisturbed hydrogeochemical conditions in Neogene sediments of the Horonobe area, Hokkaido, Japan. *Applied Geochemistry* **26**(8): 1464–1477. doi:10.1016/j.apgeochem.2011.05.020
- Seebeck H, Nicol A, Stern TA, Bibby HM, Stagpoole V. 2010. Fault controls on the geometry and location of the Okataina Caldera, Taupo Volcanic Zone, New Zealand. *Journal of Volcanology and Geothermal Research* **190**: 136–151. doi:10.1016/j.jvolgeores.2009.04.011
- Shouakar-Stash O, Alexeev SV, Frapce SK, Alexeeva LP, Drimmie RJ. 2007. Geochemistry and stable isotopic signatures, including chlorine and bromine isotopes, of the deep groundwaters of the Siberian Platform, Russia. *Applied Geochemistry* **22**(3): 589–605. doi:10.1016/j.apgeochem.2006.12.005
- Shukla R, Ranjith P, Haque A, Choi X. 2010. A review of studies on CO<sub>2</sub> sequestration and caprock integrity. *Fuel* **89**(10): 2651–2664. doi:10.1016/j.fuel.2010.05.012

- Simmons C, Narayan K, Woods J, Herczeg A. 2002. Groundwater flow and solute transport at the Mourquong saline-water disposal basin, Murray Basin, southeastern Australia. *Hydrogeology Journal* **10**(2): 278–295. doi:10.1007/s10040-002-0192-x
- Stein ML. 1987. Minimum norm quadratic estimation of spatial variograms. *Journal of the American Statistical Association* **82**(399): 765–772.
- Takahashi K, Fukusawa H, Wada N, Hoyanagi K, Oka T. 1984. Neogene stratigraphy and Paleogeography in the Area along the Sea of Japan of northern Hokkaido. *Earth Science (Chikyu Kagaku)* **38**(5): 299–312. (Japanese with English abstract)
- Tarcan G, Gemici Ü. 2003. Water geochemistry of the Seferihisar geothermal area, İzmir, Turkey. *Journal of Volcanology and Geothermal Research* **126**: 225–242. doi:10.1016/S0377-0273(03)00149-5
- Teng Y, Koike K. 2007. Three-dimensional imaging of a geothermal system using temperature and geological models derived from a well-log dataset. *Geothermics* **36**(6): 518–538. doi:10.1016/j.geothermics.2007.07.006
- Tucker ME. 2001. *Sedimentary Petrology: An Introduction to the Origin of Sedimentary Rocks, 3 edition*. Wiley-Blackwell; 212-213.
- White DE, Hem JD, Waring GA. 1963. Chemical Composition of Subsurface Waters. In M. Fleischer (Ed.), *Data of Geochemistry (Sixth Edit.)*. United States Geological Survey.
- Yager RM, Kappel WM, Plummer LN. 2007. Origin of halite brine in the Onondaga Trough near Syracuse, New York State, USA: Modeling geochemistry and variable-density flow. *Hydrogeology Journal* **15**: 1321–1339. doi:10.1007/s10040-007-0186-9
- Yamamoto H. 1979. The geologic structure and the sedimentary basin off northern part of the Hokkaido Island. *Journal of the Japanese Association of Petroleum Technologists* **44**(5): 260–267. (Japanese with English abstract)
- Yamamoto T, Shimo M, Fujiwara Y, Hattori H, Tadokoro T, Iwama H, Nago M, Kumamoto S. 2002. HDB-1 borehole investigation in Horonobe underground research center. JNC-TJ1400-2002-010. (Japanese with English abstract)
- Yasue K, Ishii E. 2005. Clarification of the accurate distribution of the Omagari-Toyotomi fault in the Horonobe Town, northern Hokkaido. *Active Fault Research* **25**: 39–46. (Japanese with English abstract)
- Yu WH, Harvey CM, Harvey CF. 2003. Arsenic in groundwater in Bangladesh: A geostatistical and epidemiological framework for evaluating health effects and potential remedies. *Water Resources Research* **39**(6): WES1-17. doi:10.1029/2002WR001327